SINGLE-CELL ELECTROPORATION USING ELECTROLYTE-FILLED CAPILLARIES -EXPERIMENTAL AND MODELING INVESTIGATIONS

by

Manyan Wang

BS, Nankai University, China 2000

MS, Nankai University, China 2003

MS, University of Pittsburgh, 2008

Submitted to the Graduate Faculty of

The Kenneth P. Dietrich School of

Arts and Sciences in partial fulfillment

of the requirements for the degree of

Doctor of Philosophy

University of Pittsburgh

2012

UNIVERSITY OF PITTSBURGH

DIETRICH SCHOOL OF ARTS AND SCIENCES

This dissertation was presented

by

Manyan Wang

It was defended on

June 21st, 2012

and approved by

Stephen G. Weber, Professor, Department of Chemistry

Shigeru Amemiya, Associate Professor, Department of Chemistry

Michael Trakselis, Assistant Professor, Department of Chemistry

German Barrionuevo, Professor, Department of Neuroscience

Dissertation Advisor: Stephen G. Weber, Professor, Department of Chemistry

Advisor: Stephen G. Weber

Initials:

SINGLE-CELL ELECTROPORATION USING ELECTROLYTE-FILLED CAPILLARIES

-EXPERIMENTAL AND MODELING INVESTIGATIONS

Manyan Wang, PhD

University of Pittsburgh, 2012

Electrolyte-filled capillaries (EFCs) with fine tips provide a highly concentrated electric field for local single-cell electroporation (SCEP) with high spatial resolution. A complete circuit for SCEP experiments was built that consisted of a test circuit and an electroporation circuit, with the ability to monitor electrically the electroporation pulses. SCEP itself was monitored in real time by observing the loss of a fluorescent adduct of glutathione (Thioglo-1-GSH) from the intracellular space. SCEP can be applied for transfection of individual adherent cells. We hypothesize that transfection of single cells can be accomplished with the plasmid contained in a single capillary. During SCEP, electroosmotic flow can pump electrolyte out of the capillary enhancing plasmid transfer into cells. This was confirmed from both simulation and transfection experiments. Cells were successfully transfected with EGFP-C2 plasmid when the loss of Thioglo-1-GSH upon SCEP (ΔF) is larger than 10% and its mass transfer rate (M) through the membrane exceeds 0.03 s^{-1}. A series of SCEP experiments has been carried out on PC-3 cells (with 2-μm tip opening) and A549 cells (with 4~5-μm tip opening) to investigate how the parameters such as cell-to-tip distance (d_c), cell size (d_m) and shape, temperature, current, and the cell cycle affect SCEP outcomes (M and resealing rate α) *via* statistical analysis. A good linear regression is achieved only at a low temperature of 15℃. The main factors affecting small

molecule transport across cell membrane are d_c, d_m and electric current. A range of M (0.03 s^{-1} ~ 0.4 s^{-1} for PC-3 cells, or 0.03 s^{-1} ~ 0.5 s^{-1} for A549 cells) gives the best linear regressions. M is also affected by the cell cycle of A549 cells, and correlated with cell roundness only for PC-3 cells. Cells reseal faster at higher temperature; while lower temperature provides better survivability with identical ΔF. Lastly, numerical models were elaborated as a platform for better understanding of the SCEP process and prediction of the trends of SCEP under various experimental conditions. A mass transport model involving potential distribution, diffusion, convection and electrokinetic flow was extended to study mass transport at a buffer-filled pipette tip/porous medium interface.

TABLE OF CONTENTS

LIST OF TABLES

LIST OF FIGURES

Figure 4.10 Simulated neutral solute concentration distribution under a pulse with an external pressure 117

PREFACE

"Theory guides. Experiment decides." - An old saying in science

I am eternally grateful to my instructor, Prof. Stephen Weber, for his continuous guidance and support. I feel extraordinary lucky to join his research group. He is a very nice, knowledgeable and extremely patient professor. My research work flourished with his valuable suggestions. He has also encouraged me to become a creative, independent, wide-open and hard-working scientist, which is very important for my future career.

I greatly thank our collaborator, Prof Owe Orwar, from Chalmers University of Technology, Sweden. He impressed me with his knowledge in electroporation field. We have also commuted frequently about our research work, which has given me a lot of help.

I highly appreciate the support from all the current and former members in Weber group. They are very kind and cooperative. The whole group is like a family. I am especially grateful to the electroporation team. I obtained many good ideas from them in my research and I am very glad to work with such a good united team.

Finally I devoutly thank my family, including my parents, sisters, my dear husband Hui, and my beloved daughter. Their love gives me utmost strength to conquer the hard times I have ever had in the past years.

1.0 A REVIEW OF SINGLE-CELL ELECTROPORATION

Most of this work has been published in *Analytical and Bioanalytical Chemistry*, 2010, 397, 3235-3238. Reproduced with permission from *Analytical and Bioanalytical Chemistry.*

Single-Cell Electroporation (SCEP) is a relatively new technique that has emerged in the last decade or so for single-cell studies. When a large enough electric field is applied to a single cell, transient nano-pores form in the cell membrane allowing molecules to be transported into and out of the cell. Unlike bulk electroporation where a homogenous electric field is applied to a suspension of cells, in SCEP an electric field is created locally near a single cell. Today, single-cell level studies are at the frontier of biochemical research, and SCEP is a promising tool in such studies. In this review, we discuss pore formation based on theoretical as well as experimental approaches. Current SCEP techniques using microelectrodes, micropipettes, electrolyte-filled capillaries, and microfabricated devices are all thoroughly discussed for adherent, and suspended cells. SCEP has been applied in both in vivo and in vitro studies for delivery of cell-impermeant molecules such as drugs, DNA, and siRNA as well as for morphological observations.

1.1 INTRODUCTION

Electroporation, also called electropermeabilization, is a phenomenon that occurs when a high voltage is applied to cells. As a result of an increase in the transmembrane potential, nanoscale pores are believed to form in the cell membrane, thus allowing molecules to be transported into

and out of the cells. Pore formation can be reversible or irreversible depending on the electrical parameters and cell characteristics. From an experimental perspective, electroporation divides into two groups: bulk or batch electroporation and single-cell electroporation (SCEP). Only in the last ten-to-fifteen years has SCEP gained attention as a potential approach to single cell manipulation and study. Unlike traditional bulk electroporation, in SCEP either a single cell is isolated from its population or an inhomogeneous electric field is focused on the target individual cell, leaving neighboring cells unaffected. An advantage of SCEP is that the electric pulses imposed on one particular individual cell can be optimized to obtain desired electroporation results, which is not the case in bulk electroporation. In bulk electroporation there is inevitably a wide distribution of outcomes among the cells in suspension, while SCEP provides an opportunity to look into the response of a specific single cell with a certain cell size, shape, status and orientation in the electric field. This is especially useful in the cases such as primary cultures and heterogeneous cultures such as brain tissue cultures. SCEP is well-suited for electroporation of adherent cells and cells in tissue. The ability to manipulate cells in their natural environment is very important. At the same time, there are approaches that work for manipulating single cells in suspension. It is capable of improving our understanding of the cytophysiological process inside a single cell, how/why the individuals differ from each other, and how one affects the whole and vice versa. These techniques could also be incredibly useful for applications including administering genes or drugs into single cells in complex tissues such as the brain as well as for acquiring samples from a single cell that will survive the sampling process. Coupling with other ultra-sensitive separation and detection methods, continuous sampling from living cells or delivery of certain molecules into specific cells would provide a window for investigating the actual long-term active behavior inside the individual cells.

SCEP has been reviewed recently. Olofsson, Nolkrantz *et al.* gave a general review on SCEP seven years ago. They narrated the SCEP techniques based on the probe types, microelectrodes, micropipettes and capillaries, and chips and other complex systems [1]. Chao and Ros described SCEP as an import potential approach for non-destructive microfluidic single-cell analysis. They introduced briefly how SCEP is performed on chips [2]. Fox *et al.* reviewed electroporation based on microfluidic devices for cell analysis, transfection, or pasteurization [3]. Uesaka *et al.* focused on a specific method of applying a current through a micropipette for axon tracing in a cultured slice, and concluded that the delivery of fluorescent proteins using this method is an easy way to study the dynamics of the axon [4]. Also, Mishra has thoroughly discussed membrane electroporation biophysics and the mechanism of pore formation [5]. More general reviews explain the fundamentals of electroporation [6-7].

In this review, we have attempted to be comprehensive and provide complete guidance on SCEP topic by including all the important papers on SCEP. We begin with a section on pore formation and closure talking about basic theories in electroporation and the current experimental approaches to demonstrate molecular flux through the electropores. That is followed by sections on experimental techniques and applications. This review primarily focuses on the techniques. We have divided applications into two groups according to the type of target cells: adherent cells and tissue; and suspended cells.

1.2 PORE FORMATION

The standard model for electroporation of many cells in suspension envisions the cell as a sphere in a homogeneous electric field. Because the cell membrane has a low conductivity, the potential

drop across the cell occurs virtually all across the membrane. The increased transmembrane potential results in electroporation, the formation of small, transient pores in the cell membrane.

The actual mechanism behind electroporation has yet to be elucidated, and many theoretical models have been developed. Some models are concerned with macroscopic reasons for the instability of lipid membranes including membrane compression and thinning, which is related to electrostriction, undulation and elastic properties of the membranes. Other models based on the *Smoluchowski* equation [8-10] find the explanation in the transition from hydrophobic pores, with the membrane phospholipids oriented with their long axis oriented as in a normal bilayer, to hydrophilic pores with the polar headgroups lining the inside wall of the pore similar to a reverse micelle. The latter pores are more stable than the former above a critical pore radius. Recently, nanoscale pulse induced electroporation models have stimulated models based on molecular dynamic simulations, which try to explain the pore permeabilization process from the molecular level [11-14]. In spite of the different models for electroporation, there is a commonly accepted concept about pore creation: the pores form on a time scale of nanoseconds and need to overcome a common Arrhenius energy barrier of ≈ 45-50 kT. The energy change associated with aqueous pore formation involves three contributions at zero transmembrane potential: $\Delta E = 2\pi\gamma r - \pi r^2\Gamma + (A/r^4)$. The first term is the energy related to the creation of a stressed pore edge having a length of $2\pi r$ and an edge energy of γ per pore edge length. The second term is associated with the energy to remove a circular flat lipid membrane having an energy per area of Γ. The third term (A is a constant) relates to steric repulsion of the lipids lining the pore. A fourth term arises when the transmembrane potential, V_m, is nonzero, $-0.5C_{LW}V_m^2\pi r^2$. It depends on the transmembrane potential and, C_{LW}, the change of capacitance from membrane to water. It is assumed that the pore fills with water rather than ions, and C_{LW} is calculated from $C_{LW} = C_w -$

C_m, where C_w and C_m represent capacitances per area for water and the membrane, respectively [15-16]. Finally, recent models for electroporation of a single spherical cell in a uniform electric field give theoretical estimation of pore characteristics [8, 17-19]. According to these models, the pore density can be high, on the order of 10^9 pores/cm^2, of which > 97% are small pores having ~ 1 nm radius.

The potential difference $\Delta\psi_m$ across a cell membrane under an external electric field consists of two major contributions, the natural resting potential $\Delta\psi_0$, and the induced membrane potential, $\Delta\psi_E$. In living cell membranes, $\Delta\psi_0$ is metabolically maintained. Typically, $\Delta\psi_0$ is about - 40 to - 60 mV, where the potential of the outside surface is taken as zero [20]. It is widely accepted that when $\Delta\psi_m$ goes above a critical threshold $\Delta\psi_c$ electroporation occurs. The critical value has been experimentally determined from bulk electroporation to be in the range of 200 mV - 1 V. The corresponding critical electric field E_p ranges from 100 V/cm for large cells such as muscle cells to 1-2 kV/cm for bacteria [21-22]. In a uniform electric field, a larger cell needs a smaller E_p to reach the critical value as shown below.

In a uniform electric field E, at a point M on the cell surface, at time t, the induced transmembrane potential $\Delta\psi_E$ has been analytically solved:

$$\Delta\psi_E(t) = \psi_{in} - \psi_{out} = -f\,g(\lambda)RE\cos\theta(M)(1-\exp(-t/\tau)) \qquad (1.1)$$

where τ is the charging time of the cell membrane, f is related to the shape of the spheroidal cell [23], g depends on the conductivities λ of the membrane, the cytoplasm and the extracellular medium, R is the radius of the spherical cell (in the case that the cell is non-spherical, but still axisymmetric, it is replaced by the semiaxis oriented in the field direction [23-24]), E is the field

strength , *θ(M)* is the angle between the normal to the membrane at the position *M* and the direction of the field. The charging time τ is typically less than 1 μs. If the cell shape is spherical and the membrane is a pure dielectric, $f = 1.5$ and $g(\lambda) = 1$ and this equation reduces to the well-known Schwan equation [25]. For prolate spheroids with the long axis perpendicular to the external field, $1.5 < f < 2$. For prolate spheroids with the long axis parallel to the external field, $1 < f < 1.5$. For oblate spheroids with the short axis parallel to the field, $f > 2$ [26]. Gimsa and Wachneralso extended the Schwan equation to present an analytical solution for the transmembrane potential induced by a homogeneous AC field on arbitrarily oriented ellipsoidal cells. Their model describes the dependence of transmembrane potential on cell size and shape, field frequency, the membrane capacitance, the conductivities of cytoplasm, membrane and external medium, the location of membrane site, and the orientation of the cell with respect to the external field [23]. The sum of $\Delta\psi_E$ and $\Delta\psi_0$, giving rise to the total transmembrane potential, will be greater at the pole facing the positive electrode than at the pole facing the negative electrode.

Kinetic studies of reversible electroporation use submicrosecond imaging to monitor the transmembrane potential in *Xenopus* oocytes exposed to a homogeneous electric field [27-28]. These studies led to a five-step mechanism which is widely adopted [25]. These five steps are induction, expansion, stabilization, resealing, and memory. The external electric field induces an increase in the transmembrane potential until it reaches a critical value. This induction step is thought to be shorter than 1 μs. Recently, the study of nanosecond pulses for electroporation indicates that this step may be in the nanosecond regime [29-30]. The induction step is followed by a continuous increase in permeability as long as the field is maintained at an overcritical value [27]. During this stage, the local density of pores increases, and structural reorganization of the membrane occurs. The time scale of expansion depends on the pulse duration, typically in the range of μs ~ ms. The

increase in the permeability of the membrane increases its conductivity, decreasing the transmembrane potential. The electric field decreases to subcritical level, and, while pores exist, the majority of the membrane reorganizes to a more normal state in the process called stabilization. In the absence of the field, a slow resealing then follows spontaneously on a scale of seconds to minutes, until the membrane recovers its intrinsic impermeability. The complete resealing of the membrane preserves the viability of cells in most pulsing conditions. Nevertheless, some changes in the membrane properties (enhanced phospholipid flip-flop) and cellular physiological properties (formation of macropinocytosis-like vesicles which are important for the uptake of macromolecules) remain present on a longer time scale (minutes to hours). This cell alteration may lead to cell death in the long term.

In SCEP, the same biophysics occurs. The difference is that the typical applied field is not homogeneous. Thus, simulations are common because of the complex geometry in the experiment. The biological cell membrane is either treated as a capacitor parallel to a resistor [31-32], or as a very low conductivity medium in an electrical field [32-33]. Numerical modeling gives the solution to the inhomogeneous electric field distribution and the potential drop across the cell membrane (which depends strongly on the position on the membrane). The theoretical membrane voltage is useful because the statically defined membrane voltage needed to reach the electroporation threshold is known for numerous cell lines from batch electroporation experiments using the Schwan equation and the experimental lowest electric fields triggering cell electroporation (*e.g.,* typically 250 mV for mammalian cells)[21-22]. Therefore, the simulation helps to anticipate the cell's behavior under a given set of geometrical and electrical conditions, giving guidance for controlling SCEP. An outstanding example is the simulation of electroporation in highly inhomogeneous electric fields using a pulled electrolyte-filled capillary by Zudans from

our group [33]. The modeling gives transmembrane potential and fraction of electroporated area over the whole cell area (*FEA*) as a function of applied voltage (V_{tot}) and tip-to-cell distance (d) (Figure 1). The results fit with the experimental outcome that the cells are successfully electroporated when the tip-to-cell distance is ~ 6.5 μm or smaller with an applied voltage of 500 V (capillary length 15 cm).

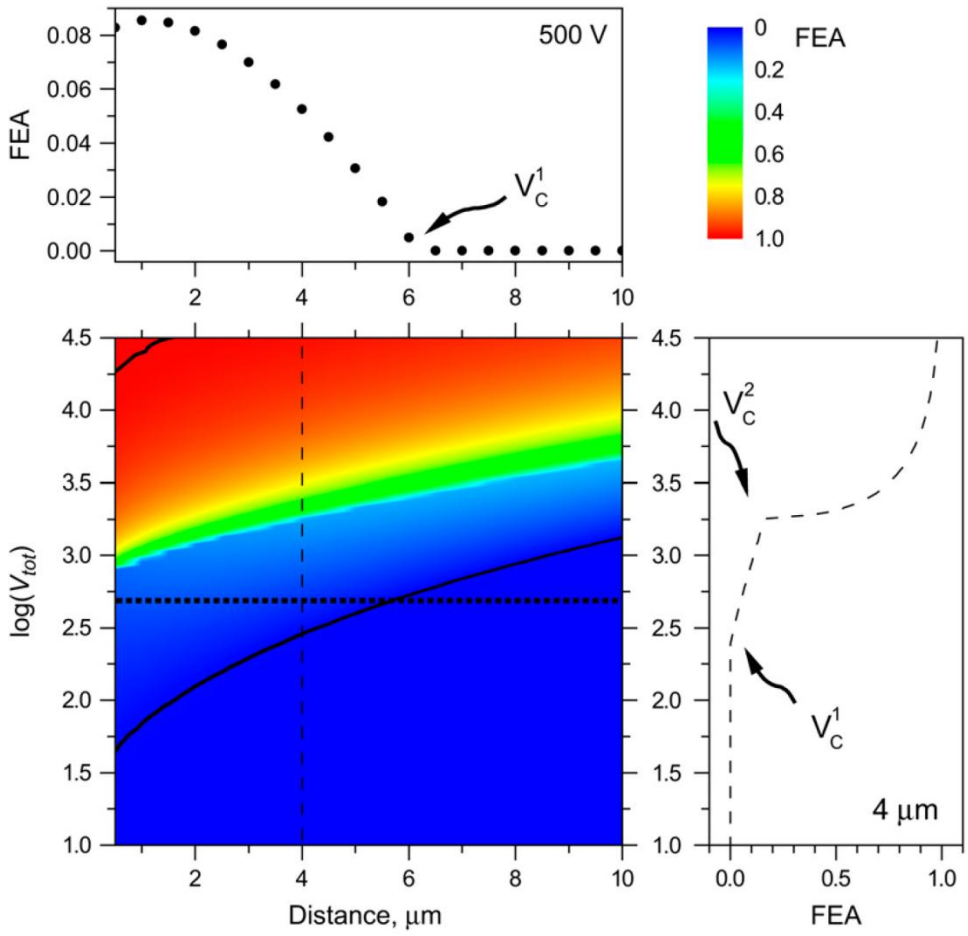

Figure 1.1 Fraction electroporated area of the cell membrane as function of distance and applied potential (in volts)

Note that the applied potential is dropped across a 15 cm capillary. Contours that correspond to 1% and 99% FEA are shown with black solid lines. The upper panel shows a slice of the contour plot at V_{tot} = 500 V (marked with the horizontal dotted line on the contour). The right panel illustrates how FEA varies with log(V_{tot}) at d = 4 μm (marked

with the vertical dashed line in the contour plot). Required experimental total voltages applied that correspond to the beginning of the electroporation (V_{1c}) and the electroporation of the cell side walls (V_{2c}) are marked. The electroporation threshold potential V_{1c} increases with increasing tip-to-cell distance. The increase is the most pronounced at short and becomes more gradual at large distances. Reproduced by permission of Elsevier from Ref. [33]

1.3 MASS TRANSPORT ACROSS THE PERMEABILIZED MEMBRANE

Two techniques are often employed to demonstrate the molecular or ionic flux during SCEP: fluorescence microscopy and patch-clamp recording. Fluorescence microscopy is more general in the way that it demonstrates the exchange of molecules through the transient pores and is commonly used.

In principle, there are two different types of fluorescence microscopy-based assays. One is to introduce cell permeant fluorogenic reagents to cells before electroporation, then observe the loss of fluorescence during electroporation [33]. The other is to use cell impermeant fluorophores or fluorogenic reagents in the extracellular medium and observe the target cells after pulses (*e.g.* labeled dextrans[34-38], propidium iodide[39], fluorescently labeled siRNA [40], and GFP encoded plasmid [2, 41-42]. The direct view of molecules exchanged through the cell membranes also provides physical information of the pores formed, *e.g.* pore size by using libraries of differently sized molecules. We have studied the release of freely diffusing molecules from electroporated cells. Figure 1.2 shows a typical decay curve of the whole-cell fluorescence intensity upon SCEP of an individual cell. The fluorescence comes from a fluorescent adduct of thiols (chiefly glutathione, GSH) resulting from pretreatment with a thiol-reactive fluorogenic dye. The model used [43] assumes a first-order mass transport rate of solute through the pores. This

will be adequate if the diffusional relaxation time within the cell is faster than the mass transport time (~ the inverse of the observed mass transfer rate), as is the case [44]. The model also has a first order rate constant for pore resealing and a first order rate constant for photobleaching. The model fits the time-dependent fluorescence intensity decay well. It yields the mass transfer rate (~ 0.01 s^{-1}) through the electroporated cell membrane and the pore resealing rate when a 500 V pulse (delivered through a 30 cm long pulled capillary) with a duration of 300 ms was applied [44]. Linear regression analysis shows that the mass transfer rate is significantly dependent on the tip-to-cell distance and the cell size. It decreases with an increase of the tip-to-cell distance and cell size. This is consistent with the fact that a smaller tip-to-cell distance and a smaller cell size induce, respectively, stronger electric field near the cell and larger FEA. On the contrary, the resealing rate shows no relationship with the experimental or cell parameters. The uptake of macromolecules such as DNA into electroporated cells is different from small molecules because macromolecules are prohibited from diffusing freely into the cells due to their large size. It is interesting to note, therefore, that their loading into cells is strongly dependent on the small-molecule permeability of electroporated cell membranes. The successful transport of a 4.7 kbp plasmid pEGFP-C2 into a electroporated cell is detected only when the mass transfer rate of small freely diffusive molecules through the cell membrane is greater than 0.03 s^{-1} [45]. Also, loading cells with five different sized fluorescence-labeled dextrans during electroporation has shown a strong correlation between permeability and molecular weight. Large molecules can only penetrate the cell membrane at a high voltage and long pulse duration [46].

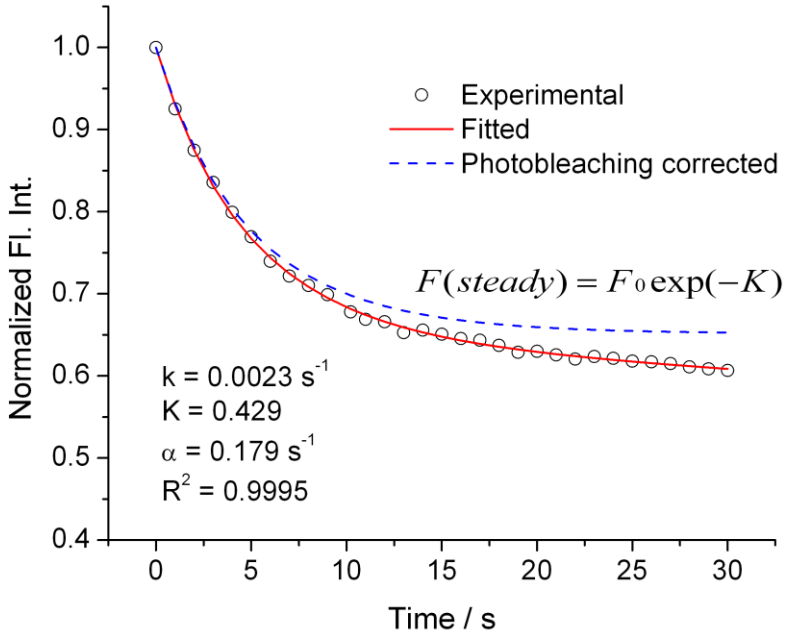

Figure 1.2 An example of a normalized whole-cell fluorescence intensity decay curve upon electroporation and fitting of the curve with an equation to obtain pore information

The equation $I(t) = I_0 e^{(-kt)} e^{K(e^{-\alpha t}-1)}$, $K = M/\alpha$ Parameters *k* (photobleaching), *K* (ratio of mass transport rate constant to pore resealing rate constant) and α (pore resealing) were determined by nonlinear regression. Here *t* is time from the start of the pulse, *I(t)* is the fluorescence intensity at time t, I_0 is the fluorescence intensity at $t = 0$. The circles are experimentally observed fluorescence intensity, the solid curve is the result from the fitting, and the dotted curve represents fluorescence intensity change induced purely by electroporation (*i.e.*, photobleaching removed). Reproduced by permission of American Chemical Society from Ref. [45]

Patch-clamp whole cell recording is a powerful technique to analyze ion flux across cell membranes. This technique incorporated into SCEP experiments [47-49] reveals pore dynamics. It is especially helpful when the lifetime of the pores is in the nanosecond range because such rapid events cannot, generally, be followed with fluorescence microscopy [50]. When pores form in the

cell membrane, the membrane resistance decreases resulting in an increase in the measured current. Because this technique is quantitative, it also serves as a method for determining pore kinetics. Orwar's group applied this technique to SCEP of NG108-15 cells electroporated with a field produced by carbon fiber microelectrodes. The patch-clamp measurements gave an electroporation transmembrane voltage drop threshold of ~250mV, a pore expansion time of 2-50 ms, a pore stabilization time of 8-100 ms and a recovery time of 10-600 ms with a 1-ms pulse.

Recently, the Tao group developed a new plasmonic-based electrochemical impedance microscopy to monitor the cellular dynamics during electroporation. This microscopy method provides high spatial and temporal resolution, and is label-free. This method also makes it possible to resolve subcellular structures and processes during electroporation [51].

1.4 TECHNIQUE DEVELOPMENT

The techniques of SCEP differ from those of bulk electroporation for two main reasons. One is that small voltage/current sources are used to provide a locally focused electric field, and the other is that the targets are individual cells. The target cells can be adherent cells growing on a solid surface, cells suspended in a buffer, tissue cultures, or cells in living tissue. In this review, we discuss SCEP technique development based on the type of target cells.

1.4.1 SCEP of adherent cells and tissues

1.4.1.1 Probes

For adherent cells, usually probes such as solid microelectrodes, micropipettes and electrolyte-filled capillaries (EFC) are used because they can be moved freely to electroporate any cell. To obtain enough spatial resolution for electroporation of one single cell, all of these probes are designed with tip sizes on the micrometer scale (typically smaller than the cell), and they are placed close to or in contact with the target cells. Recently, microfabricated chips have also been reported for adherent cell SCEP with improved throughput. However, since both the electrodes on the chips and the cells are fixed, the electroporated cells are limited to those growing close to the electrodes [52-53] and those where the electric field is focused [54].

The first SCEP experiments from Orwar's lab used solid microelectrodes [55]. Unlike bulk electroporation where large, planar electrodes are used to produce a uniform electric field, in SCEP microelectrodes with tip sizes similar or smaller than the cell are utilized to form an inhomogeneous electric field in the solution. The electric field strength decreases rapidly with increasing distance from the electrode tip. The microelectrodes were placed on both sides of the adherent cells, and a pulse was applied through the microelectrodes, producing a potential drop across the target cells exceeding the required transmembrane potential threshold for electroporation. Usually a low voltage (several volts with millisecond pulse length) is enough for electroporation. Carbon fiber microelectrodes, modified AFM silicon tips, sodium electrodes, and tungsten wire electrodes have been used successfully for SCEP [50, 55-57]. Due to the electrode reactions and the formation of an electric double layer, a significant potential loss at the electrode/solution interface must be taken into account. This is not typically a problem in bulk electroporation because the magnitude of the total applied potential is so much larger than the

interfacial potential drop in that situation (kV vs V). In single-cell electroporation with microelectrodes, the large majority of the total voltage applied drops across the electrode-solution interface. Thus, the potential drop in solution, which an electrochemist would refer to as "IR drop", is small and unknown. The potential drop in solution near a microelectrode, has been experimentally measured at carbon fiber electrodes *via* current interruption for a variety of electrode sizes, shapes and distances from the target cells[32]. These measurements led to the idea that the best way to control the voltage drop across the cells in the solution required for electroporation is to apply a current. Lambie *et al*. determined resistances (2-50 kΩ) for common electrolytes and electrode sizes and shapes and used this information to prescribe conditions for electroporation using carbon fiber microelectrodes [32]. A microinjection pipette has been used in conjunction with microelectrodes to expose the cell to a high concentration of plasmids during electroporation, resulting in a successful transfection [58-59]. Moreover, the microelectrode approach makes possible nanosecond pulsed electric fields (nsPEF)[50]. Figure 1.3 shows the the nsPEF SCEP system. The nanosecond pulse is produced by a Blumlein line generator, a special configuration built from two coaxial cables and a resistor to match the impedance between the two microelectrodes. Because of the charging time (τ in the Schwan equation) nsPEF SCEP requires much higher voltage than the more common millisecond pulse SCEP. A voltage of 540-580 V, corresponding to an electric field of 12 kV/cm, is required to electroporate mammalian cells with a pulse duration of 60 ns.

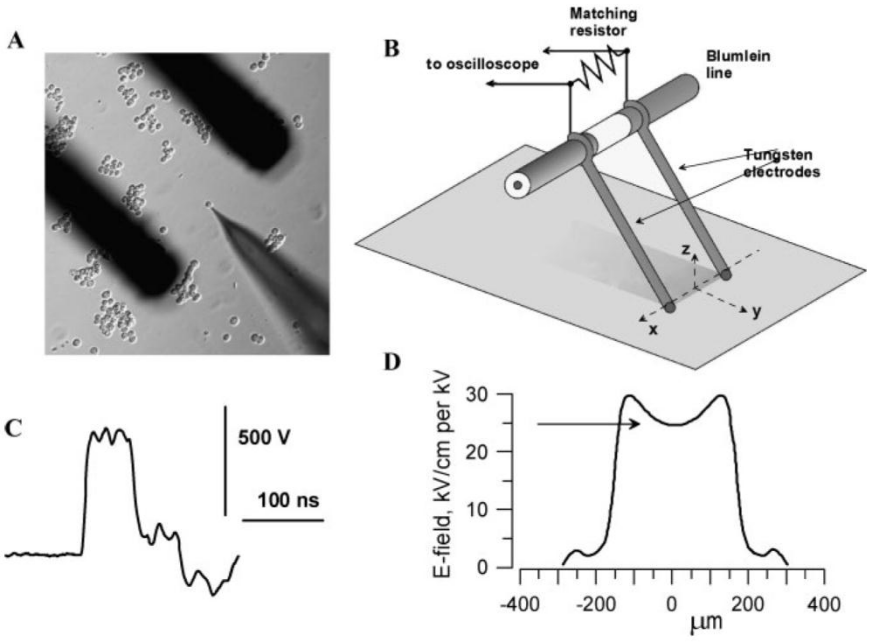

Figure 1.3 NsPEF exposure of individual cells

A: positions of pulser electrodes and a glass micropipette in contact with exposed cell, as viewed via the microscope. B: A sketch of the nsPEF delivery system(not to scale).C: Typical nsPEF trace. D: E-field distribution along the X-axis at Z=0 and Y=0, as calculated with Amaze-3D.The field at the cell location is denoted by the arrow. Reproduced by permission of John Wiley and Sons from Ref. [50]

Although SCEP with microelectrodes has a very high success rate, one concern is that cytotoxic products, such as reactive oxygen species (ROS), and gases are produced at the electrode – especially when long pulse durations and short cell-electrode distances are used. Thus, several groups have turned to micropipette and EFC approaches to SCEP for maintaining cell viability after exposure to the electric field. Micropipettes have been widely applied to the SCEP of tissue cultures. Here, the field is applied with a solute-filled micropipette made of filament fused glass with a metal electrode inside. Usually the micropipette is pushed against a target cell to increase the lateral membrane tension that lowers the required voltage. Molecules for delivery into the target cells can be in the electrolyte solution inside the micropipette. As the

volume is small (less than 1 μL) this conserves material. The same micropipette can also been used for electrophysiological recording [60]. The micropipette tip diameter is typically 0.5-2 μm, which is also the standard size for patch-clamp recordings. A pulse of 10 V with a duration of 1 ms electroporates cells. Nevertheless, larger tip openings are also used with larger voltage pulses. Uesaka, for example, used a tip diameter of 30-50 μm and 200-300 μm for *in vitro* morphological and electrophysiological study of neurons in rat brain, including cortical and thalamic explants[61-62]. The micropipette approach was first performed by Haas *et al*. on single neurons and glia in the brain of intact *Xenopus* tadpoles *in vivo*, and rat hippocampal slices *in vitro* [36]. Figure 1.4 shows the setup. A silver wire placed inside the filament micropipette having a tip diameter of 0.6–1 μm filled with loading solution was connected to a silver electrode in the circuit. The transfection efficiency in this approach is relatively low. The optimization of electric parameters led to a transfection efficiency of 20% *in vivo*.

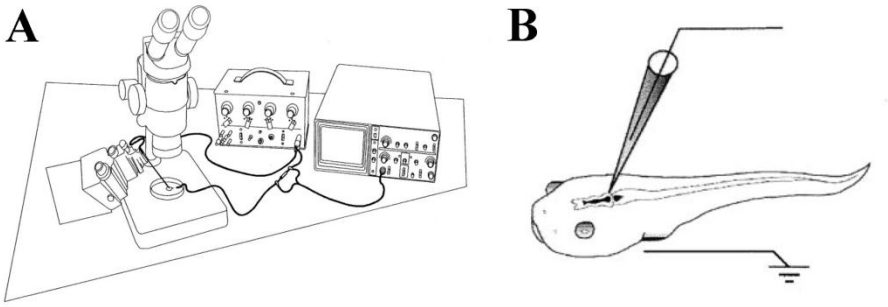

Figure 1.4 SCEP of slices with micropipette

(A) The SCEP setup. The current passing through this circuit can be monitored by measuring the voltage drop across a known resistor with an oscilloscope. (B) SCEP of neurons *in vivo* was carried out by inserting a glass micropipette filled with DNA solution into the tadpole brain. Stimulation delivered between the micropipette and an external ground electroporated a single cell at the micropipette tip. Reproduced by permission of Elsevier from Ref. [36]

Permeabilization efficiency can be improved by accurate positioning of the micropipette on a cell. To do this, Rae applied modified patch-clamp techniques [63]. A cultured cell was

indented by a micropipette having a pulled tip ~ 0.5 μm in diameter while the resistance was monitored. When the resistance increased by 25%, the electroporating potential pulse was applied. This method allowed accurate positioning of micropipette tips on the target cells without traditional visualization. A gene insertion success rate of 60–100% was obtained. Alternatively, Rathenberg used two-photon microscopy for real-time visualization at the cellular level when electroporating single cells in neurons using fluorescently labeled oligonucleotides and plasmid DNA (Figure 1.5), which led to an efficiency of 50-80% [64]. This technique has been successfully applied for SCEP of neurons *in vivo* [47].

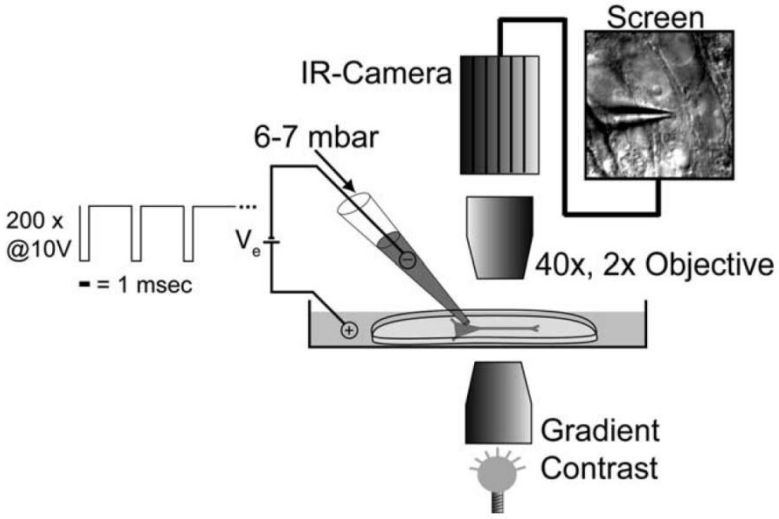

Figure 1.5 Illustration of the modified SCEP-mediated transfection setup

The culture was placed in a perfusion chamber and visualized using gradient-contrast illumination and IR video microscopy. Individual neurons can be identified on the monitor screen. The DNA filled micropipette can be targeted precisely to the membrane of a single soma. Reproduced by permission of Elsevier from Ref. [64]

The throughput of SCEP on adherent cells and tissues is an issue. Automation of SCEP can help to increase the throughput. Bae proposed an automated SCEP on adherent cells using the modified patch micropipette method [65]. A LabVIEW program was designed to carry out

computer control of micropipette positioning, cell identification, electroporation pulse trigger-on and data acquisition. Further automation has been obtained by coupling the above idea with a biomanipulator, composed of multiple motion stages which carry out routine tasks, such as scanning, positioning cells for injection, and autofocusing [66]. This approach has been successfully applied on SCEP of sea urchin eggs. Micropipette-cell positioning is based on a feedback system using the micropipette resistance. No further application has been reported except on the sea urchin eggs which have relatively large diameters of 80 μm.

Fused-silica capillaries filled with electrolyte (EFC) are also favorable for SCEP. The main difference between EFC and micropipette is that EFC is placed away from target cells at a distance of several microns. Also, the tip diameters tend to be larger in the EFC experiments, although this is not a requirement. Similar to the micropipette method, use of an EFC minimizes the volume of loading solute, and is capable of high spatial resolution when the physical dimension of the tip is small enough. Less cell trauma than for micropipettes is expected, because there is no physical force on the cell from the tip. Because the EFC is not touching the cells during the electroporation, the patch-clamp whole cell recording method can also be used to provide the transient pore information. A minor disadvantage is that a longer pulse duration and a higher voltage are required because of high resistance inside EFC.

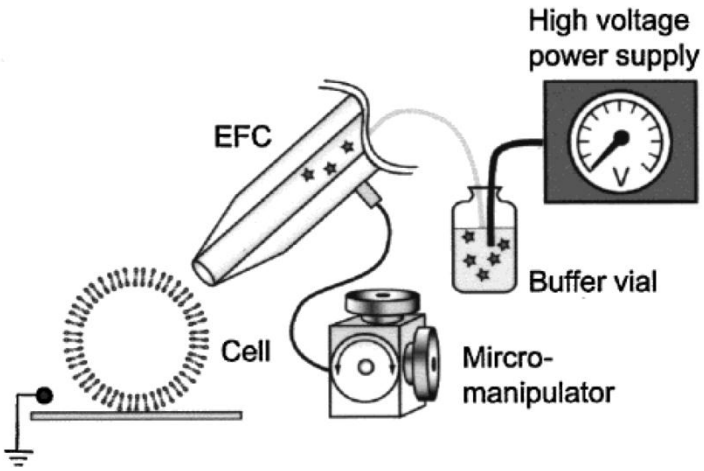

Figure 1.6 SCEP with EFC: schematic picture of the experimental setup

Reproduced by permission of American Chemical Society from Ref. [67]

Figure 1.6 shows a typical experimental setup of SCEP using EFC built by the Orwar group [67]. An EFC (30 cm long, 375 μm in outer diameter, 30 μm in inner diameter) with outlet end tapered to an outer diameter ~ 50 μm was placed 5 μm away from the cells. A large-voltage pulse (2 kV-10 kV, duration 5 s) applied across the EFC gave rise to a small electric field outside the terminus of the EFC, which caused pore formation in cell membranes. This electroporation protocol was successfully performed on both single adherent cells and small populations of cells in tissue cultures *in vitro*, and rat brain *in vivo*, with an electroporated region of 50-100 μm. Untapered capillaries with the same size need a higher voltage and a longer duration because the cell-capillary gap distance was limited to a larger value [68]. Even broader capillaries (0.4 mm inner diameter) with a lower voltage and a shorter duration have been applied for scanning electroporation [69]. The spatial resolution has been greatly improved with a pulled tip. With a tip opening of 5 μm, single cells can be electroporated without affecting the neighboring cells [33]. Even smaller sized tips of 2 μm successfully delivered plasmids filled in the tips to the electroporated cells via electroosmotic flow produced by the pulse [45]. When the pulse is applied,

the major potential drop occurs inside the capillary, and the magnitude of the electric field E decays quickly along the axis of symmetry of the EFC lumen extending out into solution. Therefore, the cell-to-tip distance is a vital factor affecting the electroporation. Selecting appropriate cell-to-tip distance according to a particular cell's size can help to maximize simultaneously the electroporation success rate and the cell's viability [33, 44]. For example, with a 15-cm long capillary having an inner diameter of 100 μm and outer diameter of 365 μm with a pulled 5-μm opening tip, when a pulse voltage of 500 V and a pulse duration of 300 ms is applied, the optimal cell-to-tip distance to obtain both high electroporation success rate and cell survival rate is 4-5 μm for cells diameter of 20-30 μm. This optimal cell-to-tip distance decreases to 3-4 μm when the cells grow to 30-35 μm.

We have discussed three efficient probes for SCEP of adherent cells and tissue. Each has its own benefits and drawbacks as addressed above. Smaller tips provide higher spatial resolution to electroporate single cells, and subcellular structures without disturbing neighboring cells, while larger tips are good for electroporation of a small group of cells. High throughput may be achieved by automation of the SCEP system with micropipettes. Molecules can be delivered into permeabilized cells by microinjection or sprayed through a second glass micropipette when using the microelectrode method, or by the aid of electroosmotic flow, electrophoretic flow and pressure at the end of the capillary for micropipette and EFC methods.

1.4.1.2 Chips

Currently microfabricated chips are under rapid development for SCEP. The majority of them are designed for suspended cells. As most cells need to adhere to a solid surface for growing, differentiation and functioning, the chips have also attracted attention for application on adherent cells. Now five types of chips are available for adherent cells, and all of them are designed to

culture cells on the substrate with electrodes either placed on the same chip, or off chip. Figure 1.7 shows a silicon chip featuring an array of 60 cell-sized gold circular electrodes to electroporate cells growing on the electrodes. Each electrode was addressed independently by a LabVIEW program, and each cell's health status could be determined by the cell/electrode impedance [53, 70]. Two similar multi-microelectrode arrayed chips have been applied for SCEP while the cells are growing over the microelectrodes. One was constructed to implant dielectrophoretic elecrodes near needle electroporation microelectrodes to allocate cells onto the designed positions during cell culture [71], while the other was built with cube microelectrodes array with the microelectrode diameters ranging from 1.2 to 4.2 μm [49]. Figure 1.8 demonstrates a simple chip built by attaching a commercially available microporous alumina membrane insert (pore size 0.02 μm) upon a thin poly-(dimethylsiloxane) (PDMS) film that has one or more holes with diameters in the one-tenth millimeter range [54]. This chip is then placed between two planar Pt electrodes for SCEP. The electric field locally focuses at the holes of the PDMS film, causing selective electroporation of cells above the holes. The size of the holes controls the electric field. The last chip, as shown in Figure 1.9, contains paired gold microelectrodes with thickened vertical sidewalls (VSW) on a glass substrate, which generates more uniform electrical fields compared to conventional planar microelectrodes [52]. The benefits of these devices are the higher throughput than the non-on-chip probes, and that other micro- and nano-scale cell analysis techniques can be incorporated on the chips. However, they can be applied only to cultures and not to cells in a tissue. And they are not capable of selectively electroporating particular single cells. For the chips constructed from substrate that is not transparent, epi-illumination has to be used for cell observation.

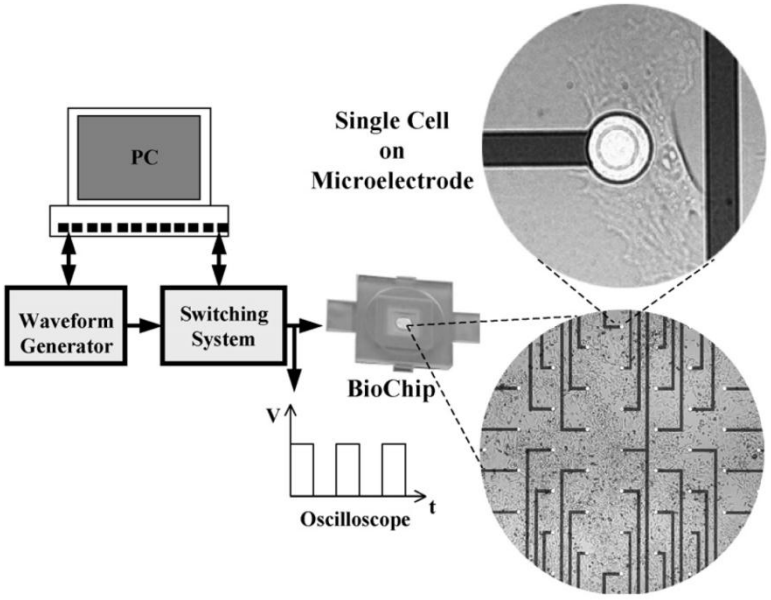

Figure 1.7 Schematics of a BioChip featuring the single-cell electroporation microarray and its control system driven by a personal computer

The control system allows, through a waveform generator and a switching system, to arbitrarily design voltage transients and to address independently each of the 60 microelectrodes of the array for single-cell electroporation. On the right side: micrograph of a culture of CHO-K1 cells on chip (right bottom). Right-top: magnification of a single cell growing in adhesion on one of the cell-sized electrodes (electrode diameter 15 μm). Reproduced by permission of Elsevier from Ref. [53]

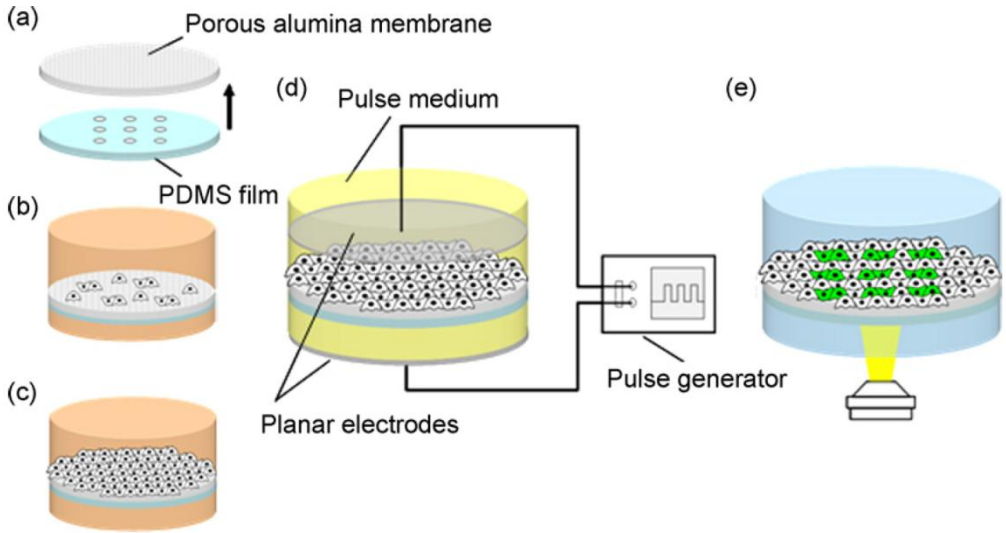

Figure 1.8 Schematics diagramming the general electroporetic protocol

(a) preparation of the membrane-based culture substrate, (b) cell seeding, (c) cell growth to confluency, (d) insertion of the electrodes and addition of pulse medium containing the molecular delivery into the chamber, and (e) microscopic imaging of the cellular sheet after electroporation. Reproduced by permission of Elsevier from Ref. [54]

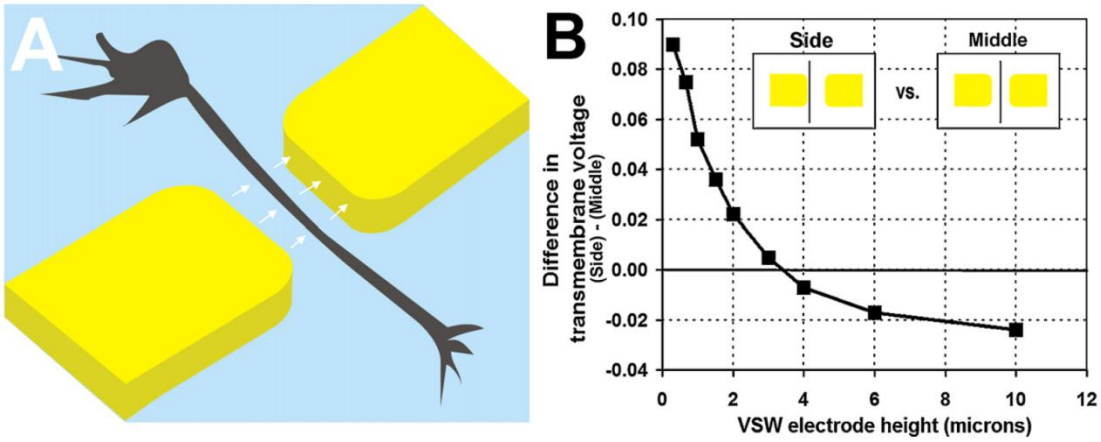

Figure 1.9 An axon (dark grey) projecting into a 10 μm gap between a vertical-side-walls electrode pair (gold)

The application of electrical fields (white arrows) in between these electrodes induces a transmembrane potential in the axon segment within the gap. (B) The transmembrane potential induced on the axon in (A) depends on where it is positioned in proximity to an electrode. This plot shows the difference in the induced transmembrane potential for the two limiting cases (shown in the inset) of (1) the axon positioned midway between electrodes and; (2) the axon positioned immediately adjacent to an electrode vs. electrode thickness. This difference is minimized when the vertical-side-walls electrode is approximately 3 μm thick. Reproduced by permission of Elsevier Ref. [52]

1.4.2 SCEP of suspended cells

Microfabricated chips are efficient devices for SCEP of suspended cells. Although with the aid of single cell capture and manipulation, suspended cells also can be electroporated with the three probes discussed above, the throughput is low. Employment of microchips for SCEP brings many merits: (1) Integration with separation and detection and single-cell analysis thereof, (2)

small loading sample amount, (3) automated SCEP can be easily developed with high efficiency and throughput, and (4) selectively trapping of specific target cells (for instance, via antibody-antigen reaction). The disadvantages are that fabrication is time-consuming with high-cost.

The various SCEP chips can be divided into three groups according to how the cells move through the device and the electroporation method. In the first group, the cells flow through the device, become trapped in a micropore (microaperture) or at the opening of a microchannel by a negative pressure. Then the cells are electroporated, and finally released. The sizes of the micro-pores (micro-apertures) and microchannels are always smaller than the cell, typically 2-6 μm. The first SCEP microchip developed by the Rubinsky group in 1999 is such a device. Using standard silicon microfabrication technology they built a vertically stacked device with two microfabricated silicon substrates bonded together with a glass cover slip [72-73]. A microhole etched through the nitride membrane connected the fluid chambers and electroporation electrodes, producing a constricted field as illustrated in Figure 1.10(A). A single cell flows to the microhole, becomes captured in the microhole by pressure difference, is electroporated by the constricted field, is loaded with exogenous compounds, and is released and replaced by the next cell. Current measurements give information about cell trapping and electroporation status as well as the breakdown voltage. An improved setup based on planar orifice arrays on a PDMS substrate, as shown in Figure 1.10(B), resulted a yield of almost 100% with 1 V pulses regardless of the cell size, shape or orientation [74]. Their group also presented a microchip (Figure 1.11) that had several electrodes in the system for detecting cells over the electroporating orifice, for electroporation and for cell lysis[75]. Membrane impermeant nucleic acid stain YOYO-1 and enhanced green fluorescent protein (EGFP) encoded plasmid were loaded into ND-1 cells with a 100% gene transfer rate with electroporation. A detailed study of

cells trapped at orifices with subcritical voltages applied revealed a current path around the cell. This path is proposed to form between the cell and the edge of the orifice. The resistance of the path is strongly temperature dependent, probably because of the temperature dependence of the membrane fluidity [76]. A 2D vibrating probe (VP) has been employed to measure the pre/during/post electroporation current density in real time through a single cell [77]. The probe consists of a parylene insulated Pt/Ir microelectrode, with a piezoelectric driver. The vibrating probe was placed near the micropore trapping the cell. Voltages measured at the two extremes of vibration yield the current density near the center point of the probe's vibrational motion.

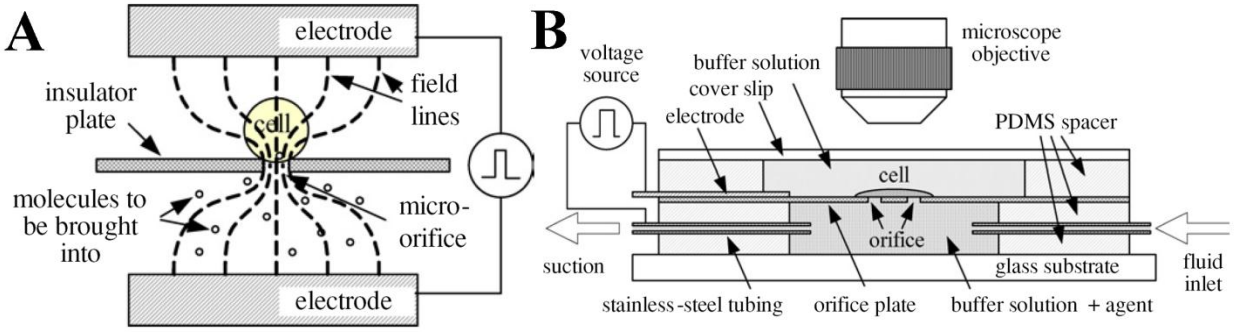

Figure 1.10 SCEP microchip based on micro-pores trapping

(A) Electroporation using the field constriction. (B) Experimental setup of a micro-orifice chip. Reproduced by permission of IOPP from Ref. [74]

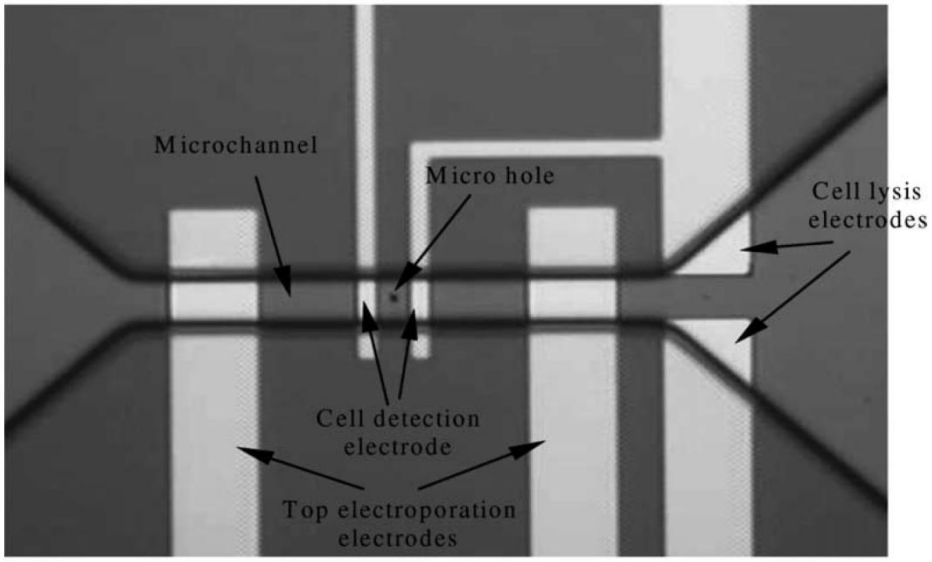

Figure 1.11 Optical image of the layout of microhole, microchannel and integrated electrodes of a flow-through microelectroporation chip with microfluidic channels for precise cell transport

Reproduced by permission of Elsevier from Ref. [75]

In 2005, the Lee group developed a PDMS microfluidic chip that can laterally immobilize and locally electroporate cells in parallel at the ends of microchannels (Figure 1.12) [78-79]. Cells were trapped by negative pressure via an attached syringe. The electrode was not incorporated on chip, eliminating production of ROS products from electrode reactions near cells. Potential drop occurred mainly in the trapped cell membrane area. HeLa cells were electroporated using low voltages (~ 0.76V) with escape of calcein and entrance of Trypan blue. This integrated, multiple patch-clamp array, microfluidic PDMS chip was later mated with a disposable bottom-less 96-well plate, enabling cells to be manipulated and monitored individually [37]. Molecules can be pre-concentrated in the microchannels and delivered into the electroporated cells by electrophoresis with a low voltage [38]. Usage of Ag/AgCl electrodes and a patch clamp amplifier allowed accurate current traces, and therefore cell resistance monitoring. Valero *et al*. presented another silicon-glass microfluidic device that traps the cells at the ends of

microchannels . The trapping sites formed at the conjunction of two channels. The cell suspension flows along the upper channel, while suction is provided by a pump on the bottom access hole at the lower channel[39].

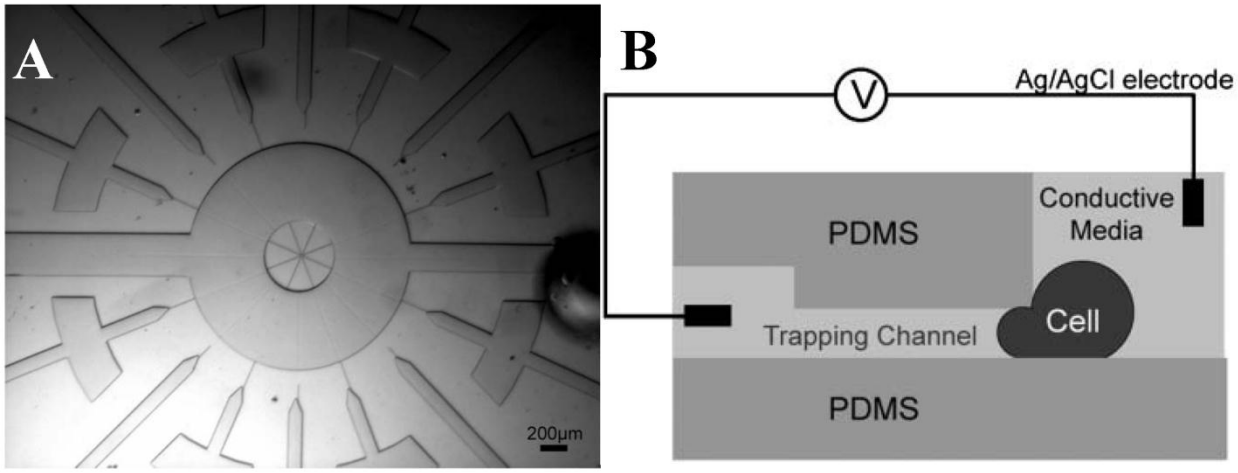

Figure 1.12 Layout of the chip and cell

(A) A multiplexed patch clamp array for high-throughput measurements. (B) A schematic view of the cross-section of the chip. Reproduced by permission of The Royal Society of Chemistry from Ref. [78]

The second group of SCEP chips employ narrow channels or microholes or other confined geometry having sizes larger than the electroporated cells but smaller than the remainder of the electrolyte path. The narrowing of the conduit focuses the electric field so that cells experience a high field merely by flowing through the narrowing region. Sarkar microfabricated a flow-through 40-μm aperture to sense and electroporate the cells analogous to the Coulter counter (Figure 1.13(A)). Cells that can pass through the aperture are identified by the impedance change, are electroporated by a pulse [80]. Wang reported a simple technique for SCEP with high throughput on a microfluidic platform (Figure 1.13(B))[81-82]. Electroporation only occurred in the narrow section of a microfluidic channel due to the local field amplification created by the narrowing. Direct current (DC) was applied for electroporation. The exposure

time of the cells to the high field was determined by the velocity of the cells and length of the section. Alteration of the geometry affected the electroporation efficiency, the longer residence time in the wide sections significantly increases the transfection yields, probably because the low electric field in the wide sections enhances the delivery of DNA into the electroporated cells [83]. This device has been applied successfully for delivery of cell-impermeant molecules and real-time cell (morphological alteration) study with a throughput of 5 cells/s [84]. Ziv *et al*. employed a similar device with an even narrower channel of 25 μm width and 200 μm in length. Cells were forced to go through the channel by a pressure difference, and electroporated with alternating current (AC). They reported that applying DC would produce bubbles which induced destruction of the cells, while using AC avoids the formation of bubbles. The cell's destruction was found to be related to the frequency of the applied AC [85]. In a recently reported simple microfluidic device for SCEP based on droplet microfluidics (demonstrated in Figure 1.14), the cells were encapsulated in 60-386 μm long aqueous droplets in oil at the junction of two channels, and electroporated by an applied voltage of 5-9 V when going through an electrode pair with a velocity of 1.38-8.86 m/min[86]. The droplet can also contain molecules for delivery into the cells within the confined space.

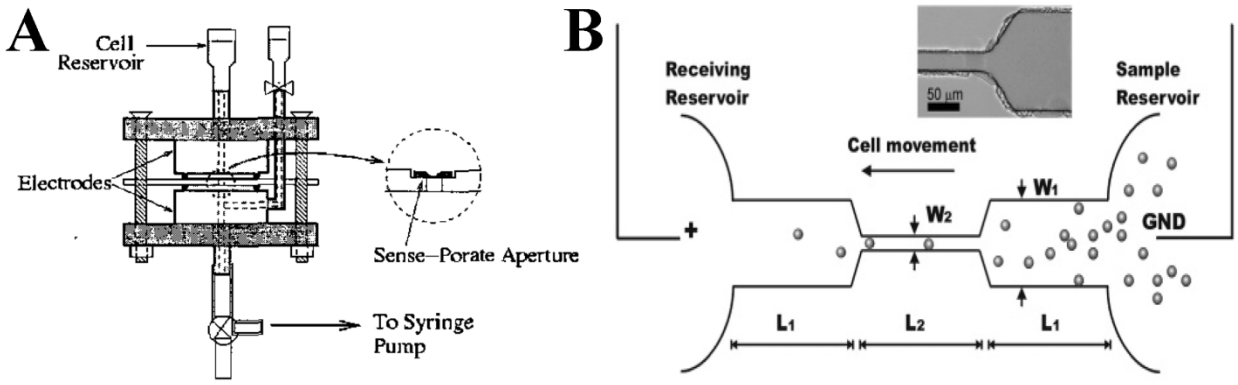

Figure 1.13 Schematics of flowing through electroporation devices

(A) Cells flowed through a tapered sense-porate aperture having a size of 40 μm. Reproduced by permission of IEEE from Ref. [80]. (B) Cells in the sample reservoir flowed to the receiving reservoir in a DC field. Electroporation was confined in the narrow section of the channel due to the amplified field inside. The inset shows a microscope image of a part of a fabricated device. Reproduced by permission of American Chemical Society from Ref. [81]

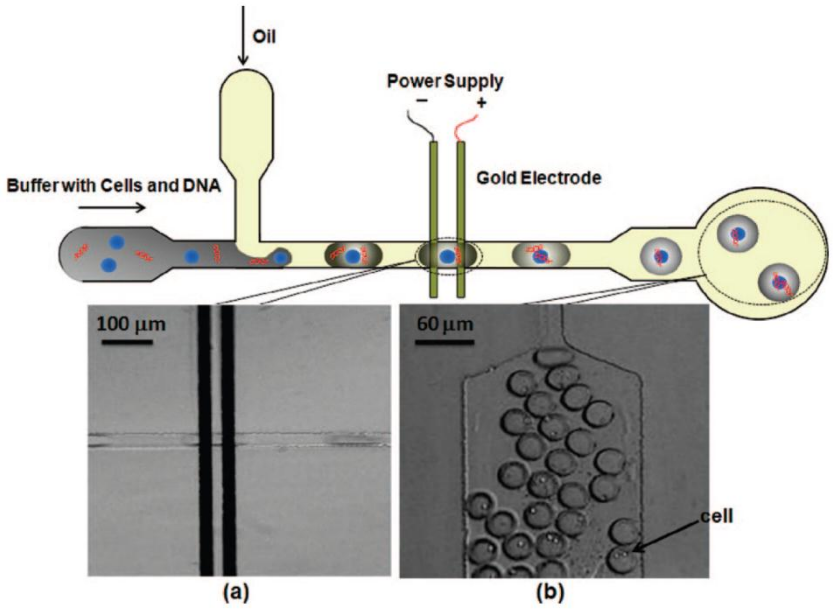

Figure 1.14 Layout and performance of the droplet-based microfluidic electroporation device

The depth of the channel was ~33 μm. Inset images illustrate the processing of the droplets at different sections of the device. (a) Cell-containing droplets rapidly flow through the two microelectrodes on the substrate (each electrode was 25 μm wide, and the distance between the two electrodes was 20 μm). (b) The droplets with encapsulated cells after electroporation at the exit of the device. Reproduced by permission of American Chemical Society from Ref. [86]

The last group of SCEP chips trap cells inside chambers between the electrodes. He *et al*. created a new micro pulsed radio frequency electroporation (μPREP) chip illustrated in Figure 1.15 [34, 87].They utilized a DC-shifted pulse oscillating at 30 kHz with a duration of 1-10 ms and an amplitude of 1-3 kV/cm to electroporate plant protoplast cells. According to their earlier

report on bulk electroporation, this pulsed radio frequency electric field has advantages over the traditional DC pulses or exponential decay pulse to improve the viability and permeability of the electroporation: it provides a sonicating effect on the cell membrane causing the breakdown of the membrane, and it can also counterbalance the cell's size effect with an opposite effect of membrane relaxation (at high oscillating frequency, the term of cell radius is removed and substituted by the inverted angular frequency for the induced transmembrane potential in Schwan equation) [88]. A large number of cells can be electroporated under different pulse conditions at the same time. Modification of the chip with higher electrodes (0.5-12 μm) increases permeabilization efficiency of the cells with a more powerful 3D electric field distribution [46]. Cho *et al.* has also designed two types of microchips composed of channels leading to a cantilever-type pair of microelectrodes, with cells captured between the electrode pair for SCEP [89]. A microchip containing saw-tooth microelectrodes built by Sedgwick *et al*. trapped cells between the electrodes by dielectrophoresis and then lysed the cells by electroporation for analysis [90]. Recently, Valley *et al.* reported an interesting device using patterned light to create virtual electrodes on photosensitive surface [91]. Figure 1.16 is the schematic of the device. The device consists of two glass substrates coated with the transparent conductor indium tin oxide (ITO). The bottom substrate is coated with a photosensitive film (α- Si:H). In the absence of light, the electric field concentrates across the highly resistive photoconductive layer. Upon illumination, electron-hole pairs appear in the illuminated areas, causing large electric fields to exist in the liquid layer wherever the device is illuminated.

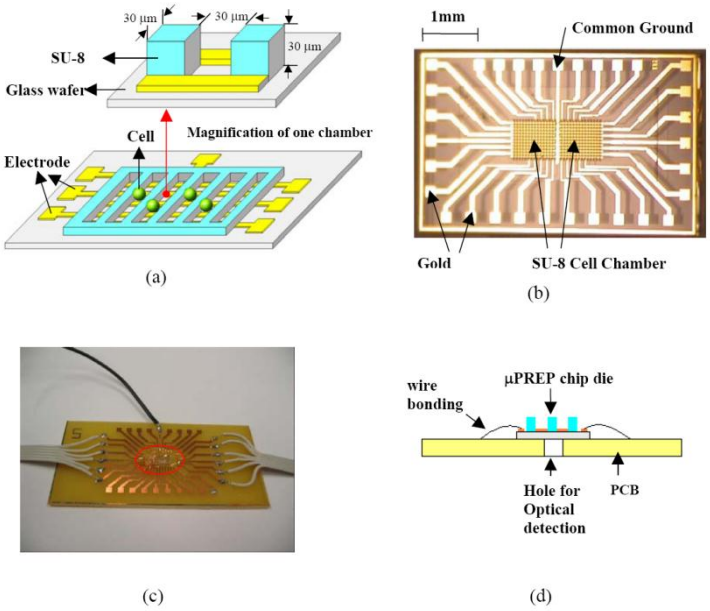

Figure 1.15 µPREP chip

(a) 3D schematic diagram of the µPREP chip, (b) a µPREP chip die. The electrodes in vertical direction were used for multiple electric field input, while those in lateral direction were for future current detection during electroporation, (c) Photograph of a packaged device. Within the red circle is the µPREP chip die which was wire-bonded on the PCB board, (d) Schematic diagram of a packaged device for optical detection. Reproduced by permission of Elsevier from Ref. [46]

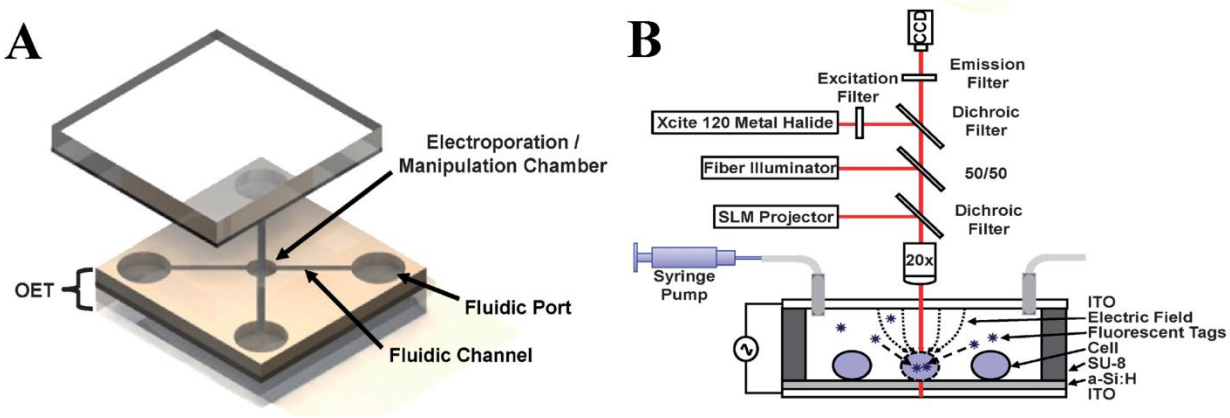

Figure 1.16 Light-induced SCEP device schematic

(a) Overall device layout where microfluidic channels define electroporation/manipulation areas and allow for perfusion of different reagents. OET and electroporation function are coupled through a change in device bias. (b)

Cross section of device showing experimental setup and mechanism of light-induced electroporation. Optical patterns cause electric field concentration across illuminated cells resulting in selective electroporation. Reproduced by permission of The Royal Society of Chemistry from Ref. [91]

1.5 APPLICATIONS

Although emerging just twelve years ago, SCEP has attracted increasing interest. SCEP is not a technique of single-cell analysis, *per se*; however, it serves as a potential tool for both destructive and nondestructive single cell analysis. Since a cell's viability can be maintained after electroporation, cell impermeant molecules such as dyes, plasmids, calcium indicators and drugs [92] can be electroloaded into specific living cells for long term, real-time study without affecting the natural behavior of the cells. Alternatively, a strong electric field can induce lysis of a single cell [90], and the contents can be analyzed with other separation and detection techniques. Delivery of plasmids into target cells has been demonstrated with high efficiency in adherent cells and tissues both *in vitro* [45, 64, 93-96] and *in vivo* [36, 42, 92, 94-95]. Introducing small interfering RNA into cells leads to the induction of functional RNA interference, and has been applied to investigate functions of genes involved in neuronal differentiation and degeneration [35, 41, 97-98]. Delivery of dyes into neurons provides an effective mean to examine the dynamic morphology [61, 99-104]. Electroloading of calcium indicator provides a powerful way to study the Ca^{2+} signaling in individual cells [105]. SCEP offers advantages over other methods of impermeant molecule delivery into the cells such as a very small amount of material is enough for delivery, the transport of molecules can be controlled according to their molecular sizes [45], the efficiency of

gene transfer is high, and particular subset of neurons can be selected for delivery within a heterogeneous cell population [106].

1.6 FUTURE WORK AND CURRENT CHALLENGES

SCEP is a promising method for many biological and medical applications. However, so far there is still a lack of understanding of the fundamental theory, which limits our ability to control and apply this technique. For example, most of the excellent theoretical papers apply to the lipid bilayer. It is difficult to factor in the effect of a cytoskeleton, or the degree to which an adherent cell's membrane properties are altered by its attachment. Besides the cell size, shape and orientation, we need further understanding of what intrinsic and extrinsic properties of the cell influence its electroporation. For adherent cells and tissues, the electroporation technique needs to be improved to achieve high efficiency with high yield. We also anticipate that further miniaturization of the probes to the nanoscale will allow selective electroporation of certain organelle inside a single cell. Another challenging future direction is combination of SCEP with currently evolving rapid, ultra small volume (picoliter, femtoliter) analytical techniques, which will allow us to study quantitatively living cells without damage.

1.7 OUTLINE

As we mentioned in the "Pore formation" section, usually micro-size probes are applied to produce limited non-uniform electric fields in SCEP. Generally any analytical solution for the

calculation of the transmembrane potential of cell membrane is not possible. Furthermore, in SCEP the effect of local geometry and the individual cell condition on cell permeabilization is amplified compared to bulk electroporation. A small alteration in the geometry, probes or cell status would induce a lot variance. Therefore statistical analysis is necessary in SCEP to reveal the origins of the variance and optimize parameters for best efficiency and survivability. So far most reports on SCEP are based on qualitative analysis. Researchers find optimized pulse conditions to obtain high efficiency RE for their specific setup, but other variables have been seldom investigated in detail.

We are using EFCs with micrometer-scaled tips for electroporation of single Human lung carcinoma A549 cells and Human prostate cancer PC-3 cells. Our aim is to make SCEP a quantitative and predictable tool for delivery and sampling/sensing of bioactive molecules without killing the target cells. To do this, we have investigated the effect of pulse parameters, characteristics of the cells, size of probe tips and other circumstantial conditions on the electroporation efficacy and cell survivability. Quantitative analysis of small molecule release is carried out to help us understand the pore sizes and kinetics. Transport of macromolecules through the transient pores is also studied and successfully applied to single-cell transfection.

Beyond the experiments, numerical models using Comsol Multiphysics finite modeling software has been set up to simulate the electroporation process based on the real geometry of the capillary. This simulation helps us to understand the mechanism and guide our experiments. A model involving multiphysics including potential, fluid flow and electrokinetic flow help us to investigate mass transfer of molecules from the capillary to the electroporated cells, and predict the delivery of target molecules into the cells based upon their particular molecular characteristics.

2.0 SINGLE-CELL TRANSFECTION BY ELECTROPORATION USING AN ELECTROLYTE/PLASMID-FILLED CAPILLARY

This work has been published in *Analytical Chemistry*, 2009, 81(10), 4060-4067. Reproduced with permission from *Analytical Chemistry.*

2.1 ABSTRACT

Single-cell transfection of adherent cells has been accomplished using single-cell electroporation (SCEP) with a pulled capillary. HEPES-buffered physiological saline solution containing pEGFP plasmid at a low concentration (0.16 ~ 0.78 μg/μL) filled a 15 cm long capillary with a tip opening of 2 μm. The electric field is applied to individual cells by bringing the tip close to the cell and subsequently applying one or two brief electric pulses. Many individual cells can thus be transfected with a small volume of plasmid-containing solution (~ 1 μL). The extent of electroporation is determined by measuring the percentage loss of freely diffusing thiols (chiefly reduced glutathione) that have been derivatized with the fluorogenic ThioGlo 1. A mass transport model is used to fit the time-dependent fluorescence intensity decay in the target cells. The fits, which are excellent, yield the electroporation-induced fluorescence loss at steady state and the mass transfer rate through the electroporated cell membrane. Steady-state fluorescence loss ranged approximately from 0 to about 80% (based on the fluorescence intensity before

electroporation). For the cells having a loss of thiol-ThioGlo 1 fluorescence intensity greater than 10%, and mass transfer rate greater than 0.03 s^{-1}, EGFP fluorescence is observed after 24 hours. The EGFP fluorescence is increased at 48 hours. With a loss smaller than 10% and a mass transfer rate smaller than 0.03 s^{-1}, no EGFP fluorescence is detected. Thus, transfection success is closely related to the small molecule mass transport dynamics as indicated by the loss of fluorescence from thiol-ThioGlo 1 conjugates. The EGFP expression is weaker than bulk lipid-mediated transfection, as indicated by the EGFP fluorescence intensities. However, the success with the single-cell approach is considerably greater than lipid-mediated transfection.

2.2 INTRODUCTION

Studies on single cells are becoming the frontier of biochemical research. Effective and reliable single-cell transfection technologies have great value to construct single-cell models, and control biochemistry at the single-cell level. Besides the traditional carrier-mediated and plasma-membrane permeabilization protocols which require that individual cells are isolated for individual cell gene delivery, microinjection techniques using ultra-small probes (glass needles [107], nanoneedles [108], femtosyringe [109] and AFM tips [110]) with the naked DNA plasmid either inside or surrounding the probes have been successfully used for single-cell transfection. However, all these microinjection techniques rely on penetrating the cell membrane with a probe which will induce physical damage to the target cells. One solution to this problem is to use a focused femtosecond near-infrared laser beam to facilitate DNA intake, causing little cellular damage [111].

Although electroporation is an established method for gene delivery into cells in suspension and tissues, there is a limited number of reports on single-cell transfection by single-cell electroporation (SCEP). The first success in single-cell transfection by SCEP was to introduce the plasmid vector pRAY1 into individual COS 7 cells using carbon fiber microelectrodes [55]. One significant limitation in the microelectrode approach to SCEP is the potential for the electrode to form cytotoxic products such as reactive oxygen species (ROS). Plasmid/buffer-filled glass micropipettes containing a metal electrode have been developed and applied for plasmid DNA delivery into single cells [35-36, 47, 63-64]. In this case, a glass pipette connected to a voltage supply through a metal wire inside is pushed against the target cell, and an external pressure is applied to push the plasmid-containing solution in the micropipette into the target cell during the application of electrical pulses. Hass *et al*. reported the first use of micropipettes for SCEP. They used micropipettes with openings in the 0.6-1 μm range for single cell transfection with plasmids encoding enhanced green fluorescent protein (EGFP) and DsRed in the brain of intact *Xenopus* tadpoles and rat hippocampal slices [36]. Their highest transfection efficiency was only 30% after optimization of the pulse protocols. The poor transfection efficiency has been improved in two different approaches that are based on electroinjection *i.e.* the plasmid-filled capillary is in direct physical contact with the cell membrane. First, Rae and Levis pressed a smaller (0.5 μm) tip onto the target cells while monitoring the resistance increase [63]. Second, Kitamura *et al.*, coupled the whole-cell patch-clamp technique with two-photon microscopy [64] for *in vivo* transfection of neurons with plasmid encoding EGFP [47]. This micropipette method was also successfully applied to the delivery of RNA into neurons recently by Boudes *et al.* [35]. Despite the above advances, problems arise, as addressed by Rae and Levis, from the cell damage caused by indenting, micropipette tip clogging, and cell adhesion to the tips

after pulses. Recently, microchips coupling microelectrodes have been designed for high throughput SCEP and show promising results for gene delivery into singe cells [39, 53, 83]. However, this approach is not suitable for adherent cells, tissue slices, tissue cultures, or *in vivo* applications. Although many papers have reported the effect of the electrical pulsing protocol on plasmid transfer during SCEP or bulk electroporation [53, 63, 112], nobody has tried to correlate cell membrane permeability to small molecules with DNA delivery.

As we have shown previously [33, 113], exposing cells to the thiol-reactive fluorogenic reagent, ThioGlo 1 leads to intracellular fluorescence, chiefly from the freely diffusible reduced glutathione (γ-Glu-Cys-Gly, GSH). Thus, in this work, we follow the loss of intracellular fluorescence (from ThioGlo 1-labeled thiols) from single cells being electroporated with a pEGFP-C2 plasmid-filled capillary with fine tips. The results show that this method of gene delivery is effective, and that gene delivery into cells is related to the extent of electroporation as indicated by the extent of labeled thiol loss from cells.

2.3 MATERIALS AND METHODS

2.3.1 Materials

The chemicals used for buffers were all of analytical grade and purchased from Sigma (St. Louis, MO). The HEPES-buffered saline solution, which we will call ‘extracellular buffer’, consisted of NaCl (140 mM), KCl (5 mM), MgCl2 (1.5 mM), CaCl2 (2 mM), D-glucose (10 mM) and HEPES (20 mM). The pH was adjusted to 7.4 with 0.5 M NaOH and the buffer was filtered with 0.45 μm nylon filters prior to use. Plasmid pEGFP-C2 vector (donated by Dr. Michael Trakselis)

was precipitated with ethanol and resuspended in extracellular buffer to a final concentration of 0.16-0.78 μg/μL (measured by UV absorbance at 260 nm). Thioglo 1 was purchased from Covalent Associates (Woburn, MA). A549 cell lines were obtained from American Type Culture Association (Manassas, VA). Basal medium Eagle (BME), 0.25% trypsin-EDTA, One ShotTM fetal bovine serum (FBS), L-glutamine, and penicillin-streptomycin solution were all obtained from Invitrogen, GIBCO (Carlsbad, CA). Milli-Q (Millipore Synthesis A10, Billerica, MA) water was used. Pt wires (diameter 0.5 mm, high purity 99.99+ %) were purchased from Goodfellow (Oakdale, PA).

2.3.2 Cell culture and preparation

A549 human lung carcinoma cells were cultured for transfection. The culture medium was prepared by adding 50 mL FBS, 5 mL 200 mM L-glutamine and 5 mL 10,000 units/mL penicillin-10,000 μg/mL streptomycin to 500 mL BME. Cells were grown in 75-cm2 cell culture flasks (Nunc* Sterile EasYFlask) in a CO_2 incubator (HERA cell incubator, Newtown, CT) at 37 ℃ and 5% CO2/95% air, and were subcultured when reaching ~ 80% confluence every 3-4 days. Before the experiments, cells were seeded on 35-mm gridded uncoated glass-bottom cell culture dishes (MatTek Corp., Ashland, MA) at a seeding density of 1×10^4 cells/dish. Experiments were performed on the second and third days following the cell plating.

2.3.3 Thioglo 1 staining for electroporation visualization

A stock solution of ThioGlo 1 was prepared at a concentration of 0.5 mM in pure DMSO and stored in a desiccator at -20 °C in the dark. A 2 μM ThioGlo-1 loading solution was freshly

prepared by diluting 2 µL ThioGlo 1 stock solution with 0.5 mL extracellular buffer before staining the cells. For staining, each cell dish was first washed 3 times with extracellular buffer. Following the washing step the cells were exposed to 0.5 mL ThioGlo 1 for 30 s at room temperature. The cell dish was washed again with extracellular buffer and finally bathed in 2 mL extracellular buffer for electroporation.

2.3.4 Capillary fabrication

The fabrication of electrolyte-filled capillaries (EFC) with pulled tips was done in a laminar flow hood. Fused-silica capillaries from Polymicro Technology (Phoenix, AZ) with an outer diameter of 360 µm and an inner diameter of 100 µm were used. Capillaries were pulled at one end by using a CO_2 laser puller (Sutter Instruments Co. P-2000, Novato, CA). Before the capillary was pulled, a 2-cm-center section of a 35-cm-long capillary was burned with a flame to remove the protective polyimide coating, and then the capillary was flushed with pre-filtered (by 0.2 µm syringe filter) Milli-Q grade water. These capillaries were pulled to create reproducible capillaries with a short pulled tip having an opening inner diameter of ~ 2 µm. Before the experiments the capillaries were carefully truncated with a Shortix™ fused-silica tubing cutter to get a final length of 15 cm.

2.3.5 Microscope imaging

The cell dish was fixed in a cell chamber (DH 35i culture dish incubator, Warner Instruments, Holliston, MA) mounted on the stage of an inverted fluorescence microscope (Olympus IX 71, Melville, NY) coupled with a CCD (ORCA-285 IEEE 1394 -Based Digital Camera, B & B

Microscopes Limited, Pittsburgh, PA) for fluorescence imaging. A Cermax 175 W Xenon Arc lamp (PE175BF, PerkinElemer Optoelectronics, Fremont, CA) in the microscope was used as the excitation source. Cells were observed through a 20× 0.70 NA UPlanApo objective lens (Olympus). Image processing was performed by the image acquisition software SimplePCI from Compix Inc (Sewickley, PA). Fluorescence intensities of regions of interest were corrected by subtracting the average fluorescence intensity of four nearby background regions.

For Thioglo 1, an Omega fluorescence filter cube (especially built, exciter XF1075-387AF28, dichroic XF2004-410DRLP, emitter XF3087-480ALP, Omega Optical, Brattleboro, VT) was used for excitation at 378 nm and emission at 480 nm. For EGFP imaging, a U-MWIB2 filter set from Olympus (Exciter 460-490, emitter 510IF, dichroic 505) was used.

2.3.6 Experimental circuit and electronics

The experimental setup is depicted in Figure 2.1. It has two switchable circuits: an electroporation circuit and a test circuit. When doing experiments, the test circuit (described below) helps to examine the status of the capillary. Once the capillary is placed near a cell, the switches are thrown to activate the electroporation circuit (described below) for electroporation accompanied by current monitoring.

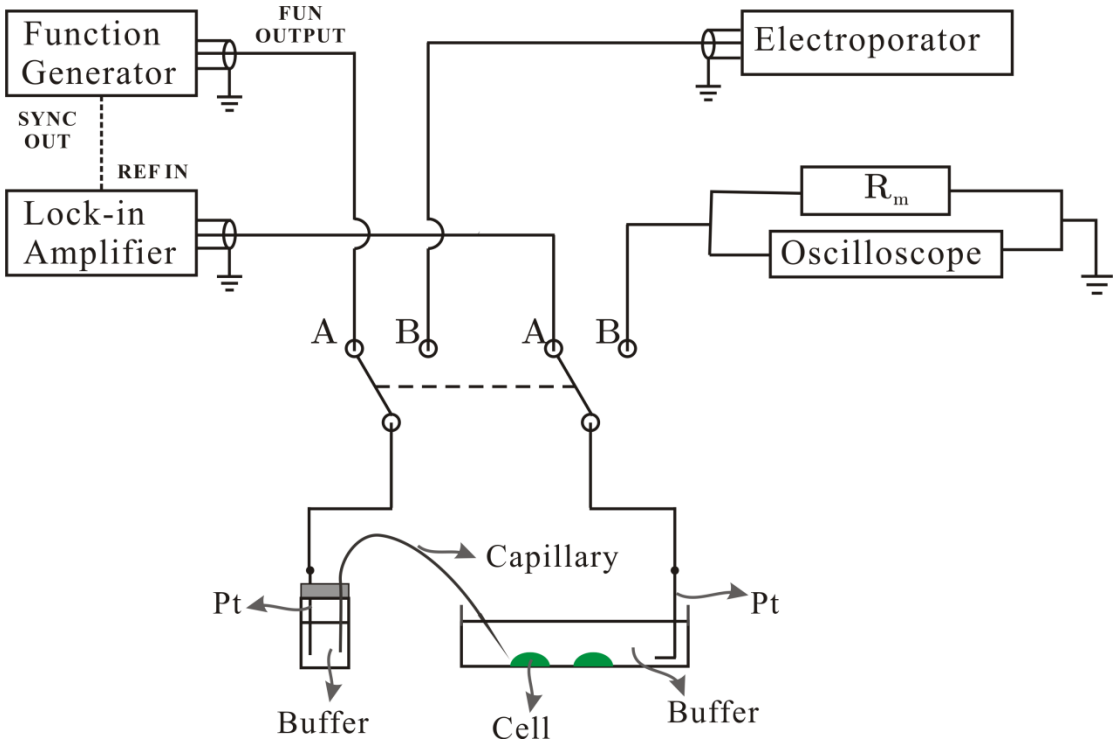

Figure 2.1 Schematic diagram of the experimental setup.

Either of two circuits, electroporation with current monitoring, or the test circuit, may be used by throwing a switch. By switching from A to B, the active circuit converts from the test circuit to the electroporation circuit. A multipostion rotary selector switch shelled in a grounded box is used for switching. (1) Switch position at A. The test circuit is on. The function generator produces a 2 V (rms) sine wave at 100 Hz. The resulting current goes through the same path taken by the current during electroporation including the interface of Pt with the electrolyte, its container, the capillary, the pulled tip, the cell dish filled with buffer, and the other electrolyte/Pt interface and to ground through a current-to-voltage converter in a lock-in-amplifier. The lock-in amplifier has its reference input connected to the signal output of the function generator, thus locks on the 100 Hz frequency and gives a current reading at this specific frequency. This circuit is used for capillary and connection testing. (2) Switch position at B. The electroporation circuit is on. An electroporator provides a high voltage pulse applied for electroporation by pushing a trigger button. The current goes through the same electrode and electrolyte path as described above. It goes to ground through a resistor and an oscilloscope in parallel. The oscilloscope is used to examine the pulse shape and magnitude as well as monitoring the current going through the electroporation circuit.

2.3.6.1 Electroporation circuit

When the switches were put in position B, the test circuit was inactive. The 15-cm-long pulled capillary was positioned using a MP-285 motorized micromanipulator from Sutter (Novato, CA). The tip end was carefully placed near the target cell at a desired distance. The other end of the capillary was inserted into a vial filled with extracellular buffer. A platinum electrode placed in this vial was connected to the electroporator (BTX ECM 830, Harvard Apparatus, San Diego, CA), and the electrical circuit was completed with another platinum electrode in the cell dish connected to ground through a 100 kΩ resistor, Rm. The voltage across the resistor created by the electroporation current was measured with a digital oscilloscope (NI 5911 Digital Oscilloscope for PCI, National Instruments Corp. Austin, Texas) for current monitoring.

The added resistor was chosen to be 100 kΩ in order to avoid exceeding the maximum voltage for the oscilloscope, 10 V, while maximizing the signal/noise ratio. Since the resistance of EFC was always > 10 MΩ, the extra 100 kΩ resistor barely affected the electroporation current. The current during electroporation is thus given by,

$$I \approx \frac{V_{O\prime}}{R_m \times R_{O\prime}/(R_m + R_{O\prime})} = \frac{V_{O\prime}}{0.091\ M\Omega} \qquad (2.1)$$

2.3.6.2 Test circuit

The test circuit was used to assess the status of the tip opening. The function generator (SRS Model DS 340, Stanford Research Systems, Inc., Sunnyvale, CA) gave a continuous 2 V AC signal at 100 Hz. This signal passed through the EFC and cell dish and was finally sent to a low input impedance (1 kΩ) current-to-voltage converter that is an integral part of the lock-in amplifier (SRS Model SR 830 DSP). The lock-in amplifier measured the magnitude and phase

angle of the current at 100 Hz. The magnitude of the current primarily reflects the resistance of the capillary tip.

2.3.7 Electroporation

A cell dish containing adherent A549 cells stained with Thioglo 1 was mounted in the cell chamber on the microscope and connected to the electroporation circuit. The capillary tip was placed at an angle of 45^{o} with respect to the dish surface with a tip-to-cell distance d_m of about 3-5 μm and a distance to the dish surface of about 4 μm. The distance d_m was determined with the help of a scale bar to visually estimate the distance between the projection of capillary tip in the horizontal imaging plane and the projection of the edge of the cell in the horizontal imaging plane. It was chosen according to the size of a particular cell in order to achieve electroporation without inducing cell death [33]. To be specific, for the capillaries with 2 μm opening, the A549 cells we electroporated had a size distribution of 17 ~ 42 μm in diameter. This cell 'diameter' is calculated (SimplePCI) from the area, A, in pixels as $(A/\pi)^{1/2}$. For a cell diameter < 20 μm, d_m was set to 6 μm. For diameter of 20 ~ 27 μm, d_m was 5 μm, and d_m was 4 μm when the cell's diameter went greater than 27 μm. Two types of pulses were used for electroporation: one was a single, 300-ms 500 V dc pulse which we called the single-pulse method, and the other is 2×150 ms 500 V dc pulses with an interval of 150 ms referred to as the two-pulse method. For each cell dish, one capillary filled with plasmid/extracellular buffer was used for SCEP of a number of cells. Fluorescence images were captured every second during the electroporation process. The grids on the dish surface helped to record the electroporated cells' positions for tracking. After electroporation, the cell dish was allowed to rest *in situ* for 20 minutes. Following the twenty-minute resting period, the extracellular buffer in the cell dish was replaced with 2 mL of BME

and the cell dish was transferred back to the CO_2 incubator. After overnight culture the cells were washed 3 times with extracellular buffer and checked for EGFP fluorescence under the fluorescence microscope. The cells were returned to the incubator (in BME) for one more day following which fluorescence micrographs for EGFP fluorescence were recorded.

2.3.8 Lipofectamine-mediated bulk transfection

The Lipofectamine 2000 transfection experiment was carried out following the general protocol (Invitrogen Lipofectamine 2000 technical manual, see Supporting Information for our particular procedure).

2.3.9 Data analysis

A quantitative model for loss of whole-cell thiol-ThioGlo1 fluorescence intensity was fit to the data based on a nonlinear least squares routine in Mathcad (‘genfit’). The fit quality was judged by the coefficient of determination, R^2. The resulting estimates of the variables were used to perform further statistical studies to reveal the relationship between the transfection efficiency and the pore kinetics.

2.4 RESULTS AND DISCUSSION

2.4.1 Capillary tip sizes and resistances

We measured the resistance for capillaries with different tip sizes. EFC tips with a 2-μm opening had currents of 0.12 - 0.13 μA, corresponding to a resistance of ~ 16 MΩ, and tip openings of 4 μm, gave currents of 0.13 - 0.14 μA corresponding to a 14 MΩ resistance. These experimentally obtained resistances were very close to the calculated values (Comsol version 3.4, data not shown). If the capillary was clogged, the current decreased substantially. In this way we were able to confirm the integrity of the capillary before carrying out electroporation by simply reading from the lock-in amplifier. All of our prior work has been with 4-5 μm tips [33, 113]. Preliminary experiments indicated that these were not suitable for transfection (no cells transfected out of 16). We have fortunately found that 2 μm tips are effective. We have not investigated why the diameter makes a difference.

2.4.2 Thioglo 1 staining for observation of electroporation in real time

To make sure electroporation occurs when attempting to deliver plasmid DNA into A549 cells, we used cell-permeable Thioglo 1 for observation of the electroporation process. Thioglo 1 is a non-fluorescent maleimide-based reagent that gives a green fluorescent product upon its reaction with active SH groups [114]. As the predominant thiol in cells is GSH, the majority of the fluorescence can be ascribed to the GSH-Thioglo 1 adduct. Thus, Thioglo 1 can be used for detection and titration of GSH [115]. The Thioglo 1-GSH conjugate has an absorbance λ_{max} at 379 nm and emission λ_{max} at 513 nm. Low concentrations of Thioglo 1 (< 10 μM) are reported to be

non-cytotoxic [115]. Nevertheless, the depletion of GSH may induce cell death, especially under the stress of oxidants produced accompanying fluorescence. Interestingly, it was reported that even with a 90% depletion of GSH, mammalian cancer cells remained viable [116]. Differences in the fluorescence spectra of EGFP and the Thioglo 1-GSH adduct ensure that the fluorescence from the Thioglo 1-GSH adduct will not interfere the observation of EGFP fluorescence (See Supporting Information for absorbance and emission spectra of EGFP and Thioglo 1-GSH adduct). One parameter that we measure is the whole-cell loss of fluorescence of Thioglo 1 adducts following electroporation, ΔF.

2.4.3 Single-cell transfection following electroporation

Using this SCEP method, we have successfully delivered pEGFP-C2 plasmid into A549 cells with an extracellular buffer/ plasmid-filled capillary having a pulled tip with a 2 μm opening. Figure 2.2 shows an example of SCEP of an individual cell and Figure 2.3 shows the subsequent EGFP expression inside this cell. A capillary was positioned 5 μm away from the target A549 cell with two cells nearby (Figure 2.2A). These cells were pre-stained with Thioglo 1, thus displaying strong green fluorescence (Figure 2.2B). Then a two-pulse train (2×150 ms pulse train with an interval of 150 ms and a voltage of 500 V) was applied to the capillary, causing electroporation of the target cell and loss of the green fluorescent Thioglo 1-GSH adduct through the transient pores in the membrane. Figure 2.2C shows a weaker fluorescence for the electroporated cell after electroporation, while the surrounding cells have no obvious change in fluorescence intensity. Figure 2.2D displays the fluorescence intensity decay of the target cell upon electroporation. At t = 9 s the pulse was applied. The fluorescence decays very rapidly in the beginning then slows down in an exponential way as the pores seal (a video file of the

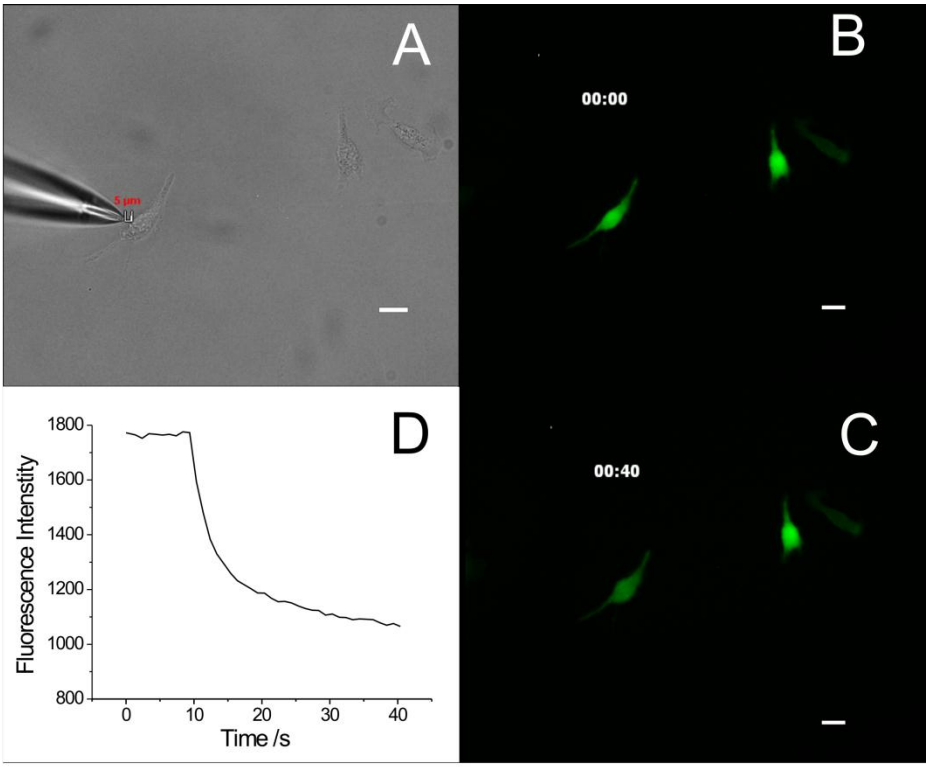

Figure 2.2 Electroporation of a target A549 cells.

(A) Bright field image of the capillary and A549 cells in a cell dish before electroporation. A 2-μm opening capillary tip filled with extracellular buffer/pEGFP-C2 plasmid is placed from the left of the target cell with a d_m of 5 μm. (B) Thioglo 1-GSH adduct fluorescence image of the cells before the pulse. (C) Thioglo 1-GSH adduct fluorescence image of the cells 40 s after the pulse. (D) The target cell Thioglo 1-GSH adduct fluorescence decay curve. Fluorescence intensity drops suddenly when the pulse is trigged followed by a slow decay while the transient pores reseal. (All images taken using a 20× objective, scale bar 20 μm)

electroporation is included in Supporting Information). After 24 hours of incubation in BME, the cell subjected to electroporation showed fluorescence from EGFP, while the other, untreated surrounding cells showed no EGFP fluorescence (Figure 2.3A & 2.3B). The EGFP fluorescence in the target cell increased after 48 hours (Figure 2.3C). This demonstrated successful delivery and expression of pEGFP-C2 plasmid in the target cell through electroporation. We note that the transfected cell is in the same position as it was when it was electroporated. This is common.

Occasionally, a cell expressing EGFP was found at a different location on the coverslip than the electroporated cell occupied at the time of electroporation. The electroporated cell is, in such cases, considered not to have been transfected. In our experiments, we noted that the fraction of cells that are missing from their original grid positions (following 24 h incubation) is correlated with the electroporation conditions. We believe that cells are lost primarily by necrosis and migration caused by high electric field exposure. For this study, we have assumed that all lost cells have died.

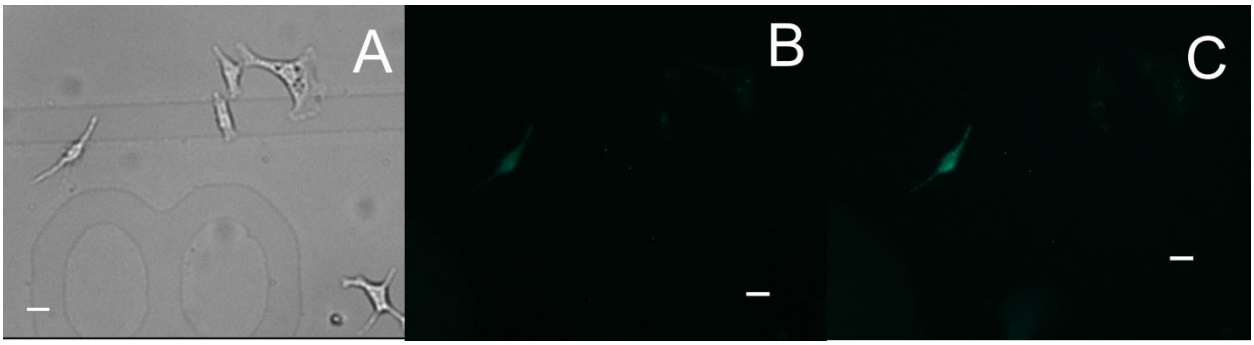

Figure 2.3 Transfection following electroporation.

(A) Bright field image of the target A549 cell and surrounding cells in cell dish 24 hours after electroporation. (B) EGFP fluorescence image of the target cell and surrounding cells as displayed in (A) 24 hours after electroporation. Only the electroporated cell shows EGFP fluorescence. (C) EGFP fluorescence image of the target cell and surrounding cells 48 hours after electroporation. The electroporated cell shows increased EGFP fluorescence over the image at 24 hours. (All images taken using a 20× objective, scale bar 20 μm)

2.4.4 Electrokinetic phenomena during electroporation

Electroosmotic flow plays an important role in plasmid delivery in our electroporation protocol. As shown in Figure 2.1, the ground Pt wire is the cathode so the electrode at the distal end of the capillary is the anode. This results in two opposing fluxes: electroosmotic flux goes in the

direction of capillary → target cell →ground while the electrophoretic flux goes in the opposite direction because of the negative charge of plasmid DNA. The observed linear velocity of plasmid DNA is thus given by

$$\upsilon_{obs} = \left(\mu_{ep} + \mu_{eo}\right) E = \left(\frac{\varepsilon\zeta_{DNA}}{\eta} - \frac{\varepsilon\zeta_{wall}}{\eta}\right) E \qquad (2.2)$$

where μ_{ep} is electrophoretic mobility, μ_{eo} is electroosmotic mobility, ε is the permittivity of the buffer solution, η is the dynamic viscosity of the buffer solution, ζ_{DNA} is the zeta potential of the plasmid in buffer solution, ζ_{wall} is the zeta potential of the fused silica capillary wall and E is the electric field. The sum of these two mobilities as well as the electric field strength determines the direction and the velocity of the plasmid. It has been reported that in uncoated fused silica capillaries with high ionic strength buffer, when a supercoiled plasmid is in the range of 2-16 kb, $\mu_{eo} > \mu_{ep}$ [117], so the plasmid moves in the direction of electroosmosis. The pEGFP-C2 plasmid has a sequence length of 4.7 kb, and our buffer is similar to the one reported, so we expect that electroosmotic flux is dominant inside the capillary. We did a simulation based on the measured capillary geometry to pursue the electric field distribution using a model similar to the one we described elsewhere [33]. The simulation results reveal the electric field at the tip can be as high as ~ 6000 kV/m, decaying rapidly in the solution outside the tip (Figure 2.4. The model and boundary conditions are included in the Supporting Information). Thus, near the tip we can postulate a significant net mobility pushing the pEGFP-C2 plasmid from the tip towards the cell. While it is impossible to be certain about the dynamics of the plasmid reaching the cell interior, at least we can say that it is unlikely that electrophoresis, which is in the direction away from the cell, is dominant. This is proven by the successful delivery of plasmid into the A549 cells.

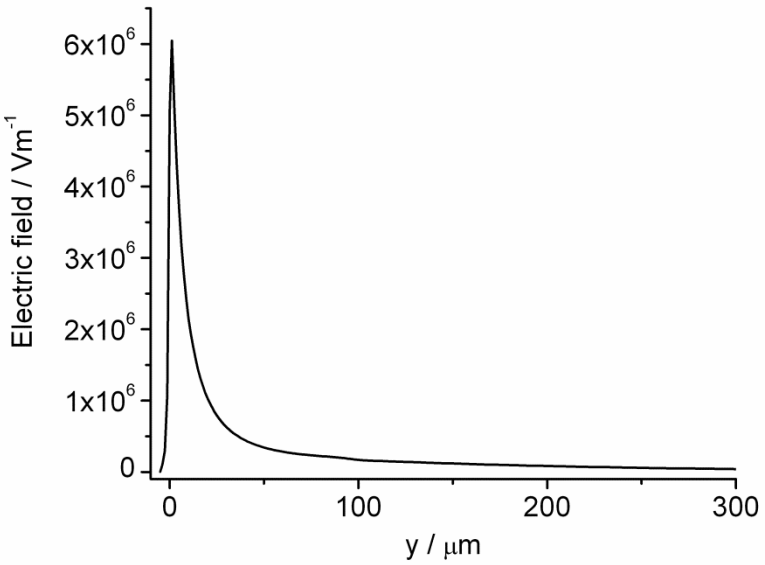

Figure 2.4 Simulated electric field distribution along the symmetry axis of the pulled capillary when a 500 V dc potential is applied. The capillary has a tip opening of 2 μm.

The x axis labeled as 'y' is the distance from the tip opening, with a negative value outside the capillary and a positive value in the capillary. A cell with a diameter of 25 μm is placed 5 μm away from the tip opening at the position of y = -5 μm. Refer to reference [33] for the model set up (the model and boundary conditions are given in Supporting Information). Temperature is set to 298.15 K.

2.4.5 Effect of pulse types on transfection

Two types of pulse protocols were applied as explained in the experimental section: the two-pulse method, and the single-pulse method. With both types, cells were transfected. Nevertheless, the two-pulse method showed higher transfection efficiency as shown in Table 2.1. In Table 2.1, there are two sets of data, one for each pulse protocol. Each row corresponds to a range of values of ΔF. In these experiments, there were three possible outcomes: the cells were transfected, they were not transfected but were present on the plate, or they were missing. At low

ΔF, transfection efficiency is poor. Transfection efficiency is much better for ΔF greater than 10%. In the single-pulse protocol, there is a considerable fraction of missing cells for ΔF greater than 10%. However, for the two-pulse protocol, the fraction of missing cells is 11%, while 89% are transfected successfully (ΔF > 10%). The better performance of the two-pulse method may be explained by the effect of pulse duration T_d and number of pulses N on electroporation. Theoretical modeling shows prolonged T_d enhances the transport through the pores but does not increase the pore density, while larger N can create more pores in the cell membrane [118]. Rols and Teissie reported that the transfer of molecules depends strongly on the time between pulses at a constant NT_d product, and longer T_d aids the transfer of macromolecules in bulk electroporation, which seems contrary to our results [112]. However, they use a much shorter pulse time (1 ms), so this advantage of prolonged T_d may disappear when applying 150 ms pulses in our experiments. Moreover, the two-pulse method has the advantage of accumulating plasmid DNA near the cell membrane after the first pulse, which facilitates the transfer of plasmid DNA during the second pulse.

Table 2.1 Effect of pulse types on SCEP-induced pEGFP-C2 transfection

Electroporated Cells ΔF	Pulse type									
	300 ms					2*150 ms with 150 ms interval				
	Total #	Missing€ #	Missing %	Transfected #	Transfected %	Total #	Missing€ #	Missing %	Transfected #	Transfected %
0-10%	5	0	0.0	0	0.0	10	1	10.0	0	0.0
10-40%	8	4	50.0	4	50.0	20	1	5.0	19	95.0
40-80%	11	7	63.6	4	36.4	8	2	25.0	6	75.0
Total	24	11	45.8	8	33.3	38	4	10.5	25	65.8

€ Missing cells 24 hours after electroporation

2.4.6 Correlation of single-cell transfection success and extent of electroporation

We noticed some cells were not transfected although they were electroporated. This is because the mechanism of DNA delivery into the cells is different from that of small molecules.

Rathenberg has visually demonstrated this point by tracking of plasmid delivery during SCEP with fluorescent labeled pDsRed-C1 plasmid and a small 54-bp fluoresceine-conjuated oligonucleotide. The small oligonucleotide entered cells immediately upon electroporation while the larger plasmid stayed at the electroporation point for at least 10 min [64]. A further study by Golzio *et al*. depicted the same view. They conducted electroporation of CHO cells with propidium iodide (PI) and rhodamine labeled fluorescent GFP plasmid. As opposed to the prompt entering of PI into the cells after the pulses, the plasmid aggregated in the electropermeabilized part of the cells before it was transferred into the cytoplasm in the following minutes post the pulses [119]. Although it is not known from direct experimental observation, a large number of theoretical papers claim that the pore size is about 1 nm in the electroporated region of the cell [8, 17, 19]. This is obviously not sufficiently large for molecules like a DNA plasmid to diffuse through freely. Several proposals have been made to explain the different behavior of DNA when electro-transferred into the cells, including the formation of endosome-like vesicles stimulated by an electric field, transient complexation between bilayer and DNA, insertion of DNA into the bilayer and involvement of electrophoretic forces [22, 120-123]. In this work, we have tried to relate the extent of electroporation (as judged by ΔF) with the transfection result as discussed below. The extent of electroporation is determined by the electroporation-induced loss of fluorescent Thioglo 1-GSH adduct and mass transfer rate of the small molecule across the transient pores.

We modified a quantitative model presented by Puc *et al*., [43] to fit the fluorescence intensity decay curves upon electroporation. This model describes the transmembrane transport of small molecules caused by electroporation. Our modifications are made based on (1) The cell volume (several pL) is much smaller than the buffer solution surrounding the cells (2 mL); (2)

the pulse duration (300 ms) is negligible when compared to the whole electroporation kinetic process; (3) The fluorescence intensity has a linear relationship with the concentration of Thioglo 1-GSH inside the cells; (4) There is photobleaching that follows a first-order decay. We get an equation from the model to fit a whole-cell fluorescence decay profile upon electroporation as follows.

$$I(t) = I_0 e^{(-kt)} e^{[K(e^{-\alpha t}-1)]} \quad (2.3)$$

$$K = \frac{M}{\alpha} \quad (2.4)$$

In equation (2.3), t is time from the start of the pulse, $I(t)$ is the fluorescence intensity at time t, I_0 is the fluorescence intensity at t = 0, k is the photobleaching rate (s^{-1}), M is the mass transfer rate (s^{-1}) through the transient pores and α is the pore resealing rate (s^{-1}). Equation (2.3) has a photobleaching term and an electroporation term. From the electroporation term we can get the fluorescence intensity, $\bar{I}$ purely induced by electroporation. When the time t approaches infinity, the steady, photobleaching corrected fluorescence is given by

$$\bar{I} = I_0 e^{-K} \quad (2.5)$$

Thus the percentage fluorescence loss induced by electroporation is

$$\Delta F = 1 - e^{-K} \quad (2.6)$$

Fitting of the decay profiles of fluorescence after electroporation using Equation (2.3) gives good correlation coefficients. Figure 2.5 shows an example of fitting. Time zero is the point right before the sudden drop of whole-cell fluorescence intensity, which we consider as the time when the pores form. From the fitting we obtain k, α and K. Then M and ΔF are calculated from equation (2.4) and equation (2.6) separately.

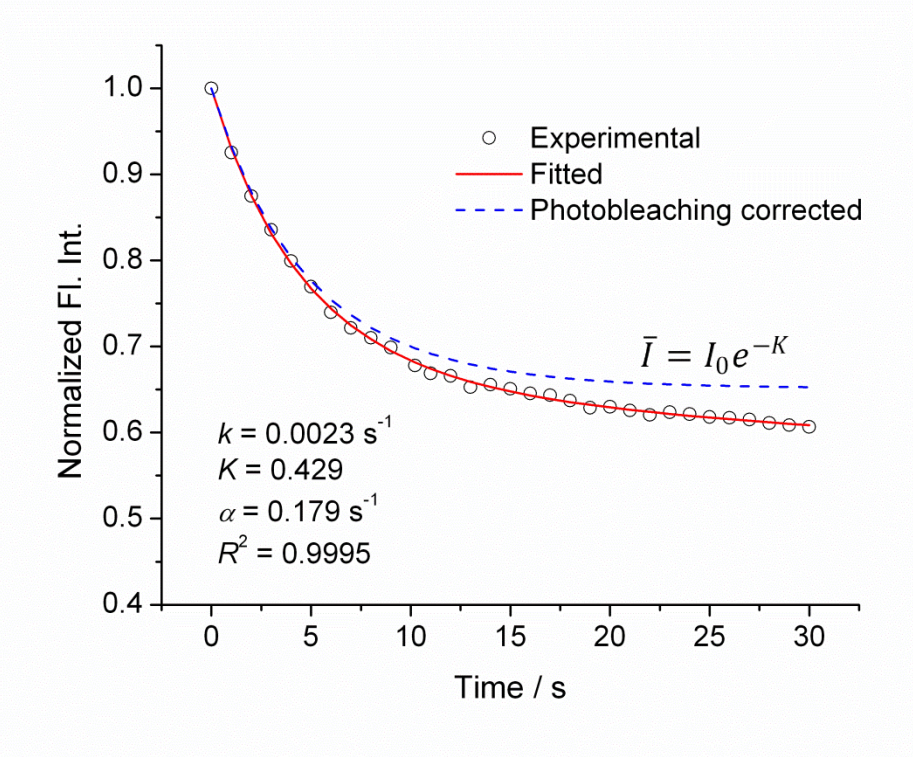

Figure 2.5 An example of fitting Eq (1) to the normalized fluorescence intensity decay curve.

Circles are experimentally observed fluorescence intensity, the red solid curve is the result from the fitting, and the blue dotted curve represents fluorescence intensity change induced purely by electroporation (i.e., photobleaching removed).

Exploring the effect of these parameters ΔF *(K)*, *M* and α on transfection gives us a clear relationship between the first two parameters and transfection. Table 2.2 shows results of a Student's *t*-test testing the null hypothesis that the parameter in question is the same in transfected and untransfected cells. We assume that the transfected cells have larger mass transfer and longer resealing constant during electroporation, so one-tailed tests are performed here. The results give extremely small P (0.0000) values for *M*, *K* and ΔF, indicating a strong relationship between these parameters and transfection, while α is apparently not related to transfection. Plotting of *M* and ΔF on the transfected and untransfected cells gives a perfect

prediction of successful transfections with M > 0.03 s-1 and ΔF >10%, as shown in Figure 2.6. We have hereby for the first time established that the occurrence of transfection with SCEP using pulled capillaries is associated with a certain extent of electroporation characterized by small molecule efflux. This also clarifies that the mechanism of DNA delivery is different from small molecule diffusion. However, we have to point out that this criterion (M > 0.03 s^{-1} and ΔF >10%) may change for different sized DNA. As Rae has shown, with increased DNA size, the voltage needed for transfection increases and the efficiency decreases [63]. Vassanelli reported a similar trend using different plasmids [53]. This is imaginable because larger DNA may need larger pore sizes for successful delivery. It would be very interesting to investigate further into how the dynamics of small molecule flux resulting from electroporation relate to the size and shape of DNA.

Table 2.2 One-tailed Student's t-test on the parameters *K, M, α* and *ΔF* for transfected cells *vs*. untransfected cells.

Parameters	Group*	Mean	SE.	[95% Conf.	Interval]	P < t
α	0	0.339	0.060	0.196	0.481	0.5525
	1	0.330	0.031	0.266	0.393	
M	0	0.017	0.003	0.010	0.024	0.0000
	1	0.129	0.018	0.093	0.167	
K	0	0.052	0.005	0.040	0.065	0.0000
	1	0.452	0.057	0.336	0.569	
ΔF	0	5.09	0.51	3.89	6.30	0.0000
	1	33.49	3.05	27.27	39.70	

*Group 0 = untransfected cells, N=8; Group 1 = transfected cells, N=33.

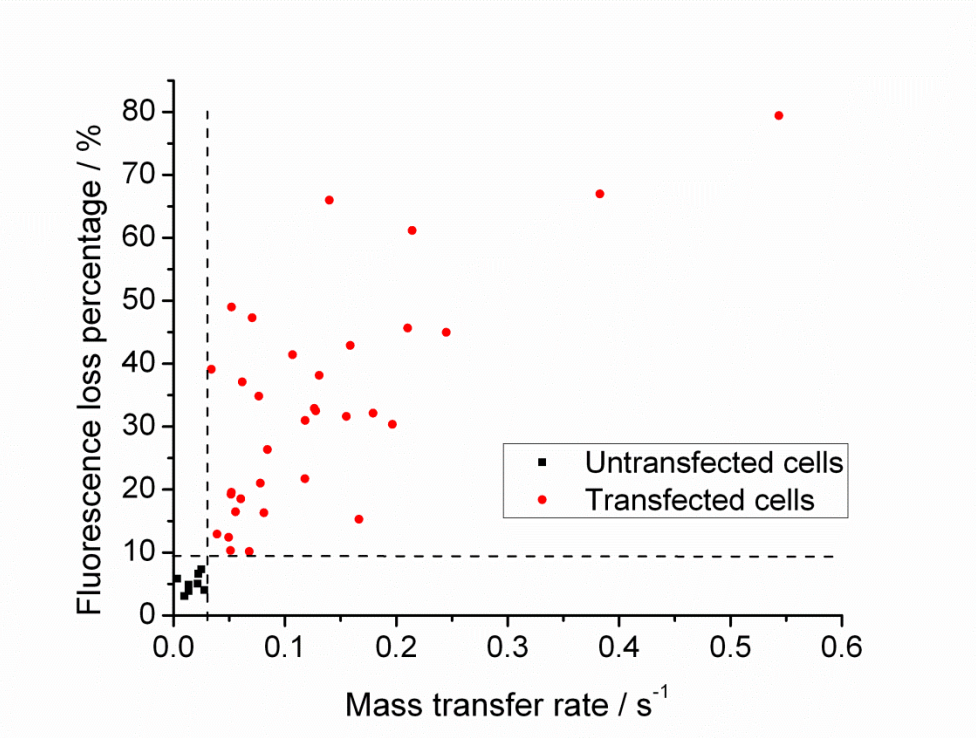

Figure 2.6 Each point represents a cell.

Black squares stand for untransfected cells and red dots represent transfected cells. Clearly, large M corresponds to a large ΔF and successful transfection. The two dashed lines define the zone for successful transfection: $M > 0.03\ s^{-1}$ and $\Delta F > 10\%$.

2.4.7 Comparison with Lipofectamine 2000-mediated bulk transfection

When we compare the SCEP-based transfection to the control experiment of bulk transfection mediated by Lipofectamine 2000, we notice an average brighter EGFP fluorescence for the bulk method than the SCEP method. The dimmer fluorescence for EGFP expression after electroporation might be due to the loss of intracellular substance and resulting lag in cell growth. It is reported that depletion of GSH in A549 cells inhibited cell growth characterized by a longer lag phase than untreated cells [124]. The same slow growth of the electroporated cells was

also observed during our experiments, as we compare the target cell in Figure 2.2 to its neighboring cells. Nonetheless, our technique has much higher transfection efficiency than the bulk method. We found that 25 – 30% of cells were transfected with Lipofectamine 2000 treatment, while at least 80% of the cells electroporated to the required extent ($M > 0.03$ s^{-1} and $\Delta F > 10\%$) are transfected using the two-pulse method. Moreover, as we stated elsewhere, we can control the extent of cell electroporation by manipulating the electric field parameters (applied voltage, pulse duration, tip-cell distance, etc) to get maximized cell survivability and electroporation efficiency[33, 113]. Therefore, we can control SCEP-introduced transfection in cells as well.

Another advantage of our approach for single-cell transfection is that a small amount of plasmid-containing solution (< 1 μl) is needed for transfection of many cells. In our experiments, we limit the number of cells electroporated with a single capillary based on the time that the cells are on the electroporation/microscope stage. Usually the cells were handled outside the incubator for no more than 2 hours to keep them healthy. Thus, the maximum number of cells electroporated for a single cell dish was limited to about 15 using one capillary within the two-hour experiments. A further automation of the operation may increase the number. Of course, smaller capillaries can also be used to conserve plasmid.

2.5 CONCLUSIONS

We have shown successful transfection of single cells with pEGFP-C2 plasmid DNA by SCEP using a pulled capillary. This is the first time that this high-resolution electroporation approach has been used for single-cell transfection. Although the mechanism of DNA transport through

the cell membrane is considered to be different from small molecules and remains unknown, our results demonstrate a strong correlation of transfection with small molecule loss. The use of the real time information provided by ΔF is useful for predicting and also guiding transfection. Further study on other plasmid vectors with different sizes may reveal if the vector size affects this relationship and how. We took advantage of the electroosmotic flow inside the fused silica capillary and the extremely high electric field at the tip part to push plasmid into the cells through the transient pores, thus avoiding the extra effort of putting pressure on the capillary. A 2×150 ms pulse train with an interval of 150 ms worked better than a single 300 ms pulse in both transfection and in preventing cells from going missing 24 hours after electroporation.

2.6 SUPPORTING INFORMATION

Supporting information including the puller program for capillary fabrication, Lipofectamine-mediated bulk transfection procedure, absorbance and emission spectra of EGFP and Thioglo 1-GSH adduct are listed here. Refer to Chapter 4 for numerical simulation of the electric field distribution around a 2-μm opening capillary during the pulses. Follow the link in the brackets (http://pubs.acs.org/doi/suppl/10.1021/ac900265f) for a video demonstrating electroporation of the transfected cell in Figure 2.2.

2.6.1 Capillary Pulling Program

Table 2.3 Program for 2-μm opening capillary pulling using a Sutter P-2000 CO_2 laser puller

Line No.	Heat	Filament	Velocity	Delay	Pull
1	250	0	30	200	0
2	250	0	30	200	0
3	250	0	30	200	0
4	270	0	30	200	0

2.6.2 Lipofectamine-mediated bulk transfection

A549 cells were cultured in antibiotic-free BME one day before transfection to reach 90% confluence at the time of transfection. Before transfection, the cells in the culture dish were washed 3 times with extracellular buffer following which 200 μL of serum-free Opti-MEM medium (Invitrogen) were added to the dish. In the meantime, 0.78 μg of plasmid and 1.5 μL of the Lipofectamine 2000 solution were each individually dissolved/diluted in 50 μL Opti-MEM. These solutions were combined and incubated at room temperature for 30 min to obtain the working plasmid/Lipofectamine solution. The working solution was added to the A549 cell dish dropwise and mixed with the medium gently by rocking the dish back and forth. After 4 hours' incubation at 37℃ in a CO_2 incubator, 1.5 mL of BME were added to each dish before continuing overnight culture. We arrived at the quantities of plasmid and Lipofectamine 2000 by exploring a range of ratios of DNA (μg) and Lipofectamine 2000 solution (μL) (2 μg DNA: 1 μL Lipofectamine to 0.75 μg DNA: 3.75 μL Lipofectamine). We found that maximum transfection yield occurred at about 1:2 (0.78 μg DNA and 1.5 μL Lipofectamine).

2.6.3 Absorbance and emission spectra of EGFP and Thioglo 1-GSH adduct

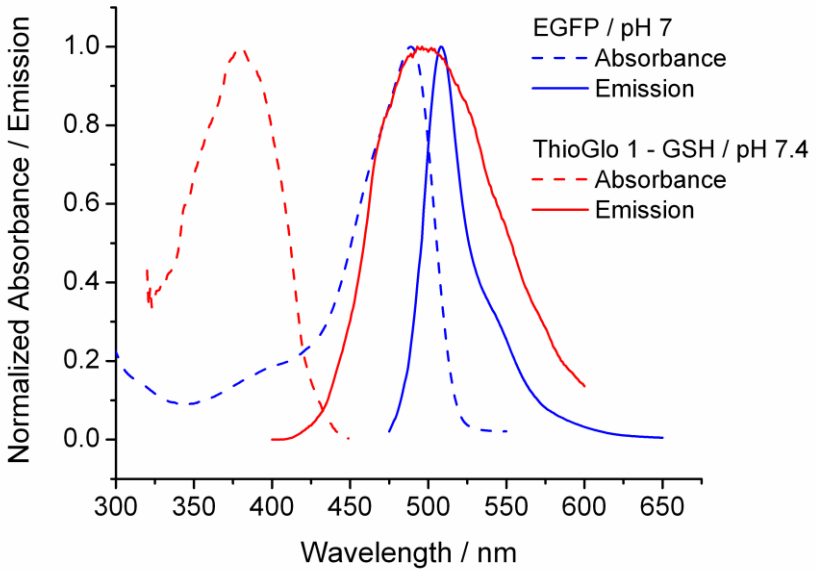

Figure 2.7 Absorbance and emission spectra of EGFP and Thioglo 1-GSH adduct.

The EGFP spectra are from Invitrogen/Molecular Probes product information.

2.7 ACKNOWLEDGEMENTS

This research has been supported by NIH Grant R01 GM066018. We sincerely thank Dr. Michael Trakselis (University of Pittsburgh, Department of Chemistry) for providing the pEGFP-C2 vector and guidance in the plasmid solution treatment and bulk transfection.

3.0 SINGLE-CELL ELECTROPORATION: TEMPERATURE AND CELL CYCLE EFFECT

3.1 INTRODUCTION

Electroporation, also called electropermeabilization, is a phenomenon that arises when cells are exposed to an electric field. In a large enough field, nanoscale pores form in the cell membrane, allowing molecules to be transported into and out of cells. These pores can close or not depending on the electrical and cell characteristics. Pores seal in reversible electroporation (RE), while irreversible electroporation (IRE) breaks down the cell membrane permanently and induces the death of cells. Electroporation is divided into two groups: bulk electroporation and single-cell electroporation (SCEP). In bulk electroporation, usually a large number of cells in suspension buffer are electroporated under a homogenous electric field using large planar electrodes, and the observations are the average from thousands of cells. In SCEP, the electric field focuses locally on a single cell, resulting in individual cell electroporation without affecting neighboring cells. Data collected from SCEP are generated from specific cells, providing unique information about cell-to-cell variation. In our study, we correlate specific cell characteristics with electroporation data, with the goal of using such correlations to control electroporation according to individual cells' characteristics. It is particularly useful to apply SCEP for single cell analysis such as drug/dye/DNA/RNA delivery or morphological or physiochemical study.

Parameters that affect electroporation have been thoroughly studied for both bulk electroporation and SCEP, but most of studies only focus on the electric pulses applied for electroporation. To achieve a reversible electroporation with high efficiency, people usually screen electric pulse types, magnitude, duration, frequency and numbers. However, other factors such as cell characteristics and/or surrounding physiochemical parameters, although are critical for SCEP, has rarely been investigated by researchers.

Temperature, although important, has only been investigated in bulk electroporation so far. It can act on pore resealing and conductivity of buffers. Most research work involving temperature effect in electroporation has been focused on temperature dependence of electrotransfection (electroporation-mediated cell transfection). Many researchers have reported an increased susceptibility to permeabilization and a shortened resealing period at temperatures greater than room temperature [125-128]. Teissie *et al*. reported that a higher level of transfection can be obtained when Chinese Hamster Ovary cells were incubated at 4℃ prior to pulse and incubated at 37℃ after bulk electroporation [119, 129]. They explained that faster resealing rate at higher temperature may increase the cell viability and consequently promote the transfection efficiency. However, to the best of our knowledge, no study on temperature effect has been reported for SCEP.

The cell cycle may lead to cell state change such as size, membrane tension and osmotic pressure. However, only a few researchers have reported a slight influence of the cell cycle on bulk electroporation with chemically synchronized cells. So far, no report on SCEP has been published. According an early report by Sachs[130] in 1974, the resting membrane potential $\Delta\psi_0$ for isolated synchronized Chinese hamster lung cells gives a peak value at S and G2 stages as a result of compartmentalization and permeability changes. A larger resting potential may induce

larger asymmetry in molecular transport through the transient pores during electroporation, especially when the applied electric field is close to the critical value for electroporation[8]. Sukhorukov *et al*. reported that chemical arresting of cells leads to excess membrane materials stored as membrane folds and microvilli, which may increases the area-specific electric conductivity and higher tolerance of hypo-osmotic stress of cells [131]. They also claimed that cell-to-cell variation in the membrane properties ($g(\lambda)$ in equation 1.1, depends on the membrane conductivity λ, and is a factor determining the critical transmembrane potential in bulk electroporation) of both G1/S phase (arrested by aphidicolin) and G2/M phase (arrested by doxorubicin) mammalian cells were similar to those of asynchronous cells. Golzio *et al*. studied the cell synchronization effect on mammalian cell permeabilization and gene delivery by electroporation[132]. They found that DNA expression was enhanced in G2/M phase synchronized cells with slightly higher electroporation efficiency, which mainly caused by the melting nuclear membrane; while synchronization in G1 phase had no effect on permeabilization and transfection. Their observation is consistent with two earlier reports that also used chemical-arrested cells for transformation[133-134]. It is necessary to point out that data on chemically synchronized cells should not be directly extrapolated to asynchronous cultures. In this paper, we examined the effect of the cell cycle on SCEP with statistical analysis by tracking the cell cycle stages of electroporated cells free from drug arrest.

We have previously studied some parameters such as cell size, cell shape and cell-probe distance which can significantly affect electric field strength on SCEP[44]. In the present paper, we investigated other critical parameters, namely, temperature and the cell cycle. It was found that at lower temperature (15℃), SCEP had smaller variability of permeabilization due to less dependence on the electroporation parameters, which can consequently lead to a better prediction

of cell pore formation. In contrast, higher temperature made it harder to predict pore formation. Also, we found that temperature can change the pore resealing rate. The viability of electroporated cells, which depends on the extent of electroporation (measured by loss of cytoplasmic fluorescent molecules), was affected by temperature as well.

As to the cell cycle, we did not observe any obvious effect of the cell stage on electroporation when all data were included in statistical analysis. When using small 2-μm tips, at a narrowed region where the mass transfer rate during electroporation is very well elucidated, a slight increase in mass transfer rate was discovered in G1/S phase cells. The cell cycle has no influence on the resealing process by statistical analysis. This indicates that the cell cycle is not a critical factor.

We have included cell viability after electroporation for statistical analysis in the present paper and our previous paper [44]. As the viability of cells also depends on cell status before electroporation, it becomes necessary to ensure that cells are healthy before applying pulses. As we mentioned in our previous papers, to assist visual observation in SCEP, we introduced a thiol-specific fluorescence probe Thioglo 1 into cells to produce cell-impermeant green fluorescence adducts by reaction with molecules containing thiol groups which include glutathione (GSH) and cysteine-containing proteins. As GSH is a key antioxidant and regulator in cells, it's important to understand how much GSH would be depleted by Thioglo 1 before starting electroporation. Our experiments demonstrate that only a small amount of GSH was depletion before electroporation.

3.2 EXPERIMENTAL SECTION

3.2.1 Materials

The chemicals used to prepare buffers were all of analytical grade and purchased from Sigma (St. Louis, MO). The HEPES-buffered saline solution, which we will call 'extracellular buffer', consisted of NaCl (140 mM), KCl (5 mM), $MgCl_2$ (1.5 mM), $CaCl_2$ (2 mM), D-glucose (10 mM) and HEPES (20 mM). The pH was adjusted to 7.4 with 0.5 M NaOH and the buffer was filtered with 0.45 μm nylon filters prior to use. Thioglo 1 was purchased from Covalent Associates (Woburn, MA). A549 human lung carcinoma cell lines were obtained from American Type Culture Association (Manassas, VA). Cell cycle kit Premo™ Fluorescence Ubiquitination Cell Cycle Indicator (FUCCI), Dulbecco's Phosphate Buffered Saline (D-PBS) without calcium or magnesium, basal medium Eagle (BME), 0.25% trypsin-EDTA, One Shot^{TM} fetal bovine serum (FBS), L-glutamine, and penicillin-streptomycin solution were all obtained from Invitrogen, GIBCO (Carlsbad, CA). Milli-Q (Millipore Synthesis A10, Billerica, MA) water was used. Pt wires (diameter 0.5 mm, high purity 99.99+ %) were purchased from Goodfellow (Oakdale, PA).

3.2.2 Cell culture and preparation

PC-3 human prostate cancer cells and A549 cells were cultured for electroporation. The culture medium was prepared by adding 50 mL of FBS, 5 mL of 200 mM L-glutamine and 5 mL of 10,000 units/mL penicillin-10,000 μg/mL streptomycin to 500 mL BME. Cells were grown in 75-cm^2 cell culture flasks (Nunc* Sterile EasYFlask) in a CO_2 incubator (HERA cell incubator, Newtown, CT) at 37℃ and 5% CO_2/95% air, and were subcultured when reaching ~ 80%

confluence every 3-4 days. Before the experiments, cells were seeded on 35-mm gridded uncoated glass-bottom cell culture dishes (MatTek Corp., Ashland, MA) at a seeding density of 2 $\times 10^4$ cells/dish. Experiments were performed on the second and third days following the cell plating.

3.2.3 Premo™ FUCCI Cell Cycle Sensor treatment for cell cycle visualization

FUCCI is a fluorescent protein-based sensor that employs a red (RFP) and a green (GFP) fluorescent protein fused to different regulators of the cell cycle: Cdt1 and geminin. Treatment of cells with FUCCI results in different fluorescence at different cell cycle phases. Red fluorescence stands for G1 phase, green fluorescence for S, G2 and M phase, and yellow fluorescence (overlap of red and green) indicates cells are at the G1/S transition phase. Cells at M/G1 transition phase have no fluorescence.

A549 cells were treated by the cell cycle kit one day before electroporation. As dictated by protocol supplied by the manufacturer, cell culture media was removed from the cells and 2 mL of Premo™ FUCCI transduction solution (D-PBS, which was comprised of 10 μL of each of the Premo™ geminin-GFP and Premo™ Cdt1-RFP reagents was added to each dish. The cell dish, covered with aluminum foil to block light, was incubated at room temperature for 2 hours with gentle shaking (80 rpm). Then the transduction solution was replaced with 1X BacMam enhancer working solution in 2 mL culture medium and the dish was incubated for 60–90 minutes in a CO_2 incubator at 37℃ and 5% CO_2/95% air. Finally the BacMam enhancer working solution was replaced by normal culture medium and the cells grew under normal growth conditions for ≥16 hours (overnight).

3.2.4 Thioglo 1 staining

A stock solution of Thioglo 1 was prepared at a concentration of 0.5 mM in pure DMSO and stored in a desiccator at -20 ℃ in the dark. A fresh 2 μM Thioglo 1 working solution was prepared by diluting 2 μL Thioglo 1 stock solution with 0.5 mL of extracellular buffer before staining the cells. For staining, each cell dish was first washed 3 times with extracellular buffer. Following the washing step, the cells were exposed to 0.5 mL of Thioglo 1 working solution and shaked for 30 s at room temperature. Then the cell dish was washed again with extracellular buffer and finally bathed in 3 mL extracellular buffer. To avoid confusion later, the foregoing procedure will be called the standard staining procedure.

To determine whether the standard staining procedure was harmful to cells, we examined the extent of GSH reacting with Thioglo 1, and cell viability after staining. Firstly, a complete 'semi-titration' profile of intracellular GSH by Thioglo 1 was made in order to determine how much Thioglo 1 and reaction time were required for complete depletion of GSH. Cells subject to "semi-titration" were cultured in the same way as those for electroporation. Cells were treated with 2 μM ThioGlo 1 solution in 0.5 ml aliquots without shaking until full reaction was reached (a maximum fluorescence intensity was reached). For each cell dish, fluorescence images of a group of cells in an arbitrarily selected scope were captured every two seconds with a 20× dry objective lens.

The "semi-titration" determines that two 0.5 ml aliquots of 2 μM Thioglo 1 is enough to fully deplete intracellular GSH in A549 cells. To determine how much GSH was reacted prior to SCEP, cells were treated with the standard staining procedure, and the fluorescence emitted by cells was imaged. Afterwards, 0.5 ml of 4 μM Thioglo 1 in extracellular HEPES buffer was added to the same cell dish for complete reaction (20 min) with GSH, and the maximum

fluorescence was recorded. The percentage of GSH reacted at 30 s was calculated as the ratio of the fluorescence intensity at 30 s and the maximum fluorescence.

To promote signal-to-noise ratio at low fluorescence intensity but avoid over-exposure when the intensity increased, the neutral density (ND) filter was set at 0.3 (50% transmission) for imaging cells with low fluorescence and changed to 0.6 (25% transmission) for imaging highly GSH-reacted cells. To make the measurement comparable at different NDs, the fluorescence intensity at ND 0.6 was multiplied by a factor determined experimentally before each experiment. To determine the value of this factor, the same batch of fluorescent cells was exposed to both ND filters, and the measured intensity at ND 0.6 was divided by that at ND 0.3. The ratio value was constant for the same day, but varied between 1.92 and 1.95 from day to day.

3.2.5 Live/Dead counting of electroporated cells

Following electroporation experiments, live/dead analysis was performed on the electroporated cells. The buffer in the cell dish was replaced by 2 mL of fresh growth medium. The cells were allowed 2 h of recovery in the CO_2 incubator at 37 ℃ and 5% CO_2/95% air, followed by a 20-minute staining with 2 mL of extracellular buffer containing 0.5 μM calcein AM and 0.5 μM propidium iodide. A measurement of cell viability was conducted on each cell that was electroporated.

3.2.6 Capillary fabrication

The fabrication of electrolyte-filled capillaries (EFC) with pulled tips was done in a laminar flow hood[45]. Fused-silica capillaries (360 μm O.D and 100 μm I.D) from Polymicro Technology

(Phoenix, AZ) were used. Capillaries were pulled at one end by using a CO_2 laser puller (Sutter Instruments Co. P-2000, Novato, CA). Prior to the pulling, a 2-cm center section of a 35-cm-long capillary was burned with a flame to remove the protective polyimide coating, and then the capillary was flushed with pre-filtered (by 0.2 μm syringe filter) Milli-Q grade water. These capillaries were pulled to create reproducible tubing with a short pulled tip having an opening inner diameter of ~2 μm or 4-5 μm. Finally, the capillaries were carefully truncated with a Shortix™ fused-silica tubing cutter to get a final length of 15 cm.

3.2.7 Microscope imaging

The cell dish was secured in a temperature control cell chamber (PDMI-2 incubator, Warner Instruments, Holliston, MA) mounted on the stage of an inverted fluorescence microscope (Olympus IX 71, Melville, NY) coupled with a cooled CCD (ORCA-ER High Resolution Digital B/W CCD Camera, B&B Microscopes Limited, Pittsburgh, PA) for fluorescence imaging. The control temperature was calibrated by measuring the real temperature in the dish at a specific ambient temperature. A Cermax® 175 W Xenon Arc lamp (PE175BF, PerkinElemer Optoelectronics, Fremont, CA) in the microscope was used as the excitation source. Cells were observed through a dry 40x 0.95 NA UPlanSApo objective lens (Olympus). Image processing was performed by the image acquisition software SimplePCI from Compix Inc (Sewickley, PA). Fluorescence intensities of regions of interest were corrected by subtracting the average fluorescence intensity of four nearby background regions.

For Thioglo 1, an Omega fluorescence filter cube (custom built, exciter XF1075-387AF28, dichroic XF2004-410DRLP, emitter XF3087-480ALP, Omega Optical, Brattleboro, VT) was used for excitation at 378 nm and emission at 480 nm. For GFP imaging, a U-MWIB2 filter set

from Olympus (Exciter 460-490, emitter 510IF, dichroic 505) was used. For RFP and live/dead imaging, a triple band "Pinkel" filter set from Semrock (Rochester, NY) was used (exciter 1: 387 nm, exciter 2: 494 nm, exciter 3: 575 nm; dichroic mirror: 394– 414 nm, 484 – 504 nm, 566 – 586 nm; emitter: 457, 530, 628 nm).

3.2.8 Experimental circuit and electronics

The experimental setup was depicted in detail in our previous paper [45]. Briefly, there were two switchable circuits: an electroporation circuit and a test circuit. The capillary was positioned using a MP-285 motorized micromanipulator from Sutter (Novato, CA). The tip end was carefully placed near the target cell at a desired distance. The other end of the capillary was inserted into a vial filled with the extracellular buffer. A platinum electrode placed in this vial was connected either to the electroporator (BTX® ECM 830, Harvard Apparatus, San Diego, CA) for electroporation, or to the function generator (SRS Model DS 340, Stanford Research Systems, Inc., Sunnyvale, CA) for the capillary test. The electrical circuit was completed with another platinum electrode in the cell dish, either connected to ground through a 100 kΩ resistor (R_m) in the electroporation circuit, or connected to a lock-in amplifier (SRS Model SR 830 DSP) in the test circuit. The voltage across the resistor created by the electroporation current was measured with a digital oscilloscope (NI 5911 Digital Oscilloscope for PCI, National Instruments Corp. Austin, Texas) for current monitoring. In the test circuit, a function generator gave a continuous 2 V AC signal at 100 Hz. The lock-in amplifier measured the magnitude and phase angle of the current at 100 Hz. The magnitude of the current reflected the resistance of the capillary tip. The lock-in amplifier measurement can help determine if the capillary was clogged or if the capillary's opening size was correct. Once the capillary was placed near a cell, the

switches were thrown to activate the electroporation circuit for electroporation. The current for electroporation was calculated by $I = \frac{V_o'}{0.091\ (M\Omega)}$ where V_o' is the reading from the Oscilloscope. For simple data analysis, we set $10 \times V_o'(\text{value}) = I_o'$, where I_o' is the "readout" current having a unit of 1.1 μA. For an example, a reading from oscilloscope of 3.3 V corresponds to a I_o' of 33, and a I of 36.3 μA.

3.2.9 Electroporation

A cell dish containing adherent cells stained with Thioglo 1 was mounted in the cell chamber on the microscope and connected to the electroporation circuit. The capillary tip was placed at an angle of 45 ^{o} with respect to the dish surface with a tip-to-cell distance (d_m) of about 3-7 μm and a distance to the dish surface of about 4 μm. The distance d_m was determined with the help of a scale bar to visually estimate the distance between the projection of the capillary tip and the edge of the cell in the horizontal imaging plane. A single, 300-ms 500 V dc pulse was applied for electroporation. Fluorescence images were captured every second during the electroporation process. The grids on the dish surface helped locate the positions of electroporated cells. After electroporation, the cell dish was allowed to rest *in situ* for 20 minutes. Afterwards, the extracellular buffer in the cell dish was replaced with 2 mL of BME and the cell dish was transferred back to the CO_2 incubator.

Electroporation with PC-3 cells (n=155) were carried out at three temperatures (15℃, 25℃ and 37℃) with capillaries of 2 μm opening tips and d_m of 2.5 μm -5 μm. A549 cells (n=361) were electroporated with capillaries of 4 μm opening tips under 15℃ and 25℃ and d_m

ranged from 3 μm to 7 μm. The temperature in the cell dish was calibrated according to the ambient temperature and the set temperature.

3.2.10 Cell Size and Shape Parameters

Cell parameters representing size and shape were obtained by the Simple PCI software. The size factors included diameter (d_c), width, height, aspect ratio and roundness. The diameter, width and height were taken into statistical analysis with a unit of micrometers. The diameter was calculated by the equation, $2 \times (A/\pi)^{0.5}$, where A was the area counted by the pixels detected in the cell image. The width was the maximum dimension of the cell in the horizontal direction (parallel to the capillary direction), and length was the dimension of the cell in the vertical direction (normal to the capillary direction). The shape factors included the aspect ratio and roundness. The aspect ratio was determined by the ratio of maximum length (longest distance between any two points on the cell boundary) and maximum breadth (maximum distance at the right angles to the maximum length), and the roundness was computed by $(4\pi A)^{0.5}/l$, where l is the perimeter of the cell.

3.2.11 Data analysis

As described in our previous paper[45], we applied a quantitative model modified from a mass transfer model reported by Puc *et al.*[43], to fit the decay curve of whole-cell thiol-Thioglo 1 fluorescence intensity upon electroporation.

$$I(t) = I_0 e^{(-kt)} e^{[K(e^{-\alpha t}-1)]} \quad (3.1)$$

$$K = \frac{M}{\alpha} \quad (3.2)$$

In equation (3.1) and (3.2), t is time from the start of the pulse, I(t) is the fluorescence intensity at time t, I_0 is the fluorescence intensity at $t = 0$, k is the photobleaching rate (s^{-1}), M is the mass transfer rate (s^{-1}) through the transient pores and α is the pore resealing rate (s^{-1}). The percentage fluorescence loss induced by electroporation at steady state and corrected for photobleaching is

$$\Delta F = 1 - e^{-K} \qquad (3.3)$$

The fluorescence decay profile after electroporation was fit to a nonlinear least squares routine in Mathcad ('genfit') using Equation (3.1). From the fitting we obtained k, α and K. M and ΔF were calculated from equation (3.2) and equation (3.3) respectively.

The values of above parameters were used to perform further statistical analysis using STATA (Intercooled 9.0) to study the influence of those variables on electroporation efficiency. The cell parameters, M, α, K and ΔF were transformed to get a normal distribution before starting the regression. Stepwise forward and backward linear regression analyses were performed for transformed M and ΔF for each temperature. In the stepwise regressions, the criterion for adding or deleting variables into/from the regression model is $p < 0.1$. The independent variables used in the linear regression were cell size, shape parameter (as described above), experimental conditions, d_m and the cell cycle (only for A549 cells, treated as a categorical variable). Anova was performed to explore the dependence of α on those independent variables. The dependence of survivability of electroporated cells on ΔF was investigated by logistic analysis.

3.3 RESULTS AND DISCUSSION

3.3.1 Determination of extent of GSH reaction with Thioglo 1 in adherent living cells

It is widely understood that by far the most abundant thiol in cells is GSH. Therefore, we will refer to the Thioglo adduct formed and its fluorescence as arising from GSH even though this is only approximately true. Figure 3.1 shows an example of a reaction of A549 intracellular GSH with 2 μM ThioGlo 1 solution added in 0.5 ml aliquots until full reaction is reached. We call this a 'semi-titration'. The fluorescence intensity from the GSH/Thioglo 1 adduct increases rapidly upon adding the first 0.5 ml of 2 μM Thioglo 1 solution, and becomes steady when reaching equilibrium. After reaction with the second 0.5 ml of 2 μM Thioglo 1 solution, the intracellular GSH is completely depleted, yielding the maximum fluorescence (No further increase in fluorescence was observed after this point). The 'semi-titration' curve is different from the free solution reaction. In solution, the GSH/Thioglo 1 reaction is complete in less than a minute with excess Thioglo 1. The reaction of Thioglo 1 with intracellular GSH is slower because of the requirement that the Thioglo 1 is transported to the intracellular space. Our semi-titration experiments show that GSH in a dish of subcultured A549 cells (approximately 10^5 cells) used for electroporation can be totally exhausted by using approximately 2-3 nmol of Thioglo 1. This is in accordance with previous studies on A549 cells that report cellular levels of GSH from 1.5 nmol /10^5 cells to 3.5 nmol/10^5 cells as a function of growth phase [124].

Table 3.1 lists the extent of reaction of thiols with Thioglo 1 using the standard pre-electroporation staining procedure in arbitrarily selected cells, and the average value for each dish. These data are from nine cell dishes from different days. . The average reaction extent in an individual dish varies from 7.7% to 14.3% in the nine dishes. Note that the reaction is faster than

that in a “semi-titration” because the cell dish is shaken after adding Thioglo 1 in the standard procedure. The standard deviation calculated from the cells in the same dish varies from 0.7% to 2.1% (the corresponding coefficient of variation varies from 0.07 to 0.19), which is relatively low, indicating cells from the same dish have similar GSH reaction extents. However, the extent of reaction of the GSH varies from dish to dish. This may be caused by inevitable differences in experimental operations such as cell seeding density. Despite the significant dish-to-dish variation, the GSH reaction extent is low with a total average at 11.3% out of nine dishes. Considering such a low reaction extent of GSH with our standard pre-electroporation staining procedure, cells are able to maintain their normal physiological status and maintain the protection from reactive oxygen species (ROS).

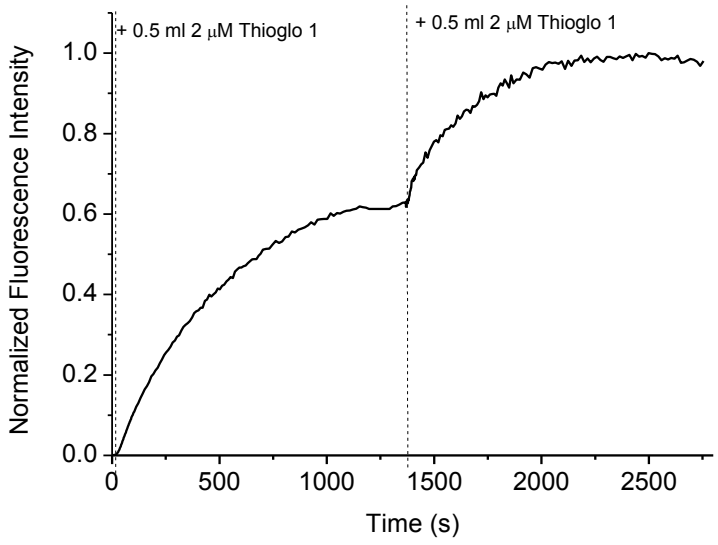

Figure 3.1 Titration of GSH in adherent A549 cells with Thioglo 1

The dotted lines indicate when the Thioglo 1 solutions were added to the cell dish.

Table 3.1 Percent of maximum Thioglo 1-induced fluorescence 30 s after adding 1 nmol of Thioglo 1

	Cell 1	Cell 2	Cell 3	Cell 4	Cell 5	Cell 6	Cell 7	Cell 8	Cell 9	Cell 10	Cell 11	Average in a dish	STDEV
Dish 1	9.9	7.4	7	7.7	7.5	6.7						7.7	1.1
Dish 2	11.4	10.8	10.1	9.8								10.5	0.7
Dish 3	13.9	13.6	13.9	14.9	14.3	11.3	11.5	13.3				13.4	1.3
Dish 4	10.2	9.8	10.9	12.1	12.5	12.5	13					11.6	1.3
Dish 5	13.2	16.5	16.6	12.2	12.8							14.3	2.1
Dish 6	10.8	8.3	12.2	11.6	11.2	12	12.1	13.1	11.7			11.4	1.3
Dish 7	12.7	11.4	10.3	12.3	11.3	10.5	9.2	9.5	11.3			10.9	1.2
Dish 8	5.9	5.1	7.8	9.7	9.9	8.8	8	8.3	7.5	7.3		7.8	1.5
Dish 9	13.6	15.5	13.6	13.7	15.1	15.2	14.3	14.1	14.5	13.8	12.9	14.2	0.8
												Average over all cells	
												11.3	

3.3.2 Electroporation of PC-3 cells under temperature control with 2 μm tips

Linear regression is a statistical technique designed to capture a linear relationship between the dependent variable and the predictor variables, and the variables are usually transformed to get a normal distribution. For the analysis of PC-3 cell electroporation data, ΔF, M and α are investigated as three dependent variables, and the independent predictor variables include d_m, d_c, roundness and aspect ratio. M and α has a unit of s^{-1}. Both d_m and d_c have a unit of micrometers. Transformation of the variables results in $ln(M)$, $ln(\alpha)$ and $ln(d_c)$, each of which has the most normal-like distribution. The linear regression based on the predictor variables for ΔF is significant at 15℃, borderline at 25 ℃, and not significant at 37 ℃. In similar fashion, $ln(M)$is significant at the two lower temperatures and not significant at the highest temperature. This temperature effect is at this point not understood. However at low temperature the cell membrane becomes less fluid. This change in fluidity may make the process of pore formation more reproducible.

Table 3.2 Overall model fit of linear regressions on *ln(M)* and Δ*F* for all PC-3 cells at different temperatures

T	Number of cells	For Δ*F* regression			For *ln(M)* regression		
		R^2	F	Prob. > F	R^2	F	Prob. > F
15 ℃	47	0.4045	16.62	0.0000	0.3755	12.43	0.0001
25 ℃	73	0.0601	2.53	0.0639	0.1333	3.61	0.0196
37 ℃	35	0.0453	1.81	0.1807	0.1526	3.70	0.0750

At 15℃, a stepwise linear regression of ΔF of PC-3 cells on the predictor variables with a significance level of 0.1 leads to two significant variables: *ln(d_c) and d_m*, with a P value of 0.007 and 0.000, respectively. Other predictor variables are not significant (p > 0.2). Table 3.3 gives the regression table with the parameters, coefficients, standard errors, p-values and more. Based on the coefficients of the significant predictor variables produced from the linear regression, we can derive an equation (3.4) to predict ΔF values based on cell diameters and cell-to-tip distances.

$$\Delta F = -0.502 * \ln(d_c) - 0.289 * d_m + 2.792 \quad (3.4)$$

Table 3.3 Linear regression of Δ*F* on predictor variables at 15℃ for PC-3 cells (R^2=0.4045)

Δ*F*	Coef.	Std. Err.	t	p>|t|	[95% Conf.	Interval]
ln(d_c)	-0.502	0.178	-2.82	0.007	-0.860	-0.143
d_m	-0.289	0.053	-5.50	0.000	-0.395	-0.183
Constant	2.792	0.613	4.55	0.000	1.555	4.028

From equation (3.4), the coefficients for $ln(d_c)$ and d_m are both negative. It indicates that larger cell diameters d_c and/or larger cell-to-tip distances d_m result in smaller ΔF. Calculating from Equation (3.4) we can get the predicted ΔF for all the tested cells. Comparison of the

predicted values to the experimental values in Figure 3.2 provides a direct view of the goodness of the above linear fit. However, the experimental ΔF is well distributed along the red line although in a wide range. This wide distribution might be caused by a lack of precise control of the experimental conditions and highly diverse properties of biological cells such as membrane surface tension (Γ in the pore formation energy change equation) [135-137], the total volume of the cells (directly related to surface tension) and cell membrane thickness (d in our numerical simulation) [138-139], and the degree of cells spreading onto the growth surface [140], etc.

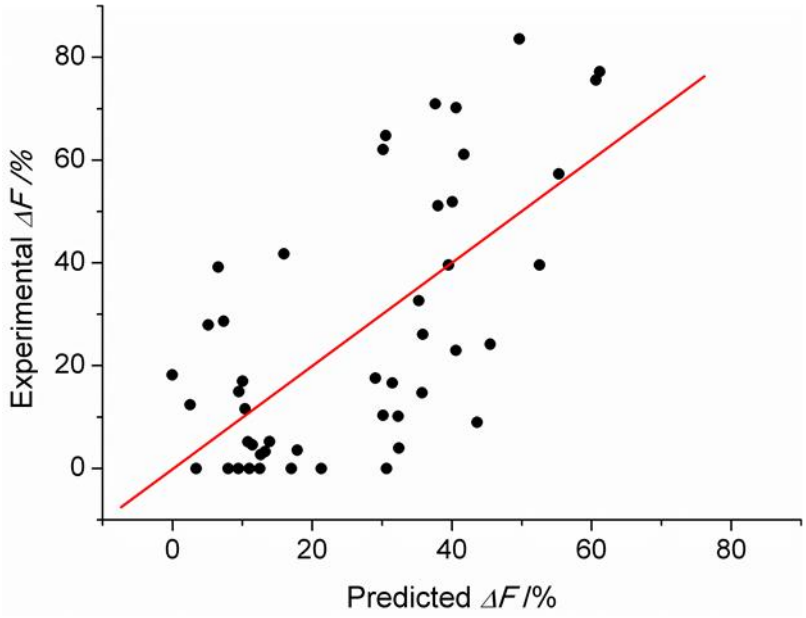

Figure 3.2 Scatter plot of experimental ΔF over predicted ΔF from stepwise linear regression analysis for PC-3 cells at 15℃.

The red line corresponds to perfect prediction.

A best linear regression for M is achieved for 15℃ when M is between 0.03 s^{-1} and 0.4 s^{-1}, corresponding to the region where $-3.5 < ln(M) < -0.9$. The regions outside this range, $ln(M) < -3.5$ or $ln(M) > -0.9$, do not produce a good regression. The regression of $ln(M)$ of PC-3 cells on the predictor variables in the $-3.5 < ln(M) < -0.9$ region generates three significant variables with

a significance level of 0.1. Table 3.4 lists the regression results. The variables include $ln(d_c)$, d_m and cell roundness, with p values of 0.007, 0.014 and 0.032, respectively. The constant has a p value of 0.008. Other predictor variables are not significant (p > 0.2). From the regression we can write equation (3.5) to predict *ln(M)* at given predictor variables.

$$ln(M) = -2.713 * \ln(d_c) - 0.565 * d_m - 3.040 * Roundness + 9.911 \qquad (3.5)$$

Table 3.4 Linear regression of $ln(M)$ on dependent variables at 15 ℃ for PC-3 cells when -3.5 < *ln(M)* <-0.9 (R^2=0.4907)

ln(M)	Coef.	Std. Err.	t	p>|t|	[95% Conf.	Interval]
$ln(d_c)$	-2.713	0.871	-3.11	0.007	-4.559	-0.866
d_m	-0.565	0.205	-2.76	0.014	-1.000	-0.130
Roundness	-3.040	1.295	-2.35	0.032	-5.784	-0.295
Constant	9.911	3.256	3.04	0.008	3.009	16.813

Similar to those of ΔF, the coefficients for $ln(d_c)$, d_m and Roundness in equation (3.5) are all negative. This means that larger cell diameters, higher cell roundness, and/or longer cell-to-tip distances can lead to smaller *M*, thus less permeabilization. Figure 3.3 shows a plot of the predicted *ln(M)* from equation (3.5) over the experimental *ln(M)* for all PC-3 cells electroporated at 15℃. The red line indicates the place where the predicted values are equal to the experimental values. The region of -3.5 < *ln(M)* <-0.9 is labeled as the grey block, which provides a good equal distribution of the experimental values along the red line. Enlarging the regression to the whole data results in a worse R^2 =0.3755 and the missing of Roundness in the coefficient table. No good regression was found at the region of *ln(M)*<-3.5 or *ln(M)*>-0.9. We speculate that when *M* is very small, the quantitative determination is difficult because the change in

fluorescence is rather small. As a result, the correction for photobleaching becomes critical. In the middle region where sensitivity is not a concern, pores can form with a gradually increasing area and permeability under increasing external stress, demonstrating a good relationship between *M* and the predictor variables. In the case of very large *M*, the explanation could be that large pores form under the high external electric field, causing the irreversible destruction of cell membrane. Under such circumstances the dependence of mass transfer rate upon predictor variables may lose its linearity.

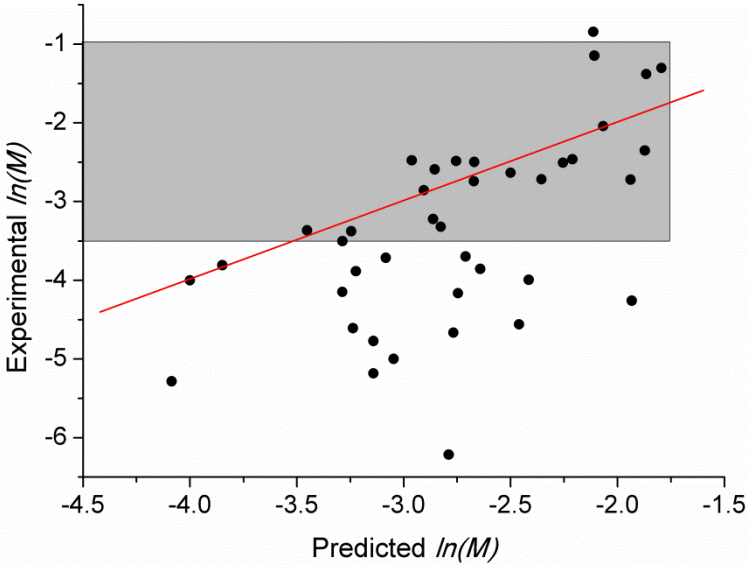

Figure 3.3 Scatter plot of predicted *ln(M)* from regression analysis over experimental *ln(M)* for PC-3 cells at 15 ℃ when regression is performed based on the region of -3.5 < *ln(M)* <-0.9.

The red line corresponds to where predicted values are equal to the experimental values.

From our experiments we see a strong relationship between $\Delta F\%$ and post-electroporation cell survivability. Statistical analysis reveals that they are logistically related. In Figure 3.4, the spots are indicative of the viability of electroporated cells. The spots located at viability 1 represent living cells, while those at viability 0 represent dead cells. The line is the

fitted likelihood of cell survivability calculated from logistic analysis. Figure 3.4 shows the chance of cell survival decreases as ΔF increases. Cells with a ΔF of 10% have a chance of 90% to survive, and this survival chance decreases to 75% when ΔF increases to 20%, and to 25% with a ΔF of 40%. When ΔF increases to 50%, cells have only 10% chance to keep alive after electroporation. When considering the temperature effect on this relationship, we do not find a significant influence from logistic analysis. However, the boxplot of normal distributed $ln(\Delta F)$ at different temperatures in Figure 3.5 shows that higher temperature is likely to yield a lower average of ΔF for both survived and dead cells. It manifests that cells are easier to lose viability at higher temperature than lower temperature with similar ΔFs.

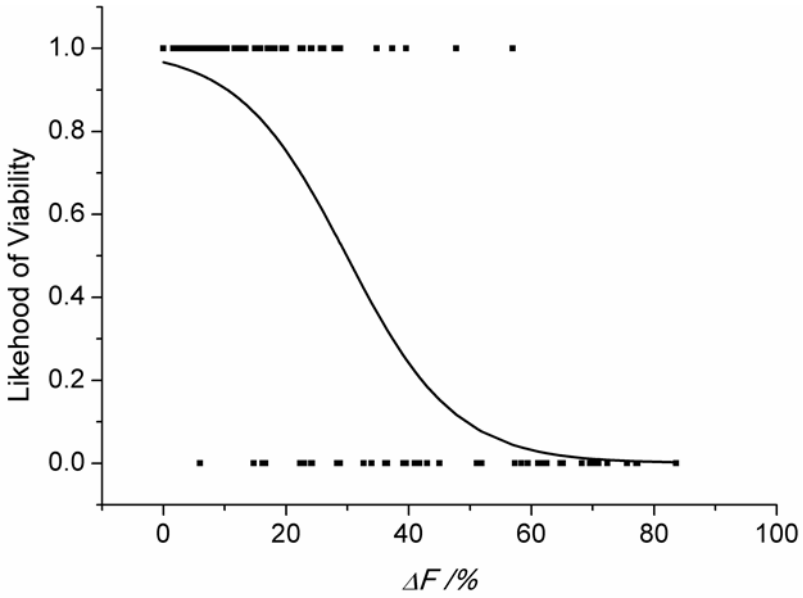

Figure 3.4 Likelihood of electroporated PC-3 cells viability over ΔF by logistic regression (Pseudo R^2=0.5011, n=155).

Logistic analysis shows no significant temperature effect. Regression is done on cells with a $\Delta F > 0$.

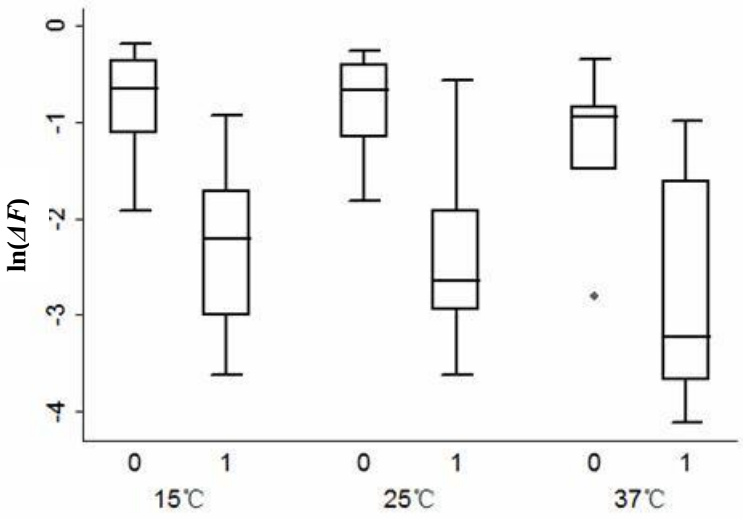

Figure 3.5 Distribution of *ln(ΔF)* for alive PC-3 cells (groups labeled as "1") and dead PC-3 cells (groups labeled as "0") at different temperatures.

The upper and bottom of the box stand for $25^{th}/75^{th}$ percentiles, and the bar inside the box stands for the median. The ends of the whiskers represent the maximum and the minimum adjacent values. Dots are outliers.

3.3.3 Electroporation of A549 cells with temperature control and cell cycle tracking by 4-5 μm tips

Electroporation with larger 4-5 μm opening tips was carried out on A549 cells. As we had a considerable tip size and shape variation for 4-5 μm tips than 2 μm tips, we got slightly different currents using different 4-5 μm tips with the same applied voltage, temperature and buffer solution. In this experiment, besides the control of temperature and d_c, we added the measured current along with the recorded cell cycle as predictor variables for the analysis. Note the current variable *I'* in the regression has a unit of 1.1 μA, *M* and α has a unit of s^{-1}, and both d_m and d_c have a unit of micrometers.

Similar to the previous PC-3 electroporation data using 2 μm tips, we only get good regression of *ΔF* and *ln(M)* for 15℃ (Table 3.5). The analysis results in poor prediction for 25℃.

Preliminary experiments with higher temperature (37℃) show a high cell viability loss after electroporation and large variation. Our full experiments on A549 cells proceeded with two temperatures (15℃ and 25℃), which is enough to tell the story of temperature effect while giving more effort on the cell cycle.

Table 3.5 Overall model fit of linear regressions on *ln(M)* and Δ*F* for A549 cells at different temperatures

T	Number of cells	For Δ*F* regression			For *ln(M)* regression		
		R^2	F	Prob. > F	R^2	F	Prob. > F
15 ℃	166	0.4382	43.90	0.0000	0.2355	8.39	0.0000
25 ℃	195	0.1756	9.26	0.0000	0.0711	4.60	0.0042

When the temperature is 15℃ the stepwise linear regression with a significance level of 0.1 gives good prediction for both Δ*F* and *M*. A best regression for *M* is achieved when *M* is between 0.03 s^{-1} and 0.5 s^{-1}, corresponding to the region where -3.5 < *ln(M)* <-0.7. Enlarging the regression to the whole data results in a worse R^2 =0.2355. No good regression for *M* was found at the region of *ln(M)*<-3.5 or *ln(M)*>-0.7. As explained previously with PC-3 cell data, we may ascribe the failure of *ln(M)* regression attempt beyond a limited region to a sensitivity issue with small *M* and formation of irreversible pores not obeying the linear relationship with large *M*. From the regression we can write equations to predict ΔF (regression based on the whole data of 15℃) and *M* (regression based on the data with *M* between 0.03 s^{-1} and 0.5 s^{-1} at 15℃). Table 3.6 and 3.7 are the regression result tables listing the parameters, their coefficients, standard error and p-values.

$$\Delta F = 0.043 * I_o' - 0.288 * \ln(d_c) - 0.150 * d_m + 0.469 \quad (3.6)$$

$$Ln(M) = 0.252 * I_o' - 0.352 * d_m - \begin{cases} 9.203 & \text{S, G2, M and M/G1 phase} \\ 9.822 & \text{G1 phase} \\ 8.466 & \text{G1/S phase} \end{cases} \quad (3.7)$$

Table 3.6 Linear regression of ΔF on dependent variables at 15 ℃ for A549 cells (R^2=0.4382, n=166)

ΔF	Coef.	Std. Err.	t	p>|t|	[95% Conf.	Interval]
I_o'	0.043	0.013	3.20	0.002	0.016	0.069
$ln(d_c)$	-0.288	0.086	-3.33	0.001	-0.458	-0.117
d_m	-0.150	0.014	-10.61	0.000	-0.178	-0.122

Table 3.7 Linear regression of $ln(M)$ on dependent variables at 15 ℃ for A549 cells when $-3.5 < ln(M) < -0.7$ (R^2=0.3507, n=77)

ln(M)	Coef.	Std. Err.	t	p>|t|	[95% Conf.	Interval]
I_o'	0.252	0.067	3.76	0.000	0.119	0.386
d_m	-0.352	0.077	-4.55	0.000	-0.506	-0.198
G1 phase	-0.619	0.190	-3.27	0.002	-0.997	-0.241
G1/S phase	0.737	0.173	4.25	0.000	0.391	1.082
Constant	-9.203	2.184	-4.21	0.000	-13.556	-4.851

From equation (3.6) and (3.7), we can calculate the predicted ΔF and M. Figure 3.6 and 3.7 show us how the experimental values distribute around the predicted values.

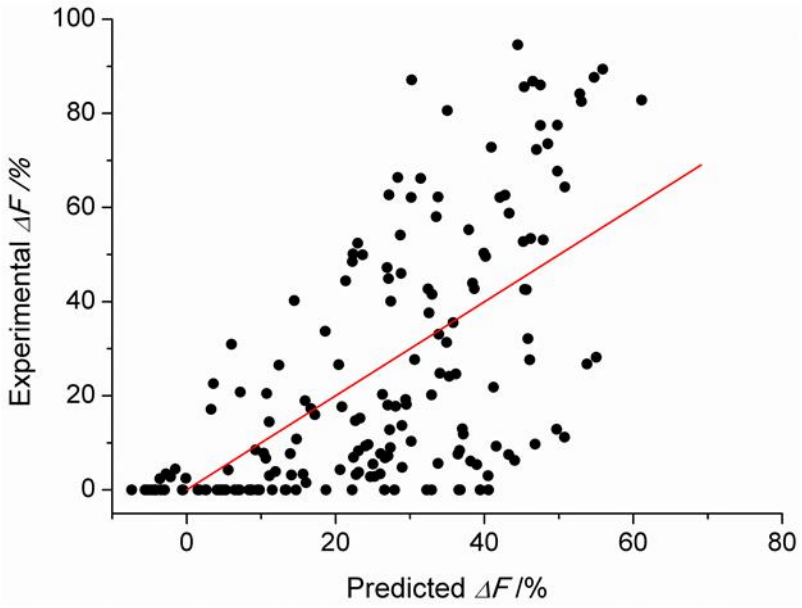

Figure 3.6 Scatter plot of predicted *ΔF* from regression analysis over experimental *ΔF* for A549 cells at 15 ℃.

The red line corresponds to where predicted values are equal to the experimental values.

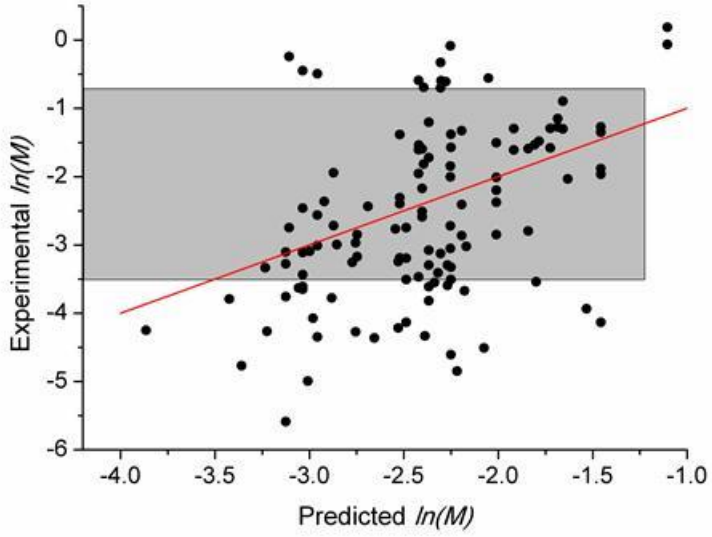

Figure 3.7 Scatter plot of experimental *ln(M)* over predicted *ln(M)* from regression analysis for A549 cells at 15 ℃ when regression is performed based on the region of -3.5 < *ln(M)* <-0.7.

The red line corresponds to where predicted values are equal to the experimental values. The region of -3.5 < *ln(M)* <-0.7 is labeled as the grey block.

As shown above, current I_o' is a significant factor for both ΔF (p = 0.002) and M (p = 0.000). An increase of current increases leads to an enhanced permeability of cell membrane. Again, larger tip-to-cell distance d_m and/or larger cell diameter d_c result in less cell membrane permeabilization. The cell cycle has no obvious influence when taken account into the whole data regression. However, if we look at the electroporated cells where M is between 0.03 s^{-1} and 0.5 s^{-1} ($-3.5 < ln(M) < -0.7$), the story changes. The cell cycle does affect slightly in this narrowed region. Compared to cell cycle phases $S, G2, M$ and $M/G1$ which show no significant distinguish, G1 phase decreases M, while G1/S phase increases M. The reason for this change is unknown. Unlike the above 2 μm tip PC-3 data, we do not see a factor of cell size and shape (diameter and roundness) for M here when using this narrowed M region, probably because the larger tip sizes are more comparable to the cell surface area where the tips are facing to than the small tips.

The viability of A549 cells also depends on ΔF, and this dependence involves a slight effect of temperatures (p = 0.021 for temperature) as shown in Figure 3.8. The probability of cell death at 25 ℃ is larger than that at 15 ℃ given the same ΔF. When compared to the above PC-3 cells data, with the same ΔF, A549 cells electroporated using 4-5 μm tips have a higher probability of cell death. As expected, we see a decreased chance of cell survival with an increased ΔF. A cell with a ΔF of 10% has a chance of 86% to keep alive at 15℃, and a chance of 73% at 25℃. This survival chance decreases to 61% when ΔF increases to 20% at 15℃ (to 42% at 25℃). When ΔF increases to 40%, cells have only 10% chances to keep alive after electroporation at 15℃, or a worse 4% chances at 25℃. A boxplot of normal distributed $ln(\Delta F)$ at different temperatures in Figure 3.9 also shows that at high temperature both survived cells and dead cells have a lower average of ΔF. Again, it tells us that at higher temperature cells have to loss less intracellular contents to sustain their viability than at lower temperatures. We would propose that cells should

be pulsed at low temperature like 15℃ to obtain best control on electroporation, then immediately transfer to incubation at 37℃ for better resealing.

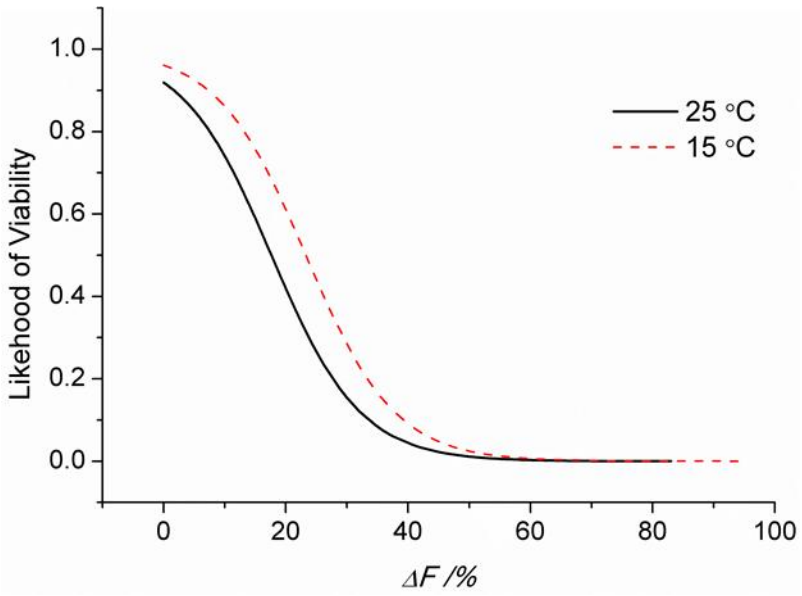

Figure 3.8 Likelihood of electroporated A549 cells viability over ΔF by logistic regression (Pseudo R^2=0.5061, n=387). Regression was done on cells with a $\Delta F > 0$.

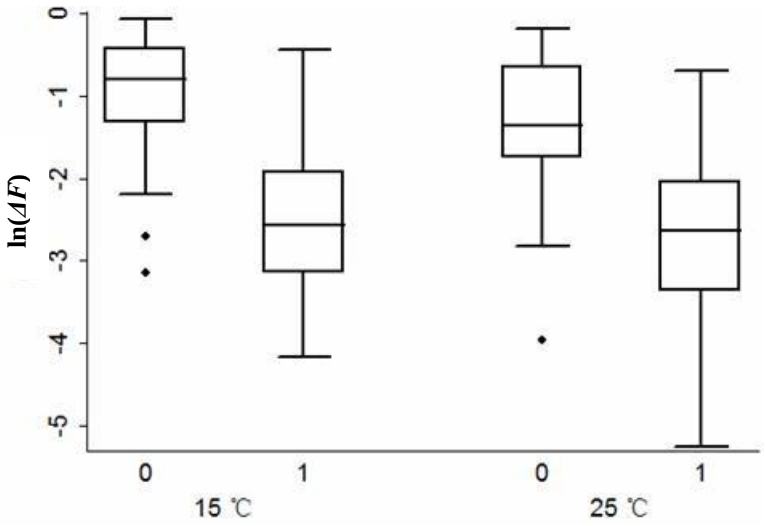

Figure 3.9 Distribution of $ln(\Delta F)$ for alive A549 cells (groups labeled as "1") and dead A549 cells (groups labeled as "0") at different temperatures.

High temperature gives a lower average of ΔF for both survived cells and dead cells. The boxplot boundaries have the same meanings as in Figure 3.5.

3.3.4 Dependence of electroporation on distance for all temperatures

Although we fail to get a good linear regression for high temperatures of 25℃ and above, we notice the distance d_m is a vital variable affecting the efficiency of electroporation. We have electroporated several hundred A549 cells at 15℃ and 25℃, and Figure 3.10 demonstrates the probability of electroporated cells at each d_m for both temperatures. From statistical analysis, one-tailed tests of d_m on ΔF and M always show a p-value smaller than 0.001 for at all temperatures, which means distance is a powerful parameter affecting electroporation outcomes. For both temperatures the chance of electroporation decreases when d_m increases. The lower temperature seems have more clear trend at d_m = 4-6 μm.

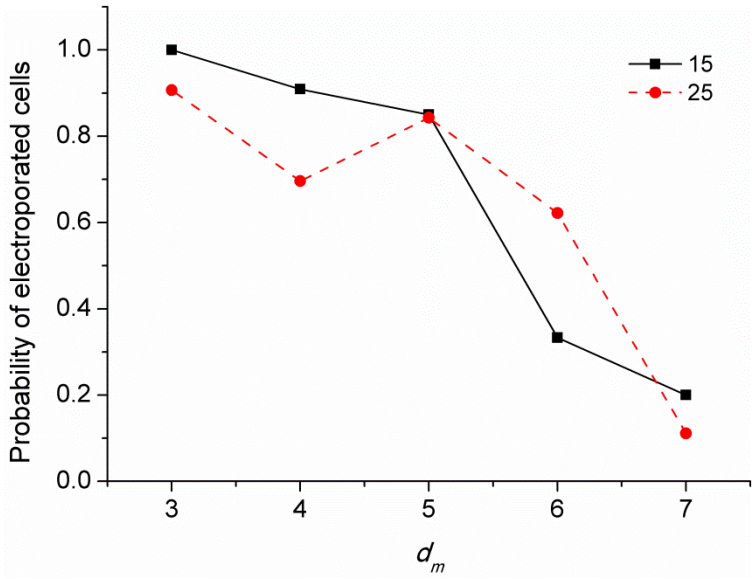

Figure 3.10 Probability of electroporated A549 cells over d_m.

3.3.5 Dependence of resealing rate α on T

Despite that fact that the resealing process is important for the application of electroporation, the understanding of this process is relatively poor [6]. Saulis suggested that pore resealing is a random process which varies from cell to cell although the kinetics of this process can be very well describe by theoretical curves [141]. This random phenomenon is understandable considering that the pore resealing energy depends on individual cells and is a complicated process. In our experiments, no significant effect of other experimental conditions or cell factor on resealing rate is observed except for a temperature effect. From anova analysis, temperature affects resealing rate for both PC-3 cells and A549 cells. Resealing rate α was transformed to $ln(\alpha)$ to get a normal distribution for the analysis. Anova of $ln(\alpha)$ on temperature results in $p = 0.0012$ for PC-3 cells and $p = 0.0079$ for A549 cells. No significant influence of the cell cycle on resealing rate was found. Figure 3.11 and 3.12 are boxplots of $ln(\alpha)$ at all temperatures for both cell lines. Higher temperature gives a higher average of $ln(\alpha)$ and larger variance than lower temperatures. To be specific, for PC-3 cells the average α is 0.157 s^{-1} at 15℃, 0.200 s^{-1} at 25℃ and 0.453 s^{-1} at 37℃, respectively. For A549 cells the average α is 0.304 s^{-1} at 15 ℃ and 0.446 s^{-1} at 25℃. The results mean cell membrane reseals faster at elevated temperature, which makes sense when considering that the pore recovery energy is formulated with a factor of exp(-1/T). To be noticed in the presented work the resealing rate is the rate at which the plasma membrane restores its function as a barrier to the mass transport of the fluorescent GSH- Thioglo 1 adduct out of the cell. The resealing time obtained in this work is close to those obtained in bulk electroporation using small molecules as probes (~ several minutes). Full recovery of the cell membrane may need a longer time (tens of minutes to several hours) [142].

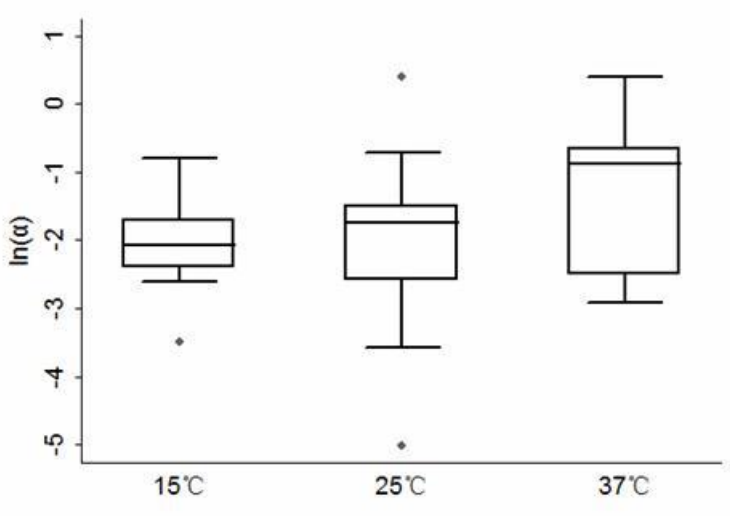

Figure 3.11 Distribution of *ln(α)* at different temperatures for PC-3 cells.

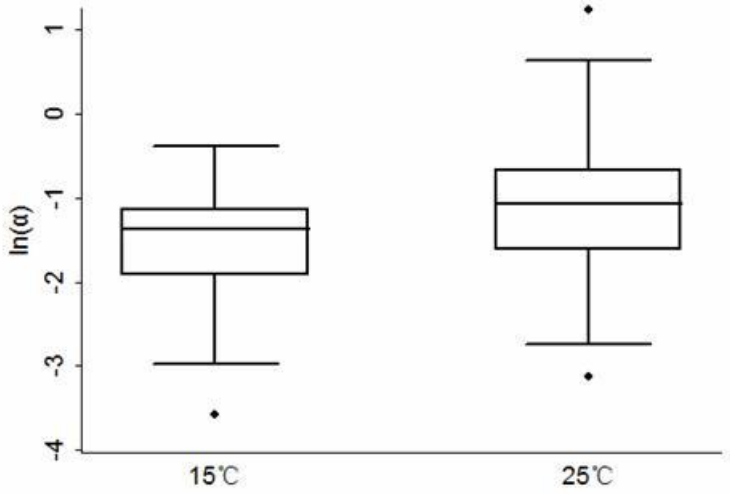

Figure 3.12 Distribution of *ln(α)* at different temperatures for A549 cells.

3.3.6 Understanding the dependence of mass transfer rate on tip-to-cell distance from a mathematical perspective

The linear regression shows that d_m is a very important factor affecting *M*. Given that all other predictor variables are kept the same, a linear relationship between *ln(M)* and d_m exists based on

experimental data. It is interesting to interpret origin of this relationship in a theoretical way. Mass transfer rate is related to the permeability of the porated portion of the membrane as well as the area of the membrane that is porous. From the 3D modeling introduced in the following chapter we can get transmembrane potential and fraction of electroporated area at defined d_m and d_c. Assume that the electroporated membrane permeability is directly determined by the maximum transmembrane potential (TMP_{max}), we can write the

$$M = C_1 \times TMP_{max} \times FEA \times A_c \qquad (3.8)$$

Where *FEA* is the fraction of electroporated area, A_c is the total area and C_1 is a constant. At a defined cell diameter, A_c is a constant. Then the above equation can be written as

$$\ln(M) = \ln(TMP_{max} \times FEA) + \ln(C_1 \times A_c) \qquad (3.9)$$

where the last item is a constant.

Interestingly the computed data from the 3D simulation models give a good linear relationship between $\ln(\mathrm{TMP_{max}} \times \mathrm{FEA})$ and d_m at defined cell sizes within a range of d_m (1-7 μm). For a tip opening of 2 μm, the slopes are -0.506, -0.498, -0.464 for cells having a diameter of 20 μm, 25 μm and 40 μm, respectively. When the tip opening increases to 4 μm, the corresponding slopes are -0.385, -0.383, -0.428. These values are very close to the coefficient achieved from the linear regression (a coefficient of -0.565 for 2-μm tips and -0.352 for 4~5-μm tips). In other words, our experiments confirmed a linear relationship between the mass transfer rate and product of $\mathrm{TMP_{max}}$ and electroporated area. This can be very useful as we can compute the $\mathrm{TMP_{max}}$ and electroporation area, we can predict the average electroporation outcomes at various experimental conditions including those not investigated in this work, such as tip sizes and shapes.

3.4 CONCLUSIONS

We have studied electroporation on PC-3 cells and A549 cells with two different sized capillaries under temperature control. The electroporation extent was observed by fluorescence produced from GSH reaction with Thioglo 1 reagent. The cell staining procedure is believed to be safe, with a low average of 11% of GSH reacted. Linear regression involving the experimental variables and cell parameters has been carried out to predict the electropermeablization of cells, and good regression of ΔF and M on predictor variables were obtained at 15℃. Tip-to-cell distances and cell diameters, as well as the electric current, are main factors affecting ΔF. For M, a narrowed region between 0.03 s^{-1} and 0.4 s^{-1} (for PC-3 cells with 2 μm tips, or between 0.03 $s^{-}1$ and 0.5 s^{-1} for A549 cells with 4-5 μm tips) gives best regression. Cell diameters and cell roundness has a significant influence on M when using the 2 μm opening tips on PC-3 cells, and this impact disappears when using the 4-5 μm opening tips on A549 cells. The cell cycle shows no effect on ΔF but slightly affects the mass transfer rate. Of all the examined parameters only temperature shows a strong influence on pore resealing. Cells reseal faster at higher temperature. Cell survivability is logistically related to ΔF. Furthermore, lower temperature has the advantage to sustain the cell viability with the same ΔF.

In our previous paper, we studied SCEP of A549 cells with no temperature control, no electric current measurement and no cell cycle tracking with subsequent statistical analysis [44]. Similarly in that paper, we have also found the resealing rate α is a random value for individual cell and is not affected by experimental conditions but temperature. Furthermore, in both reports tip-to-cell distance is acting as a vital factor determining ΔF in SCEP. The difference between the predict equations obtained in these two papers might be caused from the difference in

temperatures, cell population distribution and the commercial cell line batch. This work reveals temperature, electric current, capillary tip size as well as tip-to-cell distance are important predictors during SCEP.

4.0 NUMERICAL MODELING OF ELECTRICAL POTENTIAL DISTRIBUTION AND MASS TRANSPORT DURING ELECTRICAL PULSES

We have mentioned in our first chapter that when a voltage is applied through micrometer-sized probes such as the capillaries having microtips, no analytical solution is available to explicit the resulted electric fields. Numerical modeling has therefore become a very useful tool to study the localized electric field. Because the average transmembrane potential for electroporation is known from bulk electroporation experiments, the numerical modeling gives potential drop across the cell membrane and accordingly we can predict if electroporation occurs under the given conditions. Further modeling combining mass transport modules provides information about the flowing direction of a particular molecule, and helps us to guide the sampling/delivery process under the applied voltage.

4.1 2D NUMERICAL SIMULATION OF ELECTRIC FIELD DISTRIBUTION AROUND A MICRO-OPENING CAPILLARY

As mentioned before, the inhomogeneous electric field makes analytical calculation difficult. Previously Dr. Weber gave an analytical formula for electric field distribution at the symmetric axis produced by a uniform i.d. capillary. However, we are using a pulled capillary with a tip opening of 2 μm or 4 μm for electroporation of cells that have sizes on the order of 20-40

micrometers; hence the situation of electric field distribution around the cells is highly heterogeneous and much more complicated. We have developed a numerical simulation model for SCEP in Comsol Multiphysics 3.3, and used the model to resolve the electric field distribution and anticipate the Transmembrane Potential (TMP) and the Fraction of Electroporated Area (FEA).

4.1.1 Capillary drawing in Comsol

A typical capillary with a 2 μm tip opening and a taper length of 2 mm was chosen for the model. Because the length of the capillary (15 cm) was much larger than the tip opening, we only modeled part of the capillary, including the tapered 2 mm and 0.5 mm of untapered capillary. The real dimensions (outer diameter /inner diameter ~ distance from the tip end) were measured after taking images under objectives 20×, 40×, and 60×. These data were imported into OriginLab and fitted into 3 Sigmoidal Boltzman functions (0-100 μm/100-600 μm/600-1600 μm) followed by smoothing. Finally, the outer and inner walls were each defined by 62 points (radius and axial distance).

4.1.2 Model and parameters

The simulation of SCEP utilized a conductive Media DC with 2D axial symmetry. This model solved a partial differential equation: $-\nabla(\sigma \nabla V) = Q$, where σ is the conductivity, V is the electrical potential, and Q is the current source (gradient of current density). Figure 4.1 shows the modeling geometry and boundary conditions. Parameters and constants used are listed in Table 4.1. Two domains, the inside of the cell (d_{cins}) and its extracellular surroundings (d_{cout}), are

modeled independently. They are related by membrane boundary condition set to be $J_n\ (d_{cout}) = (V_i\text{-}V_o)*\sigma_m/\Delta$ and $J_n\ (d_{cins}) = (V_o\text{-}V_i)*\sigma_m/\Delta$ where Vs are defined on the inside surface of the membrane, V_i, and the outside surface, V_o, σ_m is the membrane conductivity, Δ is the membrane thickness, and J_n is the current density normal to the membrane. The voltage at the simulated capillary untapered end is related to the applied voltage with an equation, $V_0 = V_{app} + E_{y\_dcout} \times (L_{tot} - L_{sim})$ where E_{y_dcout} is the y component of the electric field (in the symmetry axis direction) in the outside cell domain. Accurate calculation of V_0 requires turning on the "weak boundary condition". The cell diameter, cell-to-tip distance and the temperature T varies for the simulation.

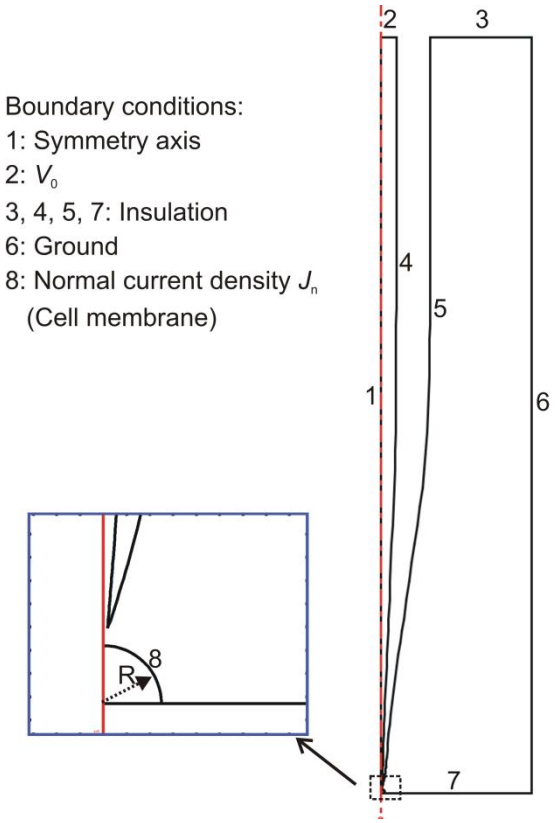

Figure 4.1 Modeling 2D axial symmetry geometry for electroporation.

The actual shape of the capillary tip is used. Boundary conditions are described in the figure. The capillary is positioned perpendicular to the dish surface and is centered above the cell. Rotational symmetry is used to simplify the simulation.

Table 4.1 Parameters and constants for 2D axial-symmetry numerical simulation of potential distribution around a 2-μm capillary tip

Total capillary length L_{tot}	0.15 (m)
Simulated capillary length L_{sim}	0.0025 (m)
Applied voltage V_{app}	500 (V)
Conductivity of extracellular buffer σ_s*	$C_A + C_B(T - 273.15) + Cc(T - 273.15)^2 \left(\frac{S}{m}\right)$
Conductivity of cytoplasm σ_c	$\frac{13}{60} \times \sigma_s$(S/m)
Conductivity of cell membrane σ_m	5.3×10^{-5}(S/m)
Cell membrane thickness Δ	7×10^{-9} (m)
Tip-Cell distance d	3-8 (μm)
Cell radius R	12.5 μm

* *C_A=1.11669, C_B=0.01838 and Cc = 1.65 × 10 -4.*

4.1.3 Resistance for EFC with different tip size

The electric field distribution of buffer-filled capillaries with tip i.d. of 2 μm and 3.6 μm were simulated by simply setting the top end with a potential source of 500V and the tip end as grounding. The resistance of EFC was then calculated by

$$R = \frac{U}{I} = \frac{U}{\int J} = \frac{500\,(V)}{\int J_Z\_dc\,(A)} \qquad (4.1)$$

where U is the applied voltage, I is the current going through the capillary, which is calculated by integrating J over area, J is the current density in the capillary, and J_Z_dc is the current density at the inlet end of EFC normal to the circular surface.

Table 4.2 gives the simulated resistances of these two different tip-sized EFCs at different temperature. Apparently the resistance decreases along with the increase of temperature because of the enlarged conductivity. The resistance of a 2-μm tip EFC is slightly larger than a 3.6-μm one. At room temperature, they give resistance of 14.5 MΩ and 13.7 MΩ respectively. From the resistance of the EFCs we have calculated the theoretical readings given by the lock-in amplifier

in the test circuit which is shown in Figure 2.1, without taking into account of the resistances from other components in the circuit. The experimental readings are very close to the calculated values (typically 0.127 μA – 0.132 μA for 2-μm tips and 0.135 μA - 0.140 μA for 4-μm tips, with an ambient temperature between 20 ℃ to 25 ℃), and this means the model is valid for the simulation of potential distribution.

Table 4.2 Simulated resistances of different tip-sized EFCs at different temperature

T	2 μm tip capillary		3.6 μm tip capillary		Difference	
(℃)	Resistance (MΩ)	Reading * (μA)	Resistance (MΩ)	Reading (μA)	Resistance (MΩ)	Reading (μA)
0	21.87303	0.09144	20.61623	0.09701	1.2568	0.00557
15	17.08537	0.11706	16.10472	0.12419	0.98065	0.00713
20	15.75421	0.12695	14.85008	0.13468	0.90413	0.00773
25	14.5434	0.13752	13.70913	0.14589	0.83427	0.00837
30	13.44442	0.14876	12.67316	0.15781	0.77126	0.00905
37	12.07474	0.16563	11.38215	0.17571	0.69259	0.01008

** Reading: Calculated reading from lock-in amplifier given the function generator produces 2 V_{rms} without considering the other sources of resistance.*

4.1.4 Resistance with cells at various tip-cell distances

Using the model described in 4.1.2, the resistances of EFCs and the whole electroporation system were calculated by the voltage drop and integrated current

$$R(EFC) = \frac{\Delta U}{\int J(Inlet\ end)} = \frac{500 - U(tip\ center)\ (V)}{\int J_Z\_dc(Inlet\ end)\ (A)} \quad (4.2)$$

$$\text{System resistance} = \frac{500\ (V)}{\int J_Z\_dc(Inlet\ end)\ (A)} \quad (4.3)$$

Where *U(tip center)* is the potential at the center of the tip opening end, ΔU is the potential drop inside the EFC, $J\ (Inlet\ end)$ is the current density across the inlet end of EFC, and $J_Z\_dc(Inlet\ end)$ is the current density across the inlet end of EFC normal to the circular surface .

Table 4.3 Resistance measurement in electroporation simulation model with small cells (d_c = 10 μm) and 2 μm tip EFC

Tip-cell distance (μm)	Voltage at tip (V)	Current Integration (μA)	Capillary Resistance (MΩ)	System Resistance (MΩ)	Current (μA)
100	4.84035	34.1064	14.51807	14.65999	0.13643
8	4.88908	34.1031	14.51804	14.66141	0.13641
1	5.66939	34.0539	14.51612	14.68261	0.13622
0.5	6.85438	33.9866	14.51001	14.71169	0.13595

By this method, we investigated the resistances of the two types of EFCs with presence of cells at various tip-cell distances at 25 ℃. Table 4.3 shows results for the small cell with 2 μm tip capillary. The EFC resistances obtained in this model are similar to those in Table 4.2. The tip-cell distance changing from 100 μm to 0.5 μm induces only 0.35% change in the computed

current. This tiny change is unreadable in real experiments considering the noise and resolution of the electronics. Simulation with 3.6 μm tip EFCs shows similar results.

4.1.5 Potential and electric field distribution near the EFC tip

Using the model described in 4.1.2, we have examined the electric field distribution around an EFC tip when a pulse for electroporation was applied. Figure 4.2 shows how the potential (surface plot) and electric field distribute near the tip when a capillary having a 2 μm tip is put 15.5 μm away from the cell dish surface. With an apply voltage of 500V, approximately 75% potential drop happens in the untapered section, and more than 20% voltage drop occurs rapidly at the 2 mm tapered section. At the tip where in the figures corresponding to d = 0, the potential is only several volts. The existence of cell barely affects the potential drop across the capillary (plot (C) and (D)). Placing a cell under the capillary induces the formation of a sharp potential drop across the cell membrane (plot (D) insets).

The streamline plots in Figure 4.2 indicate an intense electric field at the tip and an exponentially dropping electric field when going farther into the bath buffer (plot A). The electric field is distorted by the presence of a cell (plot B).

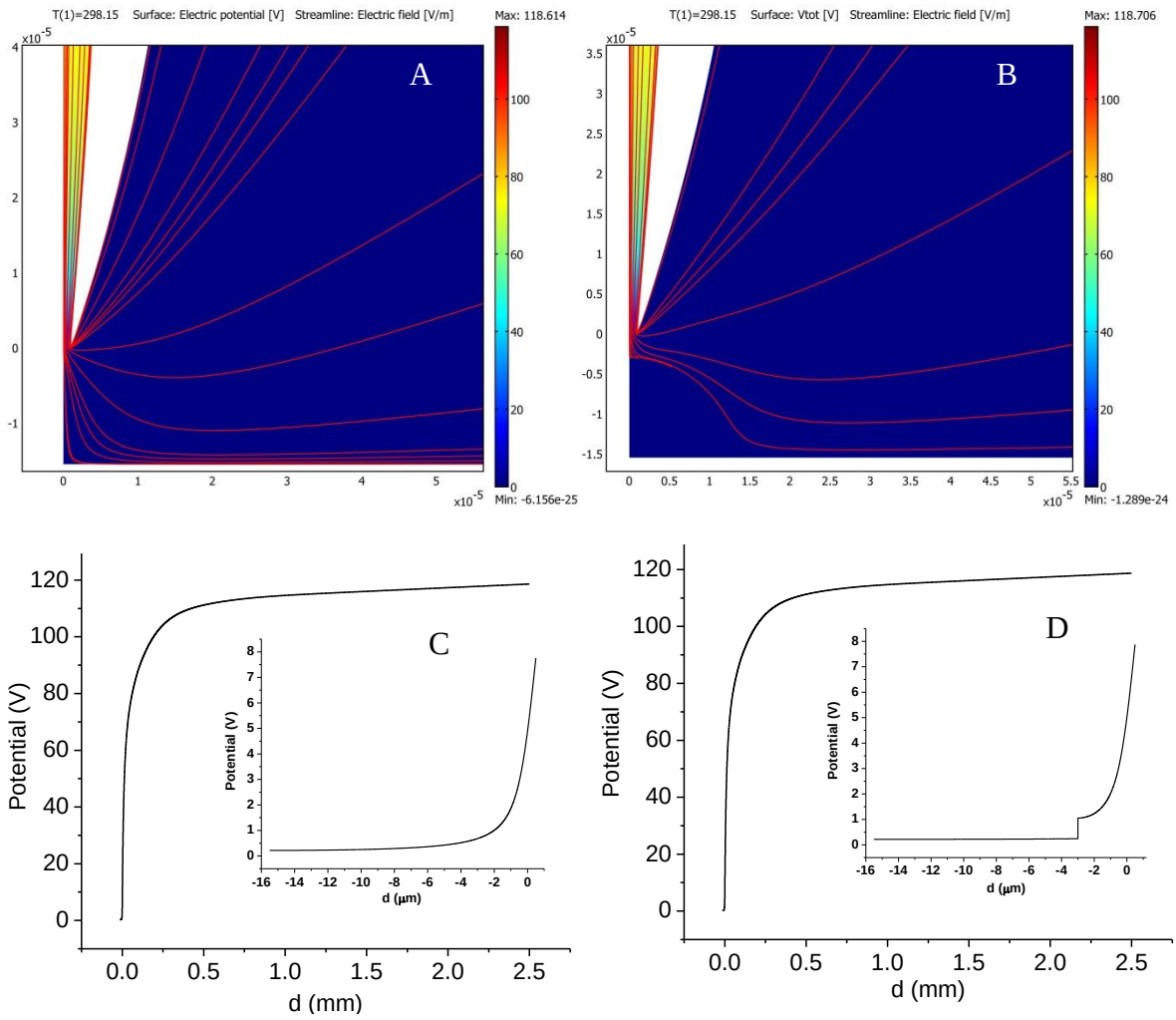

Figure 4.2 Simulated electric field and potential distribution with a 2D axial symmetric model.

(A) and (C): no cell; (B) and (D): with a median-sized cell. (A) and (B) show the surface plots for potential distribution and streamline plots for electric field distribution around the 2 μm tip. (C) and (D) are the potential drop curves along the central axial of capillary, with insets for the extension into the solution/cell.

4.1.6 FEA and TMP for electroporation

This model also gives FEA and TMP as introduced in the beginning of this chapter. TMP corresponds to the difference value between the potential at the outside and inner side of the membrane, and FEA is calculated by dividing the area where TMP ≥ 0.25 V by the whole cell area. Shorter distance means higher TMP and larger FEA. The simulated electroporation behavior at different tip-cell distances with 2 μm and 3.6 μm tips are demonstrated in Figure 4.3.

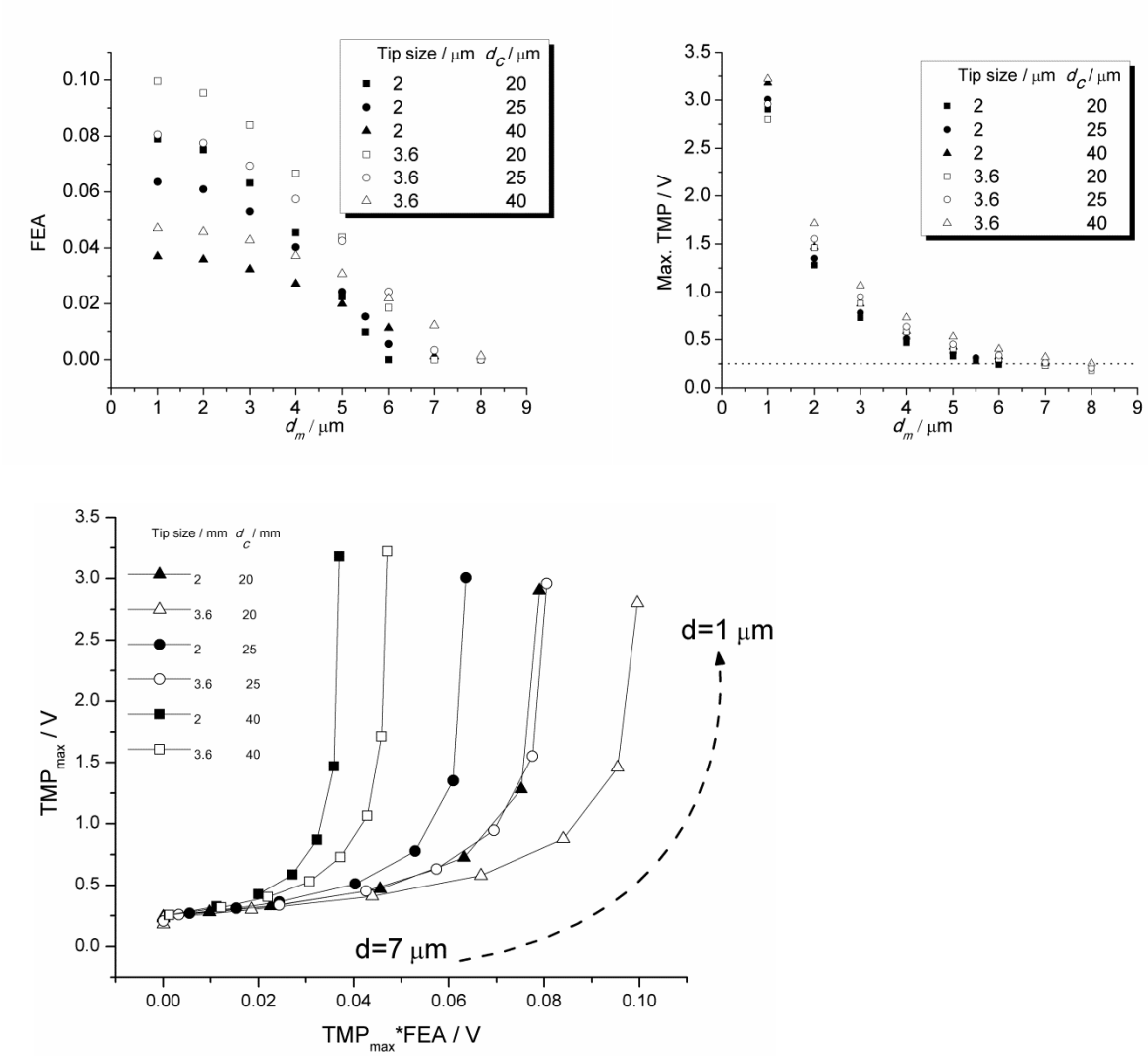

Figure 4.3 Simulated FEA, TMP and their product of a round cell with an applied voltage of 500 V with a 2D axial symmetric model.

The above figure predicts that electroporation happens when the tip-to-cell distance d_m is less than 6-7 μm, with a small variation depending on the cell size and the tip opening. This fits our experimental results well. The alteration of this distance greatly changes the FEA and TMP, which will affects the permeability of the cell membrane and the survivability of the cells directly. With a defined d_m, this model anticipates an increase in FEA with a larger EFC tip and/or a smaller cell, and a relatively greater Maximum TMP with a larger EFC tip and/or a larger cell. From the statistical results given in chapter 3, the survivability of electroporated cells depends on the extent of intracellular molecule loss, which is related directly to the mass transfer rate, and the mass transfer rate is determined by the product of FEA and TMP_{max}. Therefore we can propose that the cell survivability is related to TMP_{max}*FEA, and the probability of pore formation is determined by TMP_{max}. From figure 4.3 at the same TMP_{max}, TMP_{max}*FEA decreases if the EFC tip size decrease or/and the cell size increases. This observation indicates that electroporated cells' survivability benefits from a larger d_m, a larger cell size d_c and a smaller EFC tip. This prediction would be very useful in guiding our attempt in getting simultaneous high electroporation efficiency and high cell survivability. However, the above prediction is only based on the ideal design of a round cell and an upright position of the tip over the cells, and the actual TMP and FEA in the experiments may alters largely from the simulation data. A 3D simulation can make corrections to tip-cell position, and gives closer estimation.

4.2 3D MODELING OF ELECTROPORATION

As we mentioned in the above paragraph, a 3D model helps to examine further how the position of the cell and tip affects electroporation. In this section, we built a 3D model with the same capillary size and shape, and carried out simulation mimicking the relative position of the EFC tip and the cell in real our experiments.

4.2.1 Geometry drawing

To simplify the geometry, we drew the capillary tip with a length of 80 μm. The voltage applied at the wider end of the capillary was calculated from the previous 2D model. For a 2 μm tip, the voltage at the wider end is 84.6 V, which corresponds to an applied voltage of 500 V for the whole capillary with a full length of 15 cm. We borrow this voltage from on the previous results that the when the capillary stays 1 μm away from the tip, the resistance of the whole system remains the same. To avoid the current flow out from the wider end of the tip directly to the ground, we set an insulation layer with a thickness of 1.6 μm above the wider end. The 3D geometry is shown in Figure 4.4. The 3D tip was revolved from a 2D plane and tilted to from an angle of 45^{o} with respect to the dish surface. The height of tip center to the surface of the dish is set to 5 μm.

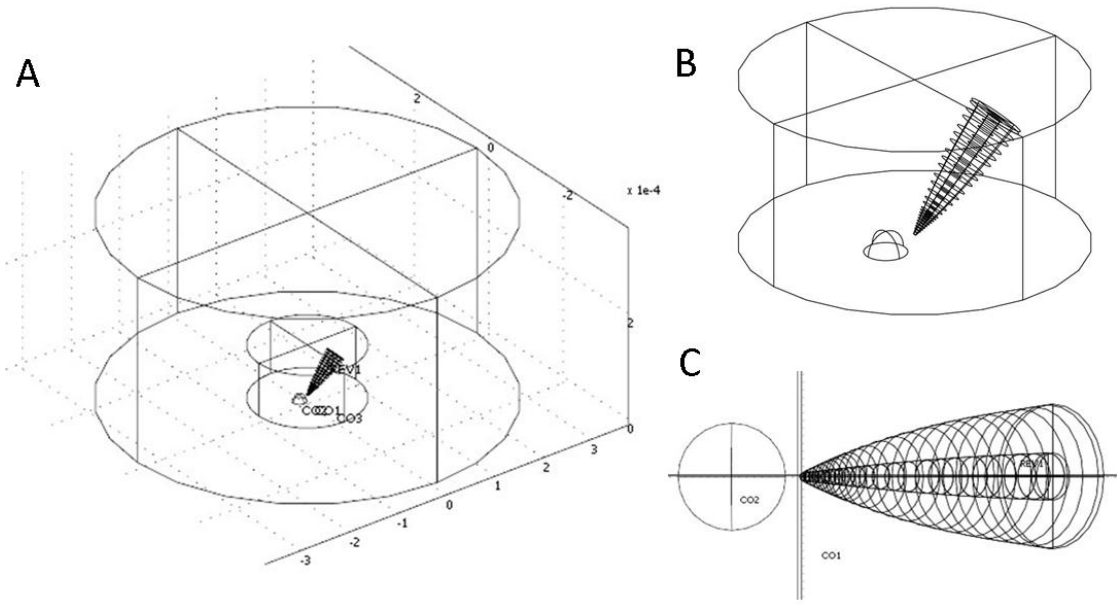

Figure 4.4 Modeling 3D geometry for electroporation.

(A) The whole geometry. The outside large cylinder has a radius of 3.5 mm; the inner smaller cylinder has a radius of 1 mm. This smaller cylinder is drawn for a purpose of a fine mesh of the space around the tip and the cell. The large cylinder is filled with buffer, and its wall is set as ground. (B) A closer look of the small inner cylinder with a target cell and a tip inside. The cell is hemisphere-shape with the same boundary settings in 2D symmetry model. The capillary is composed of three parts: an insulation wall, a buffer-filled lumen and an insulation layer on top of the wider opening. The tip is tilted to from an angle of 45^{o} with respective to the dish surface. The height of the tip center to the dish surface is 5 μm. (C) A perspective view of the cell and the tip.

In this 3D model, how to set the distance between the tip and the cell (d_m) is a little more complicated than in the case of the 2D model. To make the simulation comparable to the experiments, we set the distance d_m as the perspective distance between the tip center and the cell edge. The real shortest distance, which depends on the cell size and the relative position of the tip, shall be a value between d_m and $\sqrt{2}d_m$.

A good mesh was obtained by setting fine maximum mesh element sizes. The cell membrane was set to 0.5 μm, inner cylinder was set to 5 μm, the capillary inner wall was set to 1 μm, and the tip opening was set to 0.2 μm, with a grow rate of 1.1(the grow rate determines how fast the elements grow from small to large over the domain. The number 1.1 means the elements adjacent to the small elements are 1.08 larger than the small ones).

4.2.2 Simulated TMP and FEA with 3D modeling

Using the similar settings as in 2D axial symmetry, we obtain FEA and TMP from this 3D model. Figure 4.5 shows a sample surface distribution pattern of calculated TMP on the membrane of a 25-μm-diameter cell using a 2-μm tip from a distance of 4 μm. The dark red area has the maximum TMP around 0.44 V, the TMP decreases gradually as the color bar shifts outside from dark red to the bulk area of blue. The area with TMP above a critical TMP of 0.25 V (yellow-colored) is the electroporated region, which can be seen from the model straightforwardly.

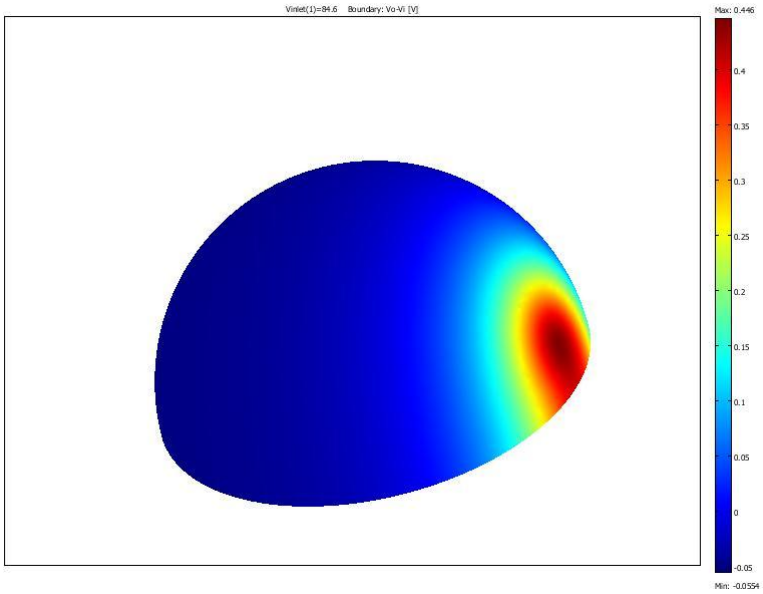

Figure 4.5 Surface distribution of calculated TMP on a hemisphere cell membrane under an applied voltage of 500 V in a 3D model.

The value of calculated TMP decreases gradually as the color alters from dark red to blue. The dark red area is the spot where the capillary tip points to. In this sample model, a cell with a diameter of 25 μm was electroporated using a 2-μm-opening tip with a distance d_m of 4 μm.

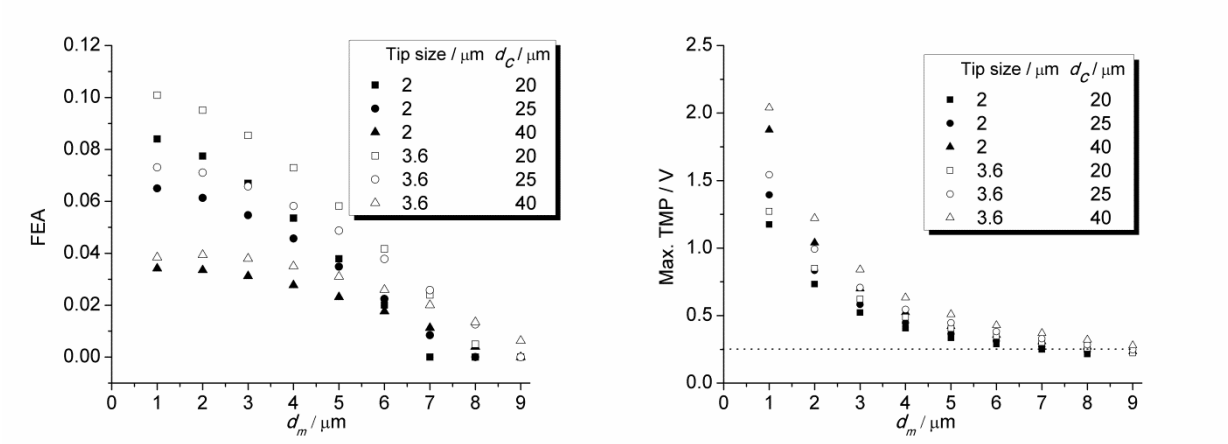

Figure 4.6 Simulated FEA and TMP of a hemisphere cell with an applied voltage of 500 V with a 3D model.

Figure 4.6 demonstrates the calculated FEA and maximum TMP for a hemisphere cell with various sizes at d_m=1 - 9 μm using tips of 2-μm or 3.6-μm opening. The trend that the maximum TMP/FEA changes when d_m increases is similar to the outcomes from 2D models. Different from a widely open cell membrane in a 2D model, in a 3D model the cell membrane area facing the tip is limited. This 3D model gives a very good platform to understand experimental results. For example, the computed ln(TMP_{max}*FEA) is found to be linearly related to the cell-to-tip distance, which helps to explain the linear relationship between ln(M) and cell-to-tip distance in real experiments. The computed slopes fit well with coefficient produced in the linear regression for different EFC tips.

4.3 MASS TRANSPORT MODELING AROUND A TIP UNDER ELECTROPORATION PULSES

As mentioned in the chapter 2, we are interested in investigating the mass transport process during SCEP for different molecules such as dyes, DNA plasmid and small molecules. Understanding of this process is of particular importance when we intended to apply SCEP for delivery of molecules from the capillary tips into cells. I have built a 2D axial symmetry time-dependent finite element model for this purpose involving the studies of multiple factors including potential distribution, diffusion, convection and electrokinetic flow. It helps us understand and predict the delivery of target molecules depending on their molecular properties at given experimental conditions.

4.3.1 Model and Parameters

In this simulation, we used a simple geometry composed of a real-shaped 2-μm tip opening capillary and the surrounding buffer in a dish. The capillary tip was placed 20 μm from the dish surface, and the side wall of the dish was set 0.5 mm away from the symmetry axis. This simulation adopted three application modes in the Comsol program: Conductive Media DC, Incompressible Navier-Stokes and Electrokinetic Flow (Chemical Engineering Module). The conductive Media DC results were calculated with the same settings as discussed in 4.1.2 except that the cell was excluded from the drawing and only the outside cell domains, d_{cout}, kept effective. The Incompressible Navier-Stokes solved the continuity equation $\nabla \cdot \mathrm{u} = 0$ and a momentum balance equation $\rho \frac{\partial \mathbf{u}}{\partial t} + \rho(\mathbf{u} \cdot \nabla)\mathbf{u} = \nabla \cdot [-p\mathbf{I} + \eta(\nabla \mathbf{u} + (\nabla \mathbf{u})^T)]$; here $\mathbf{u}$ is the bulk flow velocity vector, ρ is the solution density, η is the solution dynamic viscosity and p is the pressure. The electroosmotic flow inside the capillary was computed by setting the capillary as a moving wall with a velocity calculated from $v_{wall} = -\frac{\varepsilon \zeta_{wall}}{\eta} E$. Here ε is the electric permittivity, ζ_{wall} is the zeta potential of the capillary wall (set as $-0.05\ V$ [143]) and E is the electric field obtained from Conductive Media DC mode. The pressure p was set from the wider, proximal end of the capillary, and the open surface of the buffer was set as pressure 0 with no viscous stress. The dish walls were set as no slip wall ($\mathrm{u} = 0$). The last mode is Electrokinetic Flow Application solving the Nernst – Planck equation $\frac{\partial c}{\partial t} + \nabla \cdot (-D\ \nabla c - z\ u_m F\ c\ \nabla V + c\ \mathbf{u}) = 0$ with a continuity equation of $\mathbf{n} \cdot (\mathbf{N_1} - \mathbf{N_2}) = 0$ where $\mathbf{N_1}$ and $\mathbf{N_2}$ stand for inward and outward flux, respectively. Here D is the diffusion coefficient of the molecule, c is the concentration of the molecule, z is the electric charge of the molecule, u_m is the mobility of the molecule and N is the mass flux vectors for the molecule calculated from $\mathbf{N} = -D\ \nabla c -$

$z\,u_m\,F\,c\,\nabla V + c\,\mathbf{u}$. The velocity, **u**, is equal to the velocity of the bulk flow obtained from the Incompressible Navier-Stokes mode. In this mode we assumed that the solute is at infinite dilution, so its contribution to the solvent's velocity is negligible in comparison to the solvent's contribution to the solute. Our model simulated the mass transport process during SCEP, where a capillary filled with solute in buffer was exposed to bulk solute-free buffer solution. The bulk solution volume is much larger than the volume of capillary, which allows us to set the solute concentration as $1\,mol/m^3$ inside capillary and 0 far away into the bulk buffer. Note in all three modes the interface of the solute-containing buffer and the solute-free buffer was set as continuity boundary. To mimic the process that the pulse turns on after free diffusion of the solute, we used a smoothed step transition function $V_0 = 91 * flc1hs(-1.0001 + t, 0.0002)$ for description of the voltage applied on the wider, proximal end of the capillary after 1 s of free diffusion.

Table 4.4 Parameters and constants for simulation of mass transport under electric pulses

Dynamic viscosity η	$0.89 \times 10^{-3}\ Pa \cdot s$
Capillary zeta potential ζ_{wall}	$-0.050\ V$
Conductivity σ	$1.6\ S/m$
Electric permitivity ε	$0.71\ nF/m$
Plasmid diffusion coefficient D	$5.94 \times 10^{-8}\ cm^2/s$
Plasmid electrophoretic mobility μ_p	$-3.18 \times 10^{-4}\ cm^2/(V \cdot s)$

Table 4.4 gives the parameters and constants used in the mass transport simulation. The diffusion coefficient and electrophoretic mobility are subject to change as we change the solute types. Note that in Comsol the charge *z is* a number and the unit of electrophoretic mobility is

$s \cdot mol/kg$. For simulations other than the plasmid, the mobility is calculated by $D/(R_g \times T)$ where R_g is the gas constant ($8.314\ J/(mol \cdot K)$) and T is the temperature (298.15 K). For the modeling of plasmid we use an equation $u_m = \frac{\mu_p}{zF}$ where μ_p is the electrophoretic mobility with a unit of $m^2/(V \cdot s)$ and F is the Faraday constant. In practice, we set z as 1 and set $u_m = \frac{\mu_p}{F}$ where $F = 96{,}485.3365\ C/mol$. The plasmid we simulate here is the pEGFP-C2 plasmid as we mentioned in the previous chapter of transfection by electroporation. The plasmid D and μ_p are estimated values obtained from a paper published by Nancy Stellwagen's group [144].

The mesh is done based on the default extra fine mesh plus a maximum element size of $9 \times 10^{-7}\ m$ around the tip, an element layer of 10 in horizontal axis inside the capillary and a grow rate of 1.08 around the tip. The final number of elements is 108230 with a degrees of freedom of 575590.

4.3.2 Modeling of solute mass transport with defined *D* and *z*

We have simulated mass transport for solute molecules with different D and z with or without external pressure. In the following modeling, a pulse having a magnitude of 500 V and duration of 300ms is applied after 1s of free diffusion. The results show without external pressure during the pulse, the electroosmotic flow overwhelms electrophoretic flow and pushes molecules outside the tip when D is $2 \times 10^{-7}\ cm^2/s$. Negative charge and larger D holds back this process, while a positive charge accelerates it. Figure 4.7 is a surface plot of concentration for a molecule with D of $2 \times 10^{-5}\ cm^2/s$ and z of +1 giving out the concentration distribution over time. The left upper plot shows negligible distribution of molecules outside the tip after 1s of free diffusion. The right upper plot shows after the pulse is turned on, solute molecules are

quickly pushed out from the tip to form a "cloud" with a round-curved frontier. With a pulse length of 300 ms, this "cloud" intrudes further into the outside-tip domain, as demonstrated in the left bottom plot. Figure 4.8 shows the effect of charge and diffusion coefficient on solute concentration distribution after a 300 ms pulse. We find the electroosmotic flow is overwhelming with a small *D* (relates to a small electrophoretic velocity), and the diffusion is always negligible with the settings we have. However, as *D* increases, the counteracting electrophoretic velocity increases and finally exceeds the electroosmotic flow. We have simulated the mass transport with a molecule having a $D = 2 \times 10^{-5}\ cm^2/s$ and $z = -1$ under the same pulse. The left plot in Figure 4.8 shows the result: the electrophoretic flow exceeds the electroosmotic flow and the molecules are forced into the capillary from the outside domain. We can infer that if an intracellular molecule has a diffusion coefficient and charge number similar to the one in the left plot in Figure 4.8 it can be sampled into the capillary under electroporation. As *D* increases, a wider concentration distribution of molecules around the curve pattern edge is expected as shown in the left bottom plot of Figure 4.7 when compared to the right plot in Figure 4.8.

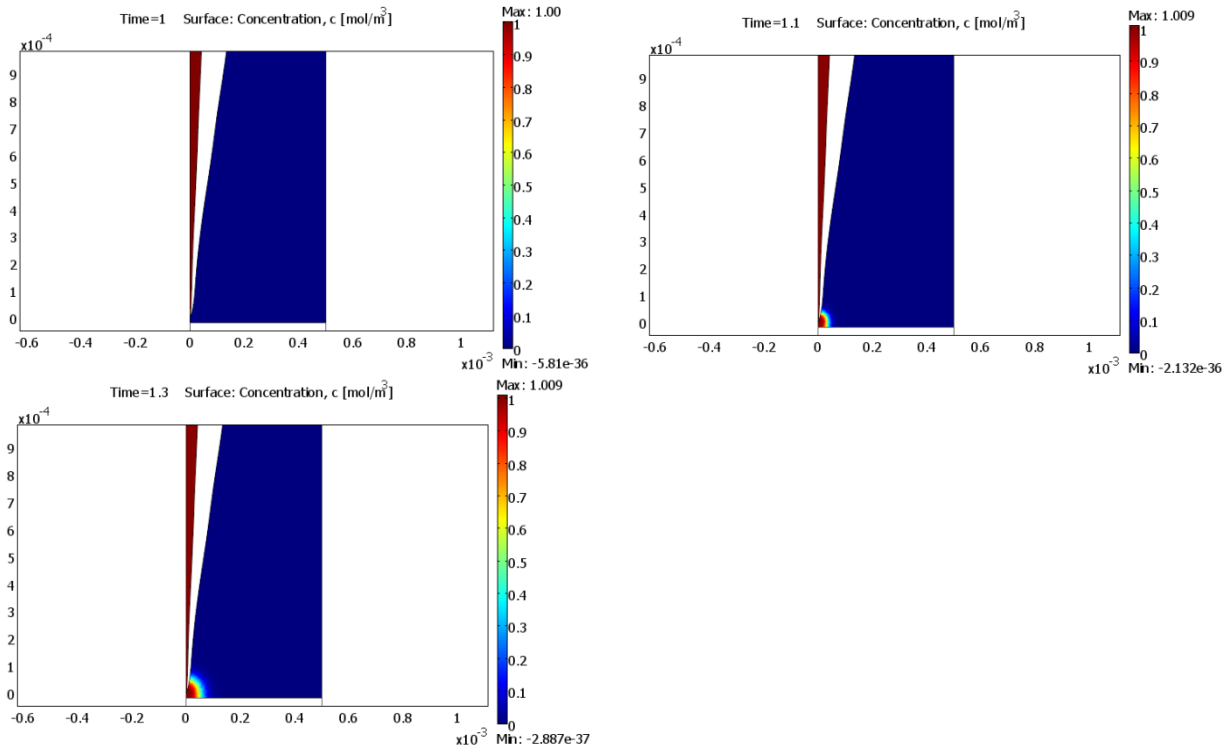

Figure 4.7 Simulated concentration distribution under a pulse wit $D = 2 \times 10^{-5}\ cm^2/s$ and $Z = +1$.

The capillary starts with a solute concentration of $1\,mol/m^3$ and the outside compartment starts with a concentration of 0.

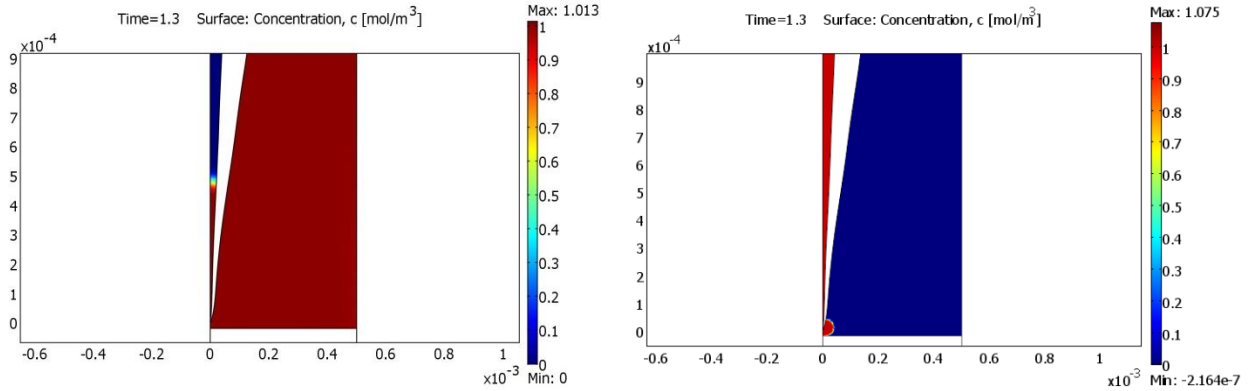

Figure 4.8 Simulated effect of charge and diffusion coefficient on mass transfer under pulses.

Left plot: The capillary starts with a concentration of 0 and the outside compartment starts with a concentration of $1\,mol/m^3$. $D = 2 \times 10^{-5}\ cm^2/s, z = -1$. Right plot: The capillary starts with a concentration of $1\,mol/m^3$ and the outside compartment starts with a concentration of 0. $D = 2 \times 10^{-7}\ cm^2/s, z = -1$.

By integration of the flux through the cross area of the tip opening over unit time, we can calculate the amount of material transported outside the tip and the net solute flow rate. Figure 4.9 gives the total solute amount flows out from the tip into the bulk solution over time and Table 4.5 gives the calculated net solute flow rate for different D and z. Note that when $D = 2 \times 10^{-5}\ cm^2/s, z = -1$, Figure 4.9 shows no obvious alteration of solute molecules outside the tip (grey line), which is because the solute molecules are pulled back into the capillary. Calculation of the flow rate under this circumstance is obtained from decrease amount of the integrated solute moles inside the capillary, or by setting the capillary concentration as 0 and the bulk outside space as 1 mol/m^3. These two approaches give the same results, which is listed in Table 4.5. Modeling with pEGFP-C2 plasmid based on the estimated D and μ_p confirms our previous postulation that the electroporation pulses deliver pEGFP-C2 plasmid into target cells through electroosmotic flow.

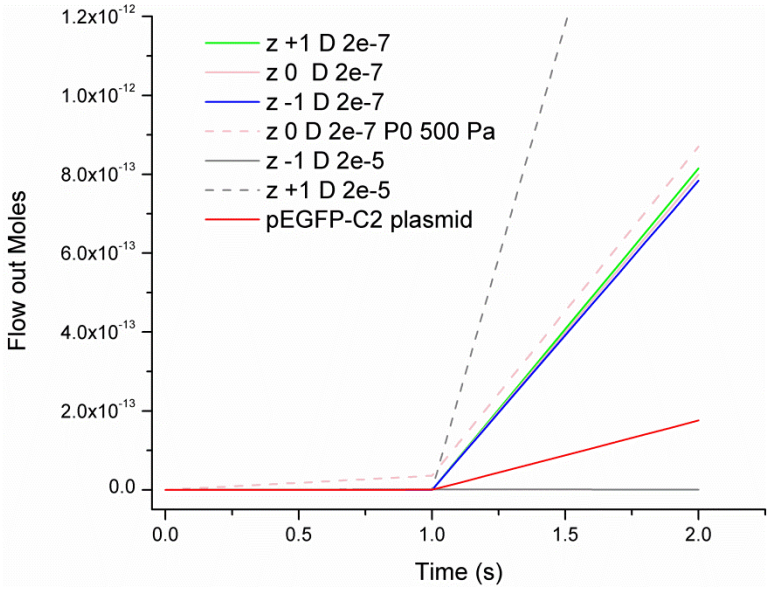

Figure 4.9 Simulated solute transport with a variation of molecular charge and diffusion coefficient using a 2-μm opening capillary tip.

Red line: pEGFP-C2 plasmid; Pink dash: Neutral solute molecules, $D = 2 \times 10^{-7}\ cm^2/s$, with an external pressure added from the wide end of the capillary $P_0 = 500\ Pa$; Others represent molecules with defined molecular charge and diffusion coefficient without external pressure. The unit of *D* is cm^2/s.

Table 4.5 Simulated net flow rate of different types of solute molecules under an electroporation pulse

Molecule type	Net Velocity $/mol \cdot s^{-1}$
z +1, *D* $2 \times 10^{-7}\ cm^2/s$	8.15×10^{-13}
z 0, *D* $2 \times 10^{-7}\ cm^2/s$	7.99×10^{-13}
z -1, *D* $2 \times 10^{-7}\ cm^2/s$	7.84×10^{-13}
z 0, *D* $2 \times 10^{-7}\ cm^2/s$, P_0 500 Pa	8.35×10^{-13}
z -1, *D* $2 \times 10^{-5}\ cm^2/s$	-7.60×10^{-13}
z +1, *D* $2 \times 10^{-5}\ cm^2/s$	2.32×10^{-12}
pEGFP-C2 plasmid	1.76×10^{-13}

4.3.3 Effect of external pressure on solute mass transport

As illustrated in Figure 4.9 and Table 4.5 we have examined the effect of pressure on solute mass transportation. The pressure is set as 500 Pa to mimic the pressure produced from the height of a full length capillary filled with extracellular buffer in our electroporation experiments. This external pressure applied at the top of the capillary accelerates the flow of solute molecules from the tip. Figure 4.10 shows a flow with the aid of external pressure. An irregularly shaped solute "cloud" is forced out by the external pressure without applied pulses. However, once the pulse is on a dominating electrokinetic flow can rapidly tune the "cloud" into a rounded-frontier one.

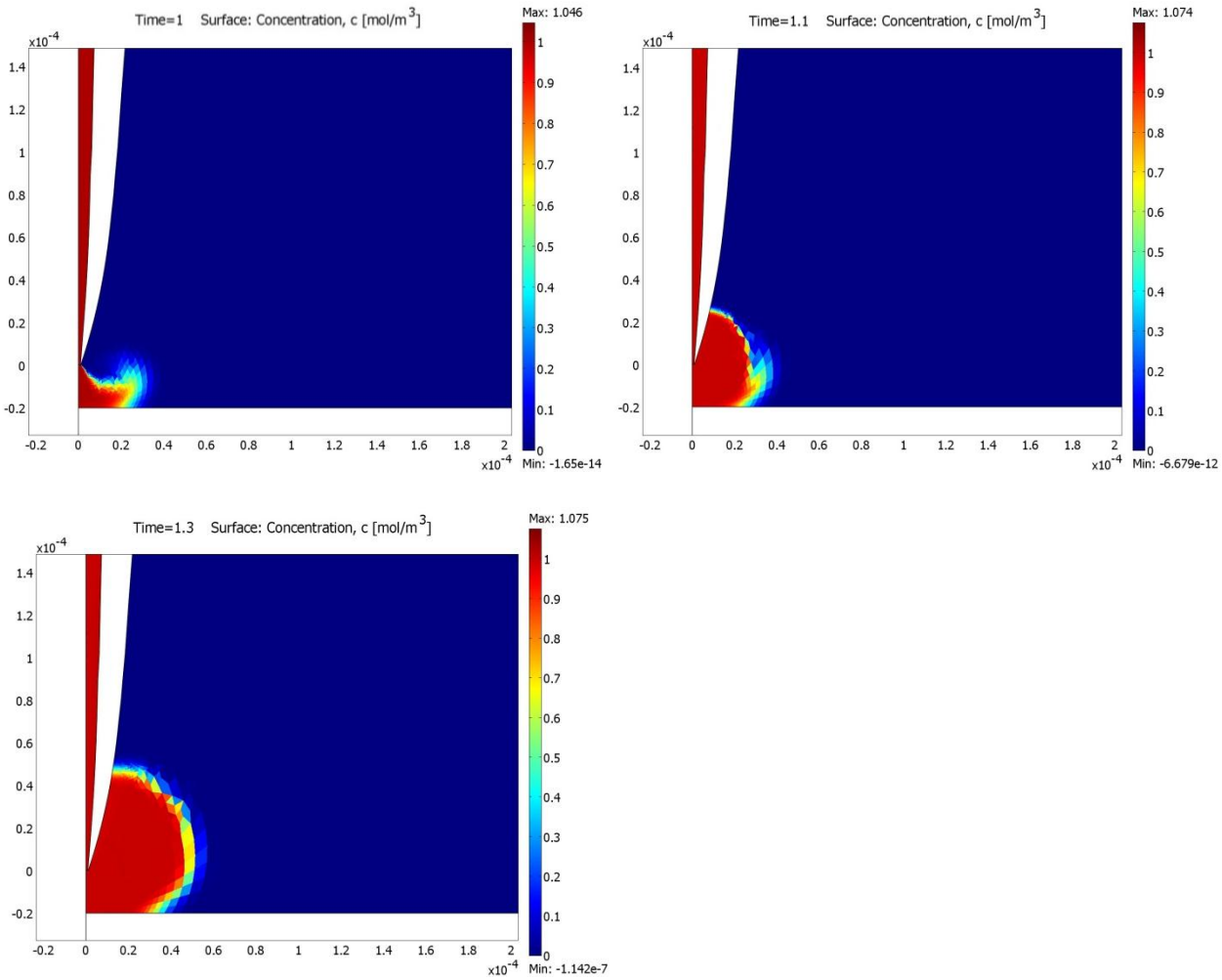

Figure 4.10 Simulated neutral solute concentration distribution under a pulse with an external pressure

The capillary starts with a solute concentration of $1\,mol/m^3$ and the outside compartment starts with a concentration of 0, $D = 2 \times 10^{-7}\ cm^2/s$.

4.4 MODELING MASS TRANSPORT AT A CONJUNCTION OF A PULLED CAPILLARY AND CHARGED POROUS MEDIUM UNDER ELECTRIC FIELD

The above mass transport model can also be extended to other simulations for mass transport under external electric field around a fine tip. For example, we have set up a model to simulate the delivery of solutes through a pulled pipette tip into porous medium by electric current, which is used to mimic the process of delivery of molecules into brain tissues. The porous medium has a certain zeta potential, so electroosmotic flow is expected in it.

A commercial finite element method (FEM) program Comsol 3.5a (Comsol, Burlington, MA) has been used to perform calculations. We have done the simulation with a 2D axial symmetrical geometry based on a real tip. We drew the pipette from 24 points measured from an image of a typical pipette used in our experiments. The simulated pipette consisted of a 2.5 mm tapered section and a 0.5 mm non-tapered section. A box standing for the porous medium conjoined the tip and filled the outside space with a radius of 10 mm and a height of 13 mm. The pipette, filled with free solution, was placed so that the tip was 3 mm below the top surface of the porous medium. The porous medium was pushed into the capillary by a depth of 0.5 μm. The wall of the pipette was set as inactive domain in the model and the end of the tip was smoothed to avoid mesh problems. The whole geometry contains two domains: a free solution domain and a porous medium domain.

Three modes are applied to get the transient or steady-state solution. The first mode is Conductive Media DC. It solved the equation

$$\nabla \cdot (\sigma \nabla V - \mathrm{J}^{\mathrm{e}}) = 0 \qquad (4.4)$$

with appropriate boundary conditions; here V is potential, σ is conductivity and J^e is an externally generated current density. An inward current flow of $J^e{}_0 = 0.5\,\mu A/cm^2$ was set at the wide end of the pipette. In free solution domain eq.4.4 is the exact equation solved using the conductivity of free solution $\sigma = \sigma_0$ and $J^e = J^e{}_0 = 0.5\,\mu A/cm^2$. In the porous medium domain, eq. 4.4 needs modification. Assume the pores in a porous medium is often modeled as a an array of *N* cylindrical pores which wind in solid medium, and the average pore size is a_p, the porosity can be expressed as

$$\phi = \frac{N\pi a_p^2 l}{AL} \qquad (4.5)$$

where *l* is the length of the cylinder, *A* is the cross-sectional area of the porous medium, and *L* is the length of the porous medium. The tortuosity can be defined as

$$\lambda = \frac{l}{L} \qquad (4.6)$$

Assume that the porous medium is only conductive in the solution-filled pores, the intrinsic average current density inside pores can be written as

$$J_p^e = J_{app}^e \frac{A}{N\pi a_p^2} \qquad (4.7)$$

where J_{app}^e is the apparent current density in the macroscopic medium. From the above three equations we get

$$J_{app}^e = J_p^e \frac{\phi}{\lambda} \qquad (4.8)$$

The intrinsic current density J_p^e can be computed by Ohm's law in the microscopic pores

$$J_p^e = \sigma E_p \qquad (4.9)$$

where σ is the conductivity of solution in the pores and E_p is the effective electric field inside the pores. E_p is related to potential drop across the cylinder ΔV by

$$E_p = \frac{\Delta V}{l} \qquad (4.10)$$

Write the apparent electric field across the porous medium as

$$E_{app} = \frac{\Delta V}{L} \qquad (4.11)$$

The apparent current density in porous medium is then given by

$$\mathrm{J}^e_{app} = \frac{\phi\sigma}{\lambda^2} E_{app} \qquad (4.12)$$

The full equation for Conductive Media DC mode in porous medium becomes

$$\nabla \cdot \left(\frac{\phi\sigma}{\lambda^2} \nabla V - \mathrm{J}^e_0\right) = 0 \qquad (4.13)$$

where $\frac{\phi\sigma}{\lambda^2}$ can be considered as the apparent conductivity for the porous medium.

The bulk fluid flow velocity is solved in the second mode. For the free solution inside the pipette, the Incompressible Navier-Stokes mode is used, solving a continuity equation $\nabla \cdot \mathrm{u} = 0$ and a momentum balance equation $\rho \frac{\partial \mathbf{u}}{\partial t} + \rho(\mathbf{u} \cdot \nabla)\mathbf{u} = \nabla \cdot [-p\mathbf{I} + \eta(\nabla\mathbf{u} + (\nabla\mathbf{u})^T)]$; here $\mathbf{u}$ is the bulk flow velocity vector, ρ is the solution density, η is the solution dynamic viscosity and p is the pressure. In porous medium domain, Brinkman Equations applies, with an assumption of a low Reynolds number, low flow speed and small pores, solving a continuity equation $\nabla \cdot \mathbf{u} = 0$ and a momentum balance equation

$$\frac{\rho}{\phi} \frac{\partial \mathbf{u}}{\partial t} + \frac{\eta}{\kappa}\mathbf{u} = \nabla \cdot \left[-p\mathbf{I} + \frac{\eta}{\emptyset}(\nabla\mathbf{u} + (\nabla\mathbf{u})^T)\right] + \mathbf{F} \qquad (4.14)$$

where $\mathbf{u}$ is the volume-averaged velocity vector, ρ is the solution density, ϕ is the porosity, η is the dynamic viscosity, p is the pressure, κ is the permeability of the porous medium calculated from the equation $\kappa = \frac{\emptyset\, m^2}{k_0\, \lambda^2}$, m is the pore radius, k_0 is a factor of the pore shape (set as 2 for cylinder pores), λ is the tortuosity of the medium and $\mathbf{F}$ is the body force vector.

The electroosmotic flow inside the pipette was computed by setting the pipette wall as a moving wall with a velocity calculated from $v_{wall} = -\frac{\varepsilon\,\zeta_{wall}}{\eta}\,E$, while the electroosmictic flow in the porous medium was set as a body force calculated by $\mathbf{F} = -\frac{k_0 \varepsilon\,\zeta_{gel}}{m^2}E$. Here ζ_{wall} is the zeta potential of the pipette wall, ζ_{gel} is the zeta potential of the porous medium and E is the electric field obtained from Conductive Media DC mode. Putting electroosmotic flow into eq. 4.14 gives the full equation we solve for Brinkman's equation mode as

$$\frac{\rho}{\phi}\frac{\partial \mathbf{u}}{\partial t} + \frac{k_0\,\lambda^2\eta}{\emptyset\, m^2}\mathbf{u} = \nabla \cdot \left[-p\mathbf{I} + \frac{\eta}{\emptyset}(\nabla\mathbf{u} + (\nabla\mathbf{u})^T)\right] - \frac{k_0 \varepsilon\,\zeta_{gel}}{m^2}E \qquad (4.15)$$

from where we can calculate the volume-averaged macroscopic velocity of bulk flow $\mathbf{u}$, and a microscopic bulk flow velocity

$$\mathbf{u}' = \frac{\lambda \mathbf{u}}{\phi} \qquad (4.16)$$

The last mode is Electrokinetic Flow Application solving the Nernst – Planck equation

$$\frac{\partial c}{\partial t} + \nabla \cdot (-D\,\nabla c - z\,u_m\,F\,c\,\nabla V + c\,\mathbf{u_{N-P}}) = 0 \qquad (4.17)$$

with a continuity equation of $\mathbf{n} \cdot (\mathbf{N}_1 - \mathbf{N}_2) = 0$. The mass flux vectors for the solute $\mathbf{N} = -D\,\nabla c - z\,u_m\,F\,c\,\nabla V + c\,\mathbf{u_{N-P}}$. In this mode we assume that the solute is infinitely diluted, so solute's contribution to the solvent's velocity is negligible in comparison to the solvent's contribution to the solute.

In the free solution domain inside the pipette, the exact eq. 4.17 is solved with $D = D_0$, $u_m = u_{m\,0}$ and $\mathbf{u_{N-P}} = \mathbf{u}$. Here D_0 is the free diffusion coefficient of the solute, $u_{m\,0}$ is the free electrophoresis mobility of the solute.

In porous medium, this equation solves the solute flow in microscopic pores using D as free diffusion coefficient of the solute, c as the concentration of the solute in microscopic pores, z as the electric charge of the solute, and u_m as the free mobility of the solute. We need to

transform eq. 4.17 to get a volume averaged solute concentration, $\bar{c}$. For small molecules, their travel in porous medium is hindered by the geometry tortuosity, and the velocity, $\mathbf{u}_{N-P}$, is equal to microscopic bulk flow velocity $\mathbf{u}'$ in eq. 4.16 obtained from the Brinkman Equation mode. The macroscopic volume-averaged solute concentration can be calculated from $\bar{c} = \phi c$. Substituting c with $\frac{\bar{c}}{\phi}$, $\mathbf{u}_{N-P}$with $\frac{\lambda \mathbf{u}}{\phi}$ in eq. 4.17, and use tortuosity λ for dimension conversion, we get a full Nernst-Planck equation for small molecule solute flow as

$$\frac{\partial \bar{c}}{\partial t} + \nabla \cdot \left(-\frac{D}{\lambda^2} \nabla \bar{c} - z \frac{u_m}{\lambda^2} F \bar{c} \nabla V + \frac{\bar{c}\,\mathbf{u}}{\phi} \right) = 0 \qquad (4.18)$$

For large molecules, their travel inside the porous medium comes from the geometry tortuosity plus extra hindrance caused by large sizes, friction and so on. We can denote an extra term for the add up of other hindrance factors as λ_m. Now a new term $\lambda' = \lambda \lambda_m$ has to be taken into the dimension conversion, and we get a full equation for macromolecule solute flow as

$$\frac{\partial \bar{c}}{\partial t} + \nabla \cdot \left(-\frac{D}{\lambda^2 {\lambda_m}^2} \nabla \bar{c} - z \frac{u_m}{\lambda^2 {\lambda_m}^2} F \bar{c} \nabla V + \frac{\bar{c}\,\mathbf{u}}{\phi \lambda_m} \right) = 0 \qquad (4.19)$$

Note that in all three modes the interface of the pipette and the porous medium was set as continuity boundary. A ‘parametric segregated’ stationary solver or a ‘time-dependent parametric segregated’ solver was applied to get rapid and reasonable converged calculation results. Again we set z as 1 and convert the mobility by $u_m = \frac{\mu_p}{F}$.

From the above model we can get simulated results such as velocity field, electric field, concentration distribution and calculate the total solute amount transported from the tip into porous medium in any defined region at both transient state and steady state, as well as calculating the time required to reach steady-state.

The purpose of above model is to inspire modeling of molecule transfer between different phases around a tip. It can easily expand to other situations such as adding another

pipette for sampling from a porous medium, changing the interface characteristics or adding a third phase. However, since we have not taken in consideration other effects such as temperature, surface tension, adsorption and porous medium characteristic alteration under heat and electric field, the above model needs further optimization to mimic the real experimental outcomes.

APPENDIX A

CAPILLARY PULLING

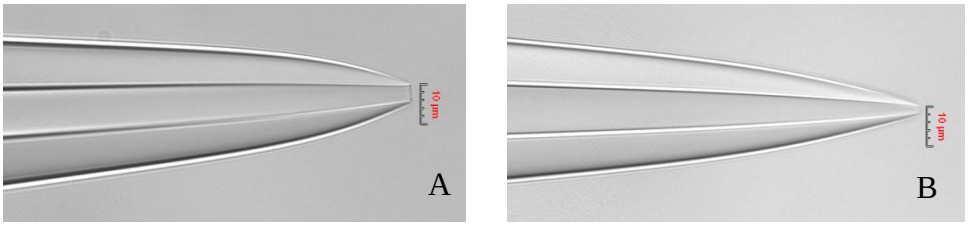

Figure AA. 1 Pictures of pulled capillaries under microscope (40×). The taper length is about 2 mm. (A) i.d. 4-5 µm. (B) i.d. ~ 2 µm.

Table AA. 1 Programs for capillary pulling

Line No.	4-5 µm					~2 µm				
	Heat	Filament	Velocity	Delay	Pull	Heat	Filament	Velocity	Delay	Pull
1	250	0	30	200	0	250	0	30	200	0
2	250	0	30	200	0	250	0	30	200	0
3	250	0	30	200	0	250	0	30	200	0
4	254	0	30	200	0	270	0	30	200	0

APPENDIX B

DEDUCTION OF SCEP FLUORESCENCE DECAY MODEL EQUATION

We modified a quantitative model presented by Puc *et al*., [43] to fit the fluorescence intensity decay curves upon electroporation. This model describes the transmembrane transport of small molecules caused by electroporation. We get an equation from the model to fit a whole-cell fluorescence decay profile upon electroporation as follows.

$$I(t) = I_0 e^{(-kt)} e^{[K(e^{-\alpha t}-1)]} \quad \text{(AB1)}$$

$$K = \frac{M}{\alpha} \quad \text{(AB2)}$$

In equation (AB1), *t* is time from the start of the pulse, *I(t)* is the fluorescence intensity at time t, I_0 is the fluorescence intensity at $t = 0$, k is the photobleaching rate (s^{-1}), M is the mass transfer rate (s^{-1}) through the transient pores and α is the pore resealing rate (s^{-1}). Equation (AB1) has a photobleaching term and an electroporation term.

In this section, we demonstrate the deduction of the electroporation term from the model published by Puc *et al*. In the following paragraphs, the concentration of Thioglo 1-GSH adduct is used, which is linearly proportional to the fluorescence intensity. As mentioned in Chapter 2, our modifications are made based on (1) The cell volume (several pL) is much smaller than the buffer solution surrounding the cells (2 mL); (2) the pulse duration (300 ms) is negligible when

compared to the whole electroporation kinetic process; (3) The fluorescence intensity has a linear relationship with the concentration of Thioglo 1-GSH inside the cells.

THE ORIGINAL MODEL PRESENTED BY PUC'S GROUP

Figure AB.1 is a two-compartment pharmacokinetic model they constructed describing the diffusion-driven transmembrane transport of small molecules caused by electropermeabilization. Figure AB.2 is a model simulating the behavior of electroporation process. The permeabilization of cell membrane is split into a permeabilizing phase that takes place during the pulse, and a resealing phase that begins after the pulse. Based on these models equation (AB1) and (AB2) have been introduced for the calculation of the concentration of small molecules inside cells and outside cells during electroporation.

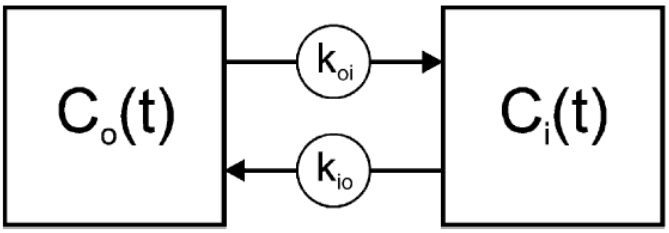

Figure AB. 1 The two-compartment pharmacokinetic model.

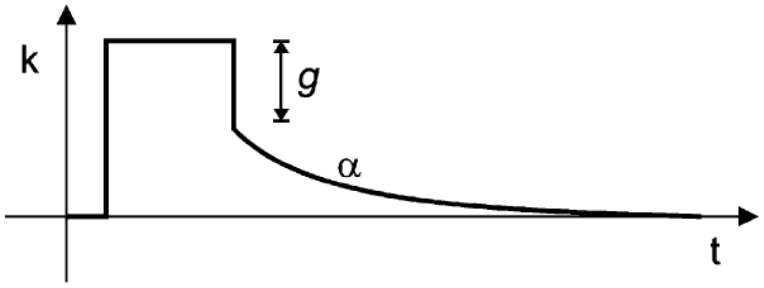

Figure AB. 2 The time course of the voltage applied to the electrodes, and the corresponding variation of coefficient k with time due to permeabilization and resealing of cell plasma membrane.

$$\frac{dC_i}{dt} = k_{io}(C_o - C_i) \qquad \text{(AB3)}$$

where C_o and C_i are external and internal concentration, respectively, k_{io} is a coefficient describing flow between the two compartments and t is time.

The paper simulated the electroporation behavior by introducing a time variation of the coefficient k_{io} as following:

$$k_{io} = \begin{cases} M, & 0 < t \leq T \\ gMexp(\alpha(T-t)), & T < t \leq \infty \end{cases} \qquad \text{(AB4)}$$

in which M is the mass transfer rate (s^{-1}) through the transient pores, α is the pore resealing rate (s^{-1}), g is a parameter that characterizes fast resealing immediately after the end of the pulse, T is the pulse duration and t is the time elapsed from the onset of the pulse.

OUR MODIFICATION

Due to the small volume of cells, we have $C_o \to 0$. From (AB3) and (AB4) we obtain

$$\frac{dC_i}{dt} = \begin{cases} -MC_i, & 0 < t \leq T \\ -gMexp(\alpha(T-t))C_i, & T < t \leq \infty \end{cases}$$

When $0 < t \leq T$,

$$\int \frac{dC_i}{C_i} = \int -Mdt$$

$$lnC_i = -Mt + P_1$$

Set $C_i = C_0$ when $t = 0$, then $P_1 = lnC_0$

$$lnC_i = -Mt + lnC_0$$

$$\int ln\frac{C_i}{C_0} = \int -Mt$$

$$C_i = C_0 \exp(-Mt)$$

When $T < t \leq \infty$,

$$\int \frac{dC_i}{C_i} = \int -gMexp(\alpha(T-t))dt$$

$$lnC_i = \frac{gM}{\alpha} \int \exp(\alpha(T-t))d(\alpha(T-t))$$

$$lnC_i = \frac{gM}{\alpha} exp(\alpha(T-t)) + P_2$$

When $t \to T$,

$$lnC_i\ (t \to T) = \frac{gM}{\alpha} + P_2$$

$$P_2 = ln(C_0 exp(-MT)) - \frac{gM}{\alpha}$$

$$P_2 = -\frac{gM}{\alpha} - MT + lnC_0$$

$$lnC_i = \frac{gM}{\alpha}[exp(\alpha(T-t)) - 1] - MT + lnC_0$$

$$C_i = C_0 exp\left\{\frac{gM}{\alpha}[exp(\alpha(T-t)) - 1] - MT\right\}$$

Set $K = \frac{gM}{\alpha}$

$$C_i = C_0 \exp(-MT) exp\{K[exp(\alpha(T-t)) - 1]\}$$

In our experiments, $T = 300\, ms$, $\exp(-MT) \to 1$, and the images are captured at a frequency of 1 image/sec, thus for a 60 s sequence, $t \gg T$ and $g \to 1$. We obtain the final concentration equation as following:

$$C_i \approx C_0 e^{[K(e^{-\alpha t}-1)]}$$

APPENDIX C

FUTURE WORK: PIEZO ACTUATOR FOR DISTANCE CONTROL

Our present micromanipulator is gear-driven, and a backlash is produced when reversing the travel direction. This backlash is not reproducible and in a range of 0.2 ~ 2 μm. The effect of backlash is disastrous as the distance control depends fully on the current measurement. Therefore, a piezo-driven manipulator is under construction to obtain an accurate distance.

A piezo actuator from Physik Instrumente is attached to the present micromanipulator. The piezo has no backlash and has a travel distance of 30 μm. In this way, we solve the backlash issue and provide precise distance manipulation. A labview program can be set up for the piezo control to enable the automation of finding the cell-tip touching point by telling the percentage of current drop in the test circuit.

A deeper inspection indicates that the change of resistance cannot be detected unless tip-cell distance is extremely small, as shown in Table AC.1 in terms of large cells, 2 μm tip capillary and short distance. We can control the tip-cell distance by current measurement in test circuit. When the capillary tip was touching the cell, a seal was formed. Cell membranes have been reported to have affinity to substrate materials such as glass [96]. In patch-clamp technology, people have been using glass pipets having an opening of 0.5 ~ 1 μm to create a

giga-seal on cells to study the electrophysiological behavior of ion channels [118, 119]. In our case, the tip was larger, and a smaller seal was expected. Figure AC.1 shows how the system resistance in test circuit changes when the tip approaches to the cell. Although the real system resistance is larger than the simulated value due to other resistance sources, this theoretical result still strongly supports our current measurement-based distance control method.

Table AC. 1 Short distance resistance measurement in electroporation simulation model with large cells (R = 20 µm) and a 2 µm tip EFC

Tip-cell distance (µm)	Voltage at tip (V)	Current Integration (µA)	System Resistance (MΩ)	Change (%)	Lock-in amplifier Reading (µA)
1	5.80	34.05	14.69	0	0.136
0.5	7.10	34.97	14.72	-0.17	0.136
0.25	9.191	33.86	14.77	-0.39	0.136
0.125	11.65	33.72	14.835	-0.73	0.135
0	19.81	33.12	15.06	-2.65	0.133
Seal (-0.047)	29.13	32.56	15.36	-4.53	0.13
Dent -1	156.74	24.00	20.83	-29.62	0.096

Relying on the reading from lock-in amplifier, we were able to tell a change of > 2%. In the following simulation part, we found that this extent of change happened only when the distance decreased to zero. A deeper indent enhanced the resistance change, which helped to tell the real change from the already weakened noise. Combined with a high resolution micromanipulator, we were able to find the zero distance point, and then retreated from the point to get a desired distance.

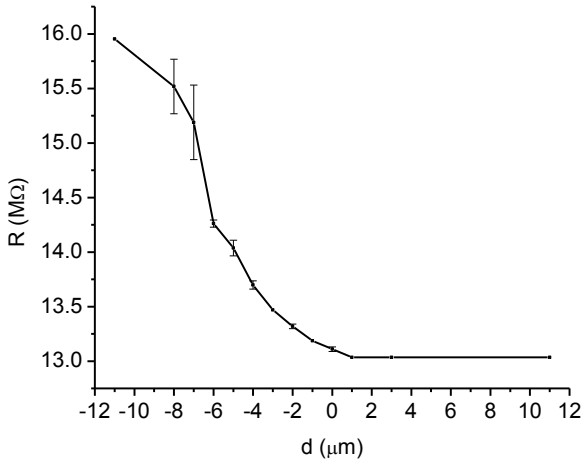

Figure AC. 1 Resistance changes when a 5 μm capillary tip seals with cell membrane.

We set the point when the resistance begins to change as distance zero. Based on the microscope observation and simulation, this zero point is extremely close to the touching point.

A significant advantage of this distance control method over the scale bar measurement is that higher spatial resolution can be achieved. Usually the scale bar method is limited beyond 1 μm. With the current measurement method, the limitation mainly comes from the noise and micromanipulator. A high resolution micromanipulator can possibly help to obtain a spatial resolution of 0.1 μm. Some other advantages are (1) the freedom to approach the EFC from any angle to the cell; (2) the distance is not necessary the projection one on the horizontal plane (this may induce distance variance by the gap between the tip and cell dish), it can be a direct distance between the tip and cell.

BIBLIOGRAPHY

1. J. Olofsson, K. Nolkrantz, F. Ryttsen, B. A. Lambie, S. G. Weber, O. Orwar, Single-cell electroporation. *Curr. Opin. Biotechnol.* 2003, *14*. 29-34.
2. T.-C. Chao, A. Ros, Microfluidic single-cell analysis of intracellular compounds. *Journal of the Royal Society, Interface* 2008, *5*. S139-S150.
3. M. B. Fox, D. C. Esveld, A. Valero, R. Luttge, H. C. Mastwijk, P. V. Bartels, A. Berg, R. M. Boom, Electroporation of cells in microfluidic devices: a review. *Anal. Bioanal. Chem.* 2006, *385*. 474-485.
4. N. Uesaka, M. Nishiwaki, N. Yamamoto, Single cell electroporation method for axon tracing in cultured slices. *Dev., Growth Differ.* 2008, *50*. 475-477.
5. K. P. Mishra, Membrane electroporation and emerging biomedical applications. *Handb. Membr. Sep.* 2009. 741-758.
6. J. C. Weaver, Y. A. Chizmadzhev, Theory of electroporation: A review. *Bioelectrochem. Bioenerg.* 1996, *41*. 135-160.
7. S. Y. Ho, G. S. Mittal, Electroporation of cell membranes: a review. *Crit. Rev. Biotechnol.* 1996, *16*. 349-62.
8. K. A. DeBruin, W. Krassowska, Modeling electroporation in a single cell. I. Effects of field strength and rest potential. *Biophys. J.* 1999, *77*. 1213-1224.
9. S. A. Freeman, M. A. Wang, J. C. Weaver, Theory of electroporation of planar bilayer membranes: predictions of the aqueous area, change in capacitance, and pore-pore separation. *Biophys. J.* 1994, *67*. 42-56.
10. V. F. Pastushenko, Y. A. Chizmadzhev, V. B. Arakelyan, Electric breakdown of bilayer lipid membranes. II. Calculation of the membrane lifetime in the steady-state diffusion approximation. *Bioelectrochem. Bioenerg.* 1979, *6*. 53-62.
11. J. M. Escoffre, D. S. Dean, M. Hubert, M. P. Rols, C. Favard, Membrane perturbation by an external electric field: a mechanism to permit molecular uptake. *Eur. Biophys. J.* 2007, *36*. 973-983.
12. L. Delemotte, F. Dehez, W. Treptow, M. Tarek, Modeling Membranes under a Transmembrane Potential. *J. Phys. Chem. B* 2008, *112*. 5547-5550.
13. Z. Vasilkoski, A. T. Esser, T. R. Gowrishankar, J. C. Weaver, Membrane electroporation: The absolute rate equation and nanosecond time scale pore creation. *Physical Review E: Statistical, Nonlinear, and Soft Matter Physics* 2006, *74*. 021904.

14. D. P. Tieleman, H. Leontiadou, A. E. Mark, S.-J. Marrink, Simulation of Pore Formation in Lipid Bilayers by Mechanical Stress and Electric Fields. *J. Am. Chem. Soc.* 2003, *125*. 6382-6383.

15. Z. Vasilkoski, The effect of electric fields on lipid membranes. *Los Alamos National Laboratory, Preprint Archive, Physics* 2006. 1-10, arXiv:physics/0701013.

16. J. C. Weaver, K. T. Powell, R. A. Mintzer, H. Ling, S. R. Sloan, The electrical capacitance of bilayer membranes: The contribution of transient aqueous pores. *Bioelectrochem. Bioenerg.* 1984, *12*. 393-404, DOI: 10.1016/0302-4598(84)87018-x.

17. W. Krassowska, P. D. Filev, Modeling electroporation in a single cell. *Biophys. J.* 2007, *92*. 404-417.

18. S. Talele, P. Gaynor, Non-linear time domain model of electropermeabilization: Response of a single cell to an arbitrary applied electric field. *J. Electrost.* 2007, *65*. 775-784.

19. P. Shil, S. Bidaye, P. B. Vidyasagar, Analyzing the effects of surface distribution of pores in cell electroporation for a cell membrane containing cholesterol. *J. Phys. D: Appl. Phys.* 2008, *41*. 055502.

20. C. Barrau, J. Teissie, B. Gabriel, Osmotically induced membrane tension facilitates the triggering of living cell electropermeabilization. *Bioelectrochemistry* 2004, *63*. 327-332.

21. J. Teissie, M. P. Rols, An experimental evaluation of the critical potential difference inducing cell membrane electropermeabilization. *Biophys. J.* 1993, *65*. 409-13.

22. M.-P. Rols, Electropermeabilization, a physical method for the delivery of therapeutic molecules into cells. *Biochim. Biophys. Acta: Biomembranes* 2006, *1758*. 423-428.

23. J. Gimsa, D. Wachner, Analytical description of the transmembrane voltage induced on arbitrarily oriented ellipsoidal and cylindrical cells. *Biophys. J.* 2001, *81*. 1888-1896.

24. K. Maswiwat, D. Wachner, R. Warnke, J. Gimsa, Simplified equations for the transmembrane potential induced in ellipsoidal cells of rotational symmetry. *J. Phys. D: Appl. Phys.* 2007, *40*. 914-923.

25. J. Teissie, M. Golzio, M. P. Rols, Mechanisms of cell membrane electropermeabilization: A minireview of our present (lack of ?) knowledge. *Biochim. Biophys. Acta: General Subjects* 2005, *1724*. 270-280.

26. J. Bernhardt, H. Pauly, On the generation of potential differences across the membranes of ellipsoidal cells in an alternating electrical field. *Biophysik* 1973, *10*. 89-98.

27. K. Kinosita, Jr., T. Y. Tsong, Voltage-induced conductance in human erythrocyte membranes. *Biochim. Biophys. Acta: Biomembranes* 1979, *554*. 479-97.

28. M. Hibino, H. Itoh, K. Kinosita, Jr., Time courses of cell electroporation as revealed by submicrosecond imaging of transmembrane potential. *Biophys. J.* 1993, *64*. 1789-800.

29. P. T. Vernier, Y. Sun, A. Gundersen Martin, Nanoelectropulse-driven membrane perturbation and small molecule permeabilization. *BMC Cell Biol.* 2006, *7*. 37.

30. S. J. Beebe, J. White, P. F. Blackmore, Y. Deng, K. Somers, K. H. Schoenbach, Diverse Effects of Nanosecond Pulsed Electric Fields on Cells and Tissues. *DNA Cell Biol.* 2003, *22*. 785-796.

31. L. Bandiera, M. Borgo, G. Cellere, A. De Toni, L. Santoni, C. Bersani, A. Paccagnella, Electrical modeling of a biochip for genetic manipulation of single cells. *Tech. Dig. - Int. Electron Devices Meet.* 2006, *1*. 455-458.

32. B. A. Lambie, C. Brennan, J. Olofsson, O. Orwar, S. G. Weber, Experimentally Determining the iR Drop in Solution at Carbon Fiber Microelectrodes with Current Interruption and Application to Single-Cell Electroporation. *Anal. Chem.* 2007, *79*. 3771-3778.

33. I. Zudans, A. Agarwal, O. Orwar, S. G. Weber, Numerical calculations of single-cell electroporation with an electrolyte-filled capillary. *Biophys. J.* 2007, *92*. 3696-3705.

34. H. He, D. C. Chang, Y.-K. Lee, Micro pulsed radio-frequency electroporation chips. *Bioelectrochemistry* 2006, *68*. 89-97.

35. M. Boudes, S. Pieraut, J. Valmier, P. Carroll, F. Scamps, Single-cell electroporation of adult sensory neurons for gene screening with RNA interference mechanism. *J. Neurosci. Methods* 2008, *170*. 204-211.

36. K. Haas, W.-C. Sin, A. Javaherian, Z. Li, H. T. Cline, Single-cell electroporation for gene transfer in vivo. *Neuron* 2001, *29*. 583-591.

37. M. Khine, C. Ionescu-Zanetti, A. Blatz, L.-P. Wang, L. P. Lee, Single-cell electroporation arrays with real-time monitoring and feedback control. *Lab on a Chip* 2007, *7*. 457-462.

38. C. Ionescu-Zanetti, A. Blatz, M. Khine, Electrophoresis-assisted single-cell electroporation for efficient intracellular delivery. *Biomed. Microdevices* 2008, *10*. 113-116.

39. A. Valero, J. N. Post, J. W. van Nieuwkasteele, P. M. ter Braak, W. Kruijer, A. van den Berg, Gene transfer and protein dynamics in stem cells using single cell electroporation in a microfluidic device. *Lab on a Chip* 2008, *8*. 62-67.

40. A. Paganin-Gioanni, E. Bellard, J. M. Escoffre, M. R. Rols, J. Teissie, M. Golzio, Direct visualization at the single-cell level of siRNA electrotransfer into cancer cells. *Proc. Natl. Acad. Sci. U. S. A.* 2011, *108*. 10443-10447, S10443/1-S10443/4, DOI: 10.1073/pnas.1103519108.

41. M. Tanaka, Y. Yanagawa, N. Hirashima, Transfer of small interfering RNA by single-cell electroporation in cerebellar cell cultures. *J. Neurosci. Methods* 2009, *178*. 80-86.

42. B. Judkewitz, M. Rizzi, K. Kitamura, M. Haeusser, Targeted single-cell electroporation of mammalian neurons in vivo. *Nat. Protoc.* 2009, *4*. 862-869.

43. M. Puc, T. Kotnik, L. M. Mir, D. Miklavcic, Quantitative model of small molecules uptake after in vitro cell electropermeabilization. *Bioelectrochemistry* 2003, *60*. 1-10.

44. A. Agarwal, M. Wang, J. Olofsson, O. Orwar, S. G. Weber, Control of the Release of Freely Diffusing Molecules in Single-Cell Electroporation. *Anal. Chem.* 2009, *81*. 8001-8008.

45. M. Wang, O. Orwar, S. G. Weber, Single-cell transfection by electroporation using an electrolyte/plasmid-filled capillary. *Anal. Chem.* 2009, *81*. 4060-4067.

46. H. He, D. C. Chang, Y.-K. Lee, Using a micro electroporation chip to determine the optimal physical parameters in the uptake of biomolecules in HeLa cells. *Bioelectrochemistry* 2007, *70*. 363-368.

47. K. Kitamura, B. Judkewitz, M. Kano, W. Denk, M. Haeusser, Targeted patch-clamp recordings and single-cell electroporation of unlabeled neurons in vivo. *Nat. Methods* 2008, *5*. 61-67.

48. F. Ryttsen, C. Farre, C. Brennan, S. G. Weber, K. Nolkrantz, K. Jardemark, D. T. Chiu, O. Orwar, Characterization of single-cell electroporation by using patch-clamp and fluorescence microscopy. *Biophys. J.* 2000, *79*. 1993-2001.

49. D. Braeken, R. Huys, J. Loo, C. Bartic, G. Borghs, G. Callewaert, W. Eberle, Localized electrical stimulation of in vitro neurons using an array of sub-cellular sized electrodes. *Biosens. Bioelectron.* 2010, *26*. 1474-1477, DOI: 10.1016/j.bios.2010.07.086.

50. A. G. Pakhomov, J. F. Kolb, J. A. White, R. P. Joshi, S. Xiao, K. H. Schoenbach, Long-lasting plasma membrane permeabilization in mammalian cells by nanosecond pulsed electric field (nsPEF). *Bioelectromagnetics* 2007, *28*. 655-663.

51. W. Wang, K. Foley, X. Shan, S. Wang, S. Eaton, V. J. Nagaraj, P. Wiktor, U. Patel, N. Tao, Single cells and intracellular processes studied by a plasmonic-based electrochemical impedance microscopy. *Nat. Chem.* 2011, *3*. 249-255, DOI: 10.1038/nchem.961.

52. W. C. Chang, D. W. Sretavan, Single cell and neural process experimentation using laterally applied electrical fields between pairs of closely apposed microelectrodes with vertical sidewalls. *Biosens. Bioelectron.* 2009, *24*. 3600-3607.

53. S. Vassanelli, L. Bandiera, M. Borgo, G. Cellere, L. Santoni, C. Bersani, M. Salamon, M. Zaccolo, L. Lorenzelli, S. Girardi, M. Mashietto, M. Dal Maschio, A. Paccagnella, Space and time-resolved gene expression experiments on cultured mammalian cells by a single-cell electroporation microarray. *N. Biotechnol.* 2008, *25*. 55-67.

54. T. Ishibashi, K. Takoh, H. Kaji, T. Abe, M. Nishizawa, A porous membrane-based culture substrate for localized in situ electroporation of adherent mammalian cells. *Sens. Actuators, B* 2007, *B128*. 5-11.

55. J. A. Lundqvist, F. Sahlin, M. A. I. Aberg, A. Stromberg, P. S. Eriksson, O. Orwar, Altering the biochemical state of individual cultured cells and organelles with ultramicroelectrodes. *Proc. Natl. Acad. Sci. U. S. A.* 1998, *95*. 10356-10360.

56. X. Yang, Z. Zhou, M. Xiao, Q. Wang, Y. Li, R. Yang, C. Shao, Sodium electrode and system for single-cell electroporation. 2007.

57. D. Nawarathna, K. Unal, H. K. Wickramasinghe, Localized electroporation and molecular delivery into single living cells by atomic force microscopy. *Appl. Phys. Lett.* 2008, *93*. 153111.

58. M. A. I. Aberg, F. Ryttsen, G. Hellgren, K. Lindell, L. E. Rosengren, A. J. MacLennan, B. Carlsson, O. Orwar, P. S. Eriksson, Selective introduction of antisense oligonucleotides into single adult CNS progenitor cells using electroporation demonstrates the requirement of STAT3 activation for CNTF-induced gliogenesis. *Mol. Cell. Neurosci.* 2001, *17*. 426-443.

59. M. Karlsson, K. Nolkrantz, M. J. Davidson, A. Stroemberg, F. Ryttsen, B. Kerman, O. Orwar, Electroinjection of Colloid Particles and Biopolymers into Single Unilamellar Liposomes and Cells for Bioanalytical Applications. *Anal. Chem.* 2000, *72*. 5857-5862.

60. L. J. Graham, R. del Abajo, T. Gener, E. Fernandez, A method of combined single-cell electrophysiology and electroporation. *J. Neurosci. Methods* 2007, *160*. 69-74.

61. N. Uesaka, Y. Hayano, A. Yamada, N. Yamamoto, Interplay between laminar specificity and activity-dependent mechanisms of thalamocortical axon branching. *J. Neurosci.* 2007, *27*. 5215-5223.

62. N. Uesaka, S. Hirai, T. Maruyama, S. Ruthazer Edward, N. Yamamoto, Activity dependence of cortical axon branch formation: a morphological and electrophysiological study using organotypic slice cultures. *J. Neurosci.* 2005, *25*. 1-9.

63. J. L. Rae, R. A. Levis, Single-cell electroporation. *Pflugers Archiv* 2002, *443*. 664-670.

64. J. Rathenberg, T. Nevian, V. Witzemann, High-efficiency transfection of individual neurons using modified electrophysiology techniques. *J. Neurosci. Methods* 2003, *126*. 91-8.

65. C. Bae, P. J. Butler, Automated single-cell electroporation. *Biotechniques* 2006, *41*. 399-400,402.

66. K. Sakaki, N. Dechev, D. Burke Robert, J. Park Edward, Development of an autonomous biological cell manipulator with single-cell electroporation and visual servoing capabilities. *IEEE Trans. Biomed. Eng.* 2009, *56*. 2064-74.

67. K. Nolkrantz, C. Farre, A. Brederlau, R. I. D. Karlsson, C. Brennan, P. S. Eriksson, S. G. Weber, M. Sandberg, O. Orwar, Electroporation of single cells and tissues with an electrolyte-filled capillary. *Anal. Chem.* 2001, *73*. 4469-4477.

68. K. Nolkrantz, C. Farre, K. J. Hurtig, P. Rylander, O. Orwar, Functional screening of intracellular proteins in single cells and in patterned cell arrays using electroporation. *Anal. Chem.* 2002, *74*. 4300-4305.

69. J. Olofsson, M. Levin, A. Stroemberg, S. G. Weber, F. Ryttsen, O. Orwar, Scanning electroporation of selected areas of adherent cell cultures. *Anal. Chem.* 2007, *79*. 4410-4418.

70. G. Cellere, L. Bandiera, M. Borgo, A. De Toni, L. Santoni, A. Paccagnella, L. Lorenzelli, A purely electronic method to measure transfection efficiency in a single-cell electroporation biochip. *ECS Transactions* 2007, *6*. 1-11.

71. P. J. Koester, C. Tautorat, H. Beikirch, J. Gimsa, W. Baumann, Recording electric potentials from single adherent cells with 3D microelectrode arrays after local electroporation. *Biosens. Bioelectron.* 2010, *26*. 1731-1735, DOI: 10.1016/j.bios.2010.08.003.

72. Y. Huang, B. Rubinsky, Microfabricated electroporation chip for single cell membrane permeabilization. *Sens. Actuators, A: Phys* 2001, *A89*. 242-249.

73. Y. Huang, B. Rubinsky, Micro-Electroporation: Improving the Efficiency and Understanding of Electrical Permeabilization of Cells. *Biomed. Microdevices* 1999, *2*. 145-150.

74. O. Kurosawa, H. Oana, S. Matsuoka, A. Noma, H. Kotera, M. Washizu, Electroporation through a micro-fabricated orifice and its application to the measurement of cell response to external stimuli. *Meas. Sci. Technol.* 2006, *17*. 3127-3133.

75. Y. Huang, B. Rubinsky, Flow-through micro-electroporation chip for high efficiency single-cell genetic manipulation. *Sens. Actuators, A: Phys* 2003, *A104*. 205-212.

76. E. Diaz-Rivera Ruben, B. Rubinsky, Electrical and thermal characterization of nanochannels between a cell and a silicon based micro-pore. *Biomed Microdevices* 2006, *8*. 25-34.

77. A. Ul Haque, M. Zuberi, E. Diaz-Rivera Ruben, D. Marshall Porterfield, Electrical characterization of a single cell electroporation biochip with the 2-D scanning vibrating electrode technology. *Biomed Microdevices* 2009, *11*. 1239-50.

78. M. Khine, A. Lau, C. Ionescu-Zanetti, J. Seo, L. P. Lee, A single cell electroporation chip. *Lab on a Chip* 2005, *5*. 38-43.

79. J. Seo, C. Ionescu-Zanetti, J. Diamond, R. Lal, L. P. Lee, Integrated multiple patch-clamp array chip via lateral cell trapping junctions. *Appl. Phys. Lett.* 2004, *84*. 1973-1975.

80. A. Sarkar, B. Mitra, A. Shastry, S. Wadia, R. Mulherkar, R. Lal, A low voltage single cell electroporator with a microfabricated sense-porate aperture. *IEEE International Conference on Micro Electro Mechanical Systems* 2004. 375-378.

81. H.-Y. Wang, C. Lu, Electroporation of Mammalian Cells in a Microfluidic Channel with Geometric Variation. *Anal. Chem.* 2006, *78*. 5158-5164.

82. H.-Y. Wang, C. Lu, High-throughput and real-time study of single cell electroporation using microfluidics: effects of medium osmolarity. *Biotechnol. Bioeng.* 2006, *95*. 1116-1125.

83. H. Y. Wang, C. Lu, Microfluidic electroporation for delivery of small molecules and genes into cells using a common DC power supply. *Biotechnol. Bioeng.* 2008, *100*. 579-586.

84. N. Bao, Y. Zhan, C. Lu, Microfluidic Electroporative Flow Cytometry for Studying Single-Cell Biomechanics. *Anal. Chem.* 2008, *80*. 7714-7719.

85. R. Ziv, Y. Steinhardt, G. Pelled, D. Gazit, B. Rubinsky, Micro-electroporation of mesenchymal stem cells with alternating electrical current pulses. *Biomed Microdevices* 2009, *11*. 95-101.

86. Y. Zhan, J. Wang, N. Bao, C. Lu, Electroporation of Cells in Microfluidic Droplets. *Anal. Chem.* 2009, *81*. 2027-2031.

87. F. Yang, H. He, D. C. Chang, Y.-K. Lee, Parametric study of pulsed radio-frequency electroporation on microchips at the single-cell level. *Special Publication - Royal Society of Chemistry* 2004, *297*. 79-81.

88. D. C. Chang, Cell poration and cell fusion using an oscillating electric field. *Biophys. J.* 1989, *56*. 641-652.

89. Y. Cho, B. Le Pioufle, N. Takama, B. Kim, A silicon-based single-cell electroporation microchip for gene transfer. *Int. Conf. Microtechnol. Med. Biol. Okinawa, Japan* 2006. 195-197.

90. H. Sedgwick, F. Caron, P. B. Monaghan, W. Kolch, J. M. Cooper, Lab-on-a-chip technologies for proteomic analysis from isolated cells. *Journal of the Royal Society, Interface* 2008, *5*. S123-S130.

91. J. K. Valley, S. Neale, H.-Y. Hsu, A. T. Ohta, A. Jamshidi, M. C. Wu, Parallel single-cell light-induced electroporation and dielectrophoretic manipulation. *Lab on a Chip* 2009, *9*. 1714-1720.

92. J. E. Bestman, R. C. Ewald, S.-L. Chiu, H. T. Cline, In vivo single-cell electroporation for transfer of DNA and macromolecules. *Nat. Protoc.* 2006, *1*. 1268-1273.

93. Y. Saheki, S.-T. Li, M. Matsushita, Y.-M. Wu, W.-H. Cai, F.-Y. Wei, Y.-F. Lu, A. Moriwaki, K. Tomizawa, H. Matsui, A new approach to inhibiting astrocytic IP3-induced intracellular calcium increase in an astrocyte-neuron co-culture system. *Brain Res.* 2005, *1055*. 196-201.

94. K. Haas, K. Jensen, W. C. Sin, L. Foa, H. T. Cline, Targeted electroporation in Xenopus tadpoles in vivo - from single cells to the entire brain. *Differentiation* 2002, *70*. 148-154.

95. S. M. Schanuel, K. A. Bell, S. C. Henderson, A. R. McQuiston, Heterologous expression of the invertebrate FMRFamide-gated sodium channel as a mechanism to selectively activate mammalian neurons. *Neuroscience* 2008, *155*. 374-386.

96. H. Seidl Armin, W. Rubel Edwin, A simple method for multiday imaging of slice cultures. *Microsc. Res. Tech.* 2010, *73*. 37-44.

97. A. T. Silva, A. Nguyen, C. Ye, J. Verchot-Lubicz, J. H. Moon, Conjugated polymer nanoparticles for effective siRNA delivery to tobacco BY-2 protoplasts. *BMC Plant Biol.* 2010, *10*. 291, DOI: 10.1186/1471-2229-10-291.

98. M. Tanaka, M. Asaoka, Y. Yanagawa, N. Hirashima, Long-Term Gene-Silencing Effects of siRNA Introduced by Single-Cell Electroporation into Postmitotic CNS Neurons. *Neurochem. Res.* 2011, *36*. 1482-1489, DOI: 10.1007/s11064-011-0474-6.

99. S. B. Lang, T. Bonhoeffer, C. Lohmann, Simultaneous imaging of morphological plasticity and calcium dynamics in dendrites. *Nat. Protoc.* 2006, *1*. 1859-1864.

100. L. Rautenberg Philipp, B. Grothe, F. Felmy, Quantification of the three-dimensional morphology of coincidence detector neurons in the medial superior olive of gerbils during late postnatal development. *J. Comp. Neurol.* 2009, *517*. 385-96.

101. S. A. Sorensen, E. W. Rubel, The level and integrity of synaptic input regulates dendrite structure. *J. Neurosci.* 2006, *26*. 1539-1550.

102. S. A. Sorensen, E. W. Rubel, Relative input strength rapidly regulates dendritic structure of chick auditory brainstem neurons. *J. Comp. Neurol.* 2011, *519*. 2838-51.

103. K. Couchman, B. Grothe, F. Felmy, Medial superior olivary neurons receive surprisingly few excitatory and inhibitory inputs with balanced strength and short-term dynamics. *J. Neurosci.* 2010, *30*. 17111-17121, DOI: 10.1523/jneurosci.1760-10.2010.

104. D. M. Feliciano, J. L. Quon, T. Su, M. M. Taylor, A. Bordey, Postnatal neurogenesis generates heterotopias, olfactory micronodules and cortical infiltration following single-cell Tsc1 deletion. *Hum. Mol. Genet.* 2012, *21*. 799-810, DOI: 10.1093/hmg/ddr511.

105. T. Nevian, F. Helmchen, Calcium indicator loading of neurons using single-cell electroporation. *Pfluegers Archiv* 2007, *454*. 675-688.

106. J. H. Marshel, T. Mori, K. J. Nielsen, E. M. Callaway, Targeting Single Neuronal Networks for Gene Expression and Cell Labeling In Vivo. *Neuron* 2010, *67*. 562-574, DOI: 10.1016/j.neuron.2010.08.001.

107. B. R. Davis, D. B. Brown, N. L. Prokopishyn, J. Yannariello-Brown, Micro-injection-mediated hematopoietic stem cell gene therapy. *Current Opinion in Molecular Therapeutics* 2000, *2*. 412-419.

108. S. W. Han, C. Nakamura, I. Obataya, N. Nakamura, J. Miyake, Gene expression using an ultrathin needle enabling accurate displacement and low invasiveness. *Biochem. Biophys. Res. Commun.* 2005, *332*. 633-639.

109. M. Knoblauch, J. M. Hibberd, J. C. Gray, A. J. E. van Bel, A galinstan expansion femtosyringe for microinjection of eukaryotic organelles and prokaryotes. *Nat. Biotechnol.* 1999, *17*. 906-909.

110. C. M. Cuerrier, R. Lebel, M. Grandbois, Single cell transfection using plasmid decorated AFM probes. *Biochem. Biophys. Res. Commun.* 2007, *355*. 632-636.

111. U. K. Tirlapur, K. Konig, Cell biology - Targeted transfection by femtosecond laser. *Nature* 2002, *418*. 290-291.

112. M.-P. Rols, J. Teissie, Electropermeabilization of mammalian cells to macromolecules: control by pulse duration. *Biophys. J.* 1998, *75*. 1415-1423.

113. A. Agarwal, I. Zudans, O. Orwar, S. G. Weber, Simultaneous Maximization of Cell Permeabilization and Viability in Single-Cell Electroporation Using an Electrolyte-Filled Capillary. *Anal. Chem.* 2007, *79*. 161-167.

114. M. E. Langmuir, J.-R. Yang, K. A. LeCompte, R. E. Durand, New thiol active fluorophores for intracellular thiols and glutathione measurement. *Fluorescence Microscopy and Fluorescent Probes* 1996. 229-233.

115. V. E. Kagan, A. I. Kuzmenko, Y. Y. Tyurina, A. A. Shvedova, T. Matsura, J. C. Yalowich, Pro-oxidant and antioxidant mechanisms of etoposide in HL-60 cells: role of myeloperoxidase. *Cancer Res.* 2001, *61*. 7777-7784.

116. E. C. Gaetjens, P. Chen, J. D. Broome, L1210(A) mouse lymphoma cells depleted of glutathione with L-buthionine-S-R-sulfoximine proliferate in tissue culture. *Biochem. Biophys. Res. Commun.* 1984, *123*. 626-32.

117. O. de Carmejane, J. J. Schwinefus, S.-C. Wang, M. D. Morris, Electrophoretic separation of linear and supercoiled DNA in uncoated capillaries. *J. Chromatogr. A* 1999, *849*. 267-276.

118. A. O. Bilska, K. A. DeBruin, W. Krassowska, Theoretical modeling of the effects of shock duration, frequency, and strength on the degree of electroporation. *Bioelectrochemistry* 2000, *51*. 133-143.

119. M. Golzio, M. P. Rols, J. Teissie, In vitro and in vivo electric field-mediated permeabilization, gene transfer, and expression. *Methods* 2004, *33*. 126-135.

120. L. M. Mir, Application of electroporation gene therapy: past, current, and future. *Methods Mol. Biol.* 2008, *423*. 3-17.

121. M. Spassova, I. Tsoneva, A. G. Petrov, J. I. Petkova, E. Neumann, Dip patch clamp currents suggest electrodiffusive transport of the polyelectrolyte DNA through lipid bilayers. *Biophys. Chem.* 1994, *52*. 267-74.

122. L. V. Chernomordik, A. V. Sokolov, V. G. Budker, Electrostimulated uptake of DNA by liposomes. *Biochim. Biophys. Acta: Biomembranes* 1990, *1024*. 179-83.

123. N. I. Hristova, I. Tsoneva, E. Neumann, Sphingosine-mediated electroporative DNA transfer through lipid bilayers. *FEBS Lett.* 1997, *415*. 81-86.

124. Y. J. Kang, M. D. Enger, Glutathione content and growth in A549 human lung carcinoma cells. *Exp. Cell Res.* 1990, *187*. 177-9.

125. S. A. Gallo, A. Sen, M. L. Hensen, S. W. Hui, Temperature-dependent electrical and ultrastructural characterizations of porcine skin upon electroporation. *Biophys. J.* 2002, *82*. 109-119.

126. J. Loefblom, N. Kronqvist, M. Uhlen, S. Staahl, H. Wernerus, Optimization of electroporation-mediated transformation: Staphylococcus carnosus as model organism. *J. Appl. Microbiol.* 2007, *102*. 736-747.

127. T. Ohshima, M. Sato, Bacterial sterilization and intracellular protein release by a pulsed electric field. *Adv. Biochem. Eng. Biotechnol.* 2004, *90*. 113-133.

128. B. J. Wards, D. M. Collins, Electroporation at elevated temperatures substantially improves transformation efficiency of slow-growing mycobacteria. *FEMS Microbiol. Lett.* 1996, *145*. 101-105.

129. M. P. Rols, C. Delteil, G. Serin, J. Teissie, Temperature effects on electrotransfection of mammalian cells. *Nucleic Acids Res.* 1994, *22*. 540.

130. H. G. Sachs, P. J. Stambrook, J. D. Ebert, Changes in membrane potential during the cell cycle. *Exp. Cell Res.* 1974, *83*. 362-6.

131. V. L. Sukhorukov, C. S. Djuzenova, W. M. Arnold, U. Zimmermann, DNA, protein, and plasma-membrane incorporation by arrested mammalian cells. *J. Membr. Biol.* 1994, *142*. 77-92.

132. M. Golzio, J. Teissie, M.-P. Rols, Cell synchronization effect on mammalian cell permeabilization and gene delivery by electric field. *Biochim. Biophys. Acta: Biomembranes* 2002, *1563*. 23-28.

133. T. Yorifuji, S. Tsuruta, H. Mikawa, The effect of cell synchronization on the efficiency of stable gene transfer by electroporation. *FEBS Lett.* 1989, *245*. 201-3.

134. K. Okada, I. Takebe, T. Nagata, Experession and integration of genes introduced into highly synchronized plant protoplasts. *Mol. Gen. Genet.* 1986, *205*. 398-403, DOI: 10.1007/bf00338073.

135. R. P. Joshi, Q. Hu, K. H. Schoenbach, H. P. Hjalmarson, Improved energy model for membrane electroporation in biological cells subjected to electrical pulses. *Phys. Rev. E* 2002, *65*. 041920.

136. M. Tarek, Membrane electroporation: a molecular dynamics simulation. *Biophys. J.* 2005, *88*. 4045-53.

137. D. J. Bicout, E. Kats, Rupture of a biomembrane under Dynamic Surface Tension. *Phys. Rev. E* 2012, *85*. 031905.

138. P. T. Vernier, M. J. Ziegler, Y. Sun, M. A. Gundersen, D. P. Tieleman, Nanopore-facilitated, voltage-driven phosphatidylserine translocation in lipid bilayers-in cells and in silico. *Phys. Biol.* 2006, *3*. 233-247, DOI: 10.1088/1478-3975/3/4/001.

139. A. El-Hag, S. H. Jayaram, in *Dielectric Liquids, 2008. ICDL 2008. IEEE International Conference on*. 2008, pp 1-4.

140. L. Raptis, K. L. Firth, Electroporation of adherent cells in situ. *DNA Cell Biol.* 1990, *9*. 615-21, DOI: 10.1089/dna.1990.9.615.

141. G. Saulis, Pore disappearance in a cell after electroporation: theoretical simulation and comparison with experiments. *Biophys. J.* 1997, *73*. 1299-1309, DOI: 10.1016/s0006-3495(97)78163-3.

142. G. Saulis, M. S. Venslauskas, J. Naktinis, Kinetics of pore resealing in cell membranes after electroporation. *Bioelectrochem. Bioenerg.* 1991, *26*. 1-13, DOI: 10.1016/0302-4598(91)87029-g.

143. C. J. Evenhuis, R. M. Guijt, M. Macka, P. J. Marriott, P. R. Haddad, Variation of zeta-potential with temperature in fused-silica capillaries used for capillary electrophoresis. *Electrophoresis* 2006, *27*. 672-676, DOI: 10.1002/elps.200500566.

144. E. Stellwagen, Y. Lu, N. C. Stellwagen, Unified Description of Electrophoresis and Diffusion for DNA and Other Polyions. *Biochemistry (Mosc).* 2003, *42*. 11745-11750.